

Acoustic images of the carotid artery

Acoustic images of the carotid artery

Akoestische plaatjes van de halsslagader

Pieter Kruizinga

ISBN: 978-94-6259-571-2
Publisher: Ipskamp Drukkers
Cover design: Pieter Kruizinga

A digital version of this thesis is available at <http://repub.eur.nl/pub/>
Copyright © 2015 by Pieter Kruizinga, Rotterdam The Netherlands

Acoustic images of the carotid artery

Akoestische plaatjes van de halsslagader

Proefschrift

ter verkrijging van de graad van doctor aan de
Erasmus Universiteit Rotterdam
op gezag van de rector magnificus

prof.dr. H.A.P. Pols

en volgens het besluit van het College voor Promoties.

De openbare verdediging zal plaatsvinden op
dinsdag 10 maart 2015 om 13:30 uur

door

Pieter Kruizinga

geboren te Aduard



Promotiecommissie

Promotor: Prof. dr. ir. A.F.W. van der Steen

Overige leden: Prof. dr A. van der Lugt
Prof. dr. S.Y. Emelianov
dr. C.L. de Korte

Copromotor: Dr. G. van Soest

The work in this thesis was conducted at the Department of Biomedical Engineering part of the Thorax Center of the Erasmus Medical Center, Rotterdam The Netherlands

The publication of this thesis was financially supported by: Laser2000, Cardialysis and the Erasmus Medical Center.

Financial support by the Dutch Heart Foundation for the publication of this thesis is gratefully acknowledged.

Preface

If while reading this you put two fingers on the side of your neck, just below the jaw, you will feel a pulsating artery - confirming that you are alive. This artery is called the carotid artery. We have two of them, one on each side of the neck. These arteries supply the brain and the rest of your head and neck with oxygenated blood. Blockage of one of these arteries by a plaque growing on the inside of the artery wall may compromise brain function. More importantly, if this plaque breaks and is exposed to the blood stream, a stroke with fatal consequences may follow.

This thesis is devoted to the carotid artery or, more specifically, to imaging of the carotid artery. Over a period of four years, together with researchers from the Biomedical Engineering group of the Erasmus Medical Centre, I have tried to improve existing imaging methods and develop new ones, for use in detecting a plaque and in determining the stability of a plaque inside the carotid artery. The result of this endeavour is the thesis that now lies before you.

Contents

Chapter 1: Introduction	1
<u>Part I: High frame-rate imaging reveals plaque dynamics</u>	
Chapter 2: Fourier domain image reconstruction	11
Chapter 3: Imaging carotid artery wall dynamics	25
Chapter 4: Vector Displacement Imaging	39
<u>Part II: Photoacoustic imaging reveals plaque composition</u>	
Chapter 5: Ultrasound-guided photoacoustic image reconstruction	55
Chapter 6: Photoacoustic imaging of carotid artery atherosclerosis	69
Chapter 7: Discussion and conclusions	77
References	85
Summary	93
Nederlandse Samenvatting	95
Publications	99
Dankwoord - Acknowledgements	101
Curriculum vitae	103
PhD Portfolio	105

Introduction

1.1 Atherosclerosis, a disease of the arteries

Arteries are strong and flexible structures that supply oxygenated blood to the organs. Their strength and flexibility rely on three distinctive layers, called the adventitia, media and intima. These layers of the arterial wall are rich in elastin, collagen and smooth muscle cells [50], which give the arteries complex elastic properties, allowing them to sustain and facilitate rapid and large variations in blood pressure [140].

Arteries can be affected by atherosclerosis, an inflammatory disease that is characterized by plaque growth inside the arterial wall. Because the disease affects arteries throughout the body, the detection of plaques at one site increases the chances of plaques also being found elsewhere. Therefore the finding of a plaque in the carotid artery provides information about the state of the coronary arteries [159, 100, 62, 72]. The fact that atherosclerosis in the carotid and coronary arteries is associated with high mortality - because they supply blood to the brain and the heart - means that much research is focused on these two types of arteries. The carotid artery (CA) is found on both sides of the neck where the common CA bifurcates into the internal and external CA, with the internal CAs supplying the brain with oxygenated blood. The coronary arteries supply the heart with oxygenated blood.

Atherosclerosis that affects these major arteries is believed to be the underlying cause of 50 % of all deaths in western societies [40, 109, 99]. Factors such as age, genetic makeup, blood pressure, cholesterol level, smoking, diabetes and obesity are strongly associated with an increased risk of developing atherosclerosis [172, 126]. Individual risk for developing atherosclerosis can be estimated with algorithms that take these risk factors into account, such as the Framingham Risk Score [172].

Plaques are often found at locations in the arterial tree where normal blood-flow dynamics are altered, such as at the bifurcation of the CA [147]. The process of plaque formation is initiated by the uptake of low-density lipoprotein (LDL) particles that penetrate the endothelium of the intima. The increased cholesterol loading of the intima initiates an inflammatory process. During the process of inflammation, more cholesterol accumulates inside the intima, together with white blood cells and macrophages. This early plaque, referred to as a “fatty streak”, may progress into a larger and stable plaque, hampering the

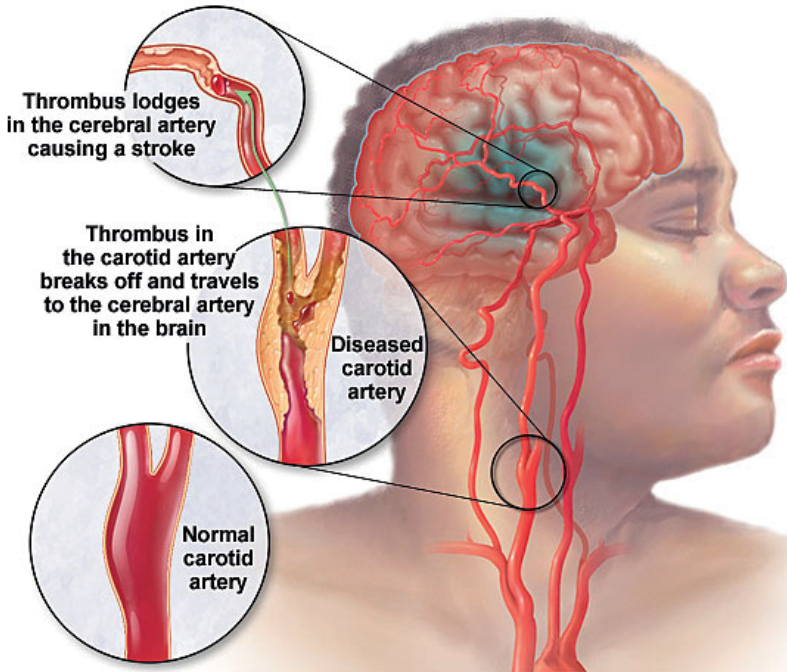


Figure 1.1: **Plaque rupture causes stroke** Artist's impression of a diseased carotid artery causing a stroke through plaque rupture, thrombus formation and downstream arterial blockage (Image obtained from <http://www.mayoclinic.org/ischemic-stroke/img-20009031>)

normal flow of blood. When such a plaque blocks more than 70 % of the lumen, or inner space of the artery, the blood flow is compromised to such a degree that surgical plaque removal is advised [125]. The major complication rate of such an intervention is 6.5 %, of which 1.1 % are fatal and another 5.4 % lead to permanent disability [9, 44].

An atherosclerotic plaque may become unsafe if it progresses into an unstable or “vulnerable” plaque. In this case the initial “fatty streak” develops into a plaque that consists of calcifications and a lipid-rich necrotic core and that is covered by a thin fibrous cap [135]. Small leaky blood vessels are formed inside the plaque - also known as neovascularization of the vasa vasorum - which leads to further expansion of the lipid core and intra-plaque haemorrhage or bleeding [49]. The fibrous tissue of the plaque is infiltrated by macrophages, which further weaken the structure by the secretion of matrix proteinases that break down collagen. When the cap subsequently becomes unstable and breaks, the plaque material enters the bloodstream. The ruptured plaque may then initiate the formation of a thrombus or blood clot. This clot will be carried in the direction of the flow and may consequently block the supply of blood to the tissue located downstream of the blockage [18, 109, 97, 162, 135, 146]. In the case of the CA the ruptured plaque may cause a stroke, and in the case of the coronary arteries a heart attack [109, 54, 96].

A considerable amount of research has been directed at understanding the vulnerable plaque and at finding indicators of its vulnerability. There are strong indications that

information that helps predict whether or not a plaque will rupture can be gained from three, albeit related, sources: the plaque's morphology (thin caps break more easily than thick ones [18, 43, 164]); its mechanical integrity (soft plaques are more prone to rupture than stiff ones [19, 53, 28, 141]); and its biochemical composition (plaques that contain more macrophages rupture more easily [18, 43, 135]; certain lipid components occur only in unstable plaques [149]).

1.2 Imaging of carotid atherosclerosis

Many of the insights concerning plaque vulnerability have been obtained from histological studies, which necessarily take place after death and are therefore static. Nevertheless, plaque development *in vivo* has also been studied extensively using both invasive and non-invasive imaging [164, 42, 17, 46]. The fact that plaques develop locally and that the plaque phenotype is known to be associated with acute events gave rise to the hypothesis that *in vivo* imaging of plaques may identify the so-called “vulnerable patient” [116, 135]. In this manner, imaging serves not only as a tool for detecting plaques in patients, but also for assessing plaque vulnerability. By combining imaging with suitable vulnerability criteria, it may well be possible to improve decision-making on whether or not to intervene. By the same rationale, imaging can be used to scan people who are at risk of developing atherosclerosis and possibly to detect early plaque development or to monitor treatment efficacy.

The most important imaging modalities used in clinical practice to scan the vulnerable patient are computed tomography (CT), magnetic resonance imaging (MRI) and ultrasound (US) [42, 117, 94, 131]. CT uses ionizing X-rays to build up a 3D image. The contrast in CT images originates from differences in X-ray attenuation. Dense calcified plaques show up white against the darker, less dense tissue. Contrast agents in CT angiography add attenuation to the perfused vasculature, making the vessels stand out in soft tissues. An example of a calcified plaque in the bifurcation of the left CA of a patient can be seen in Fig. 1.2 (a). This particular plaque, which obstructed more than 70 % of the lumen, was taken out soon after this scan was taken.

MRI uses the magnetic resonance properties of atomic nuclei - mainly the proton nucleus of ^1H , which is abundant in water - to generate contrast for 3D images. This contrast mechanism is inherently sensitive to tissue composition, which means that in MRI the contrast between tissues of similar density is greater than that obtained with CT. Improving tissue-specific contrast with MRI is still an active research area. Fig. 1.2 (b) shows an MRI image of a transverse cross-sectional view of a CA that contains a plaque within the bifurcation.

As in CT, in US the contrast originates mainly from density differences between tissues. US images are made with a transducer that transmits short ultrasonic pulses (above the audible frequency range i.e. >20 kHz) that are then reflected by the tissue. These echoes are then recorded by the same transducer. The delay between transmitting the wave and receiving the echoes defines where the tissue is located. How well these pulses are reflected depends very much on the density differences in the tissue. An example of a transverse US image of an occluded CA is shown in Fig. 1.2 (c). Current clinical carotid scanning methods are limited.

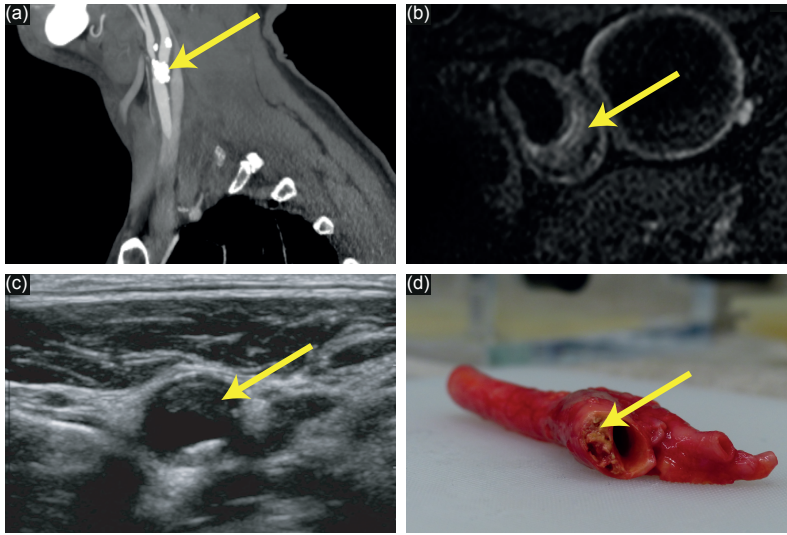


Figure 1.2: **Current clinical imaging of carotid atherosclerosis** The major techniques for carotid plaque imaging include X-ray computed tomography (CT), magnetic resonance imaging (MRI) and ultrasound (US). (a) A heavily calcified plaque inside the left carotid artery bifurcation as shown by CT angiography. (b) A transverse image made with MRI of a plaque growing inside the carotid artery. (c) A transverse US image of a large plaque inside the common carotid artery. (d) An ex vivo carotid artery with a plaque in the bifurcation.

CT is relatively expensive, uses harmful ionizing radiation and provides poor contrast between the soft tissues that are most important for determining plaque vulnerability. Although MRI provides a far better contrast between different tissue types, it also has disadvantages: it is expensive; it requires helium, which is a scarce resource; and it involves lengthy scanning procedures. MRI also has poor time resolution and therefore cannot capture the dynamics of CA motion and of the plaques within. With regard to the third imaging method used in current clinical practice, US carotid scanning lacks 3D spatial information, which is a major disadvantage in plaque assessment. However, unlike in MRI, in US imaging the time and spatial resolution required for providing information about plaque vulnerability is relatively good.

1.3 New developments and unmet needs in imaging

Using the current techniques, both early detection of plaques and reliable vulnerability assessment remain elusive, despite recent advances in carotid imaging. This is because all of the available methods lack either resolution in terms of plaque morphology, or specificity in terms of plaque composition [117]. The high costs, which limit accessibility, are an additional issue relevant to CT and MRI. Screening of people with advanced atherosclerosis, as well as those at risk, requires an imaging modality that has the following properties: it should be cheaper and faster than MRI and CT; it should be able resolve plaques

at an early stage; and it should have higher time resolution than CT, MRI and conventional US.

There is therefore clearly a need for carotid imaging that is low cost; that has a spatial resolution adequate for visualizing morphology; that is fast enough to capture dynamic phenomena that aid understanding of tissue structure and function; and that provides adequate information on tissue composition.

This thesis demonstrates that these requirements could potentially be met using high-frame-rate imaging (HFRI) and photo-acoustic (PA) imaging of the carotid artery. Both imaging techniques could be easily integrated into a single multimodality scanner that is affordable and can be used to scan people far more quickly than currently possible using CT or MRI. A brief discussion of HFRI and PA imaging will outline the role of these techniques in carotid artery diagnostics.

High frame rate imaging reveals plaque dynamics

When studying the carotid artery wall, biomechanics is important for two reasons. Firstly, in early plaques, the local biomechanical properties of the arterial wall change due to the accumulation of heterologous material and the breakdown of elastin and collagen [145, 71, 50, 112]. Secondly, these local biomechanical properties determine the chances of plaque rupture [19, 53, 28, 141]. The local biomechanics can be probed by imaging the tissue velocity in response to variations in systemic pressure [61, 32]. For the carotid artery, these pressure variations induce velocity gradients along the tissue of the artery wall. It is an interesting hypothesis that a measurement of the local tissue velocity in the arterial wall can detect early plaques and assess plaque vulnerability. The typical length scales and tissue velocities involved in such measurements require high temporal (< 1 ms) and spatial resolution (± 1 mm) [93]. The only imaging tool available today that can fulfil both requirements is high frame rate ultrasound imaging (HFRI) [102, 153, 161, 60, 37]. Fortunately HFRI has currently become available for clinical evaluation. However, the methods used to translate HFRI scans into useful and reliable arterial motion measurements and subsequently visualize them are still premature and in many cases insufficient. The first aim of the work presented in this thesis was therefore to develop imaging methods that allow the measurement of local tissue motion in the CA wall using HFRI.

The high-quality images that are obtained with conventional US scanners (Fig. 1.2 (c)) are made using many transmit-receive events (>100). However, US images can also be made with only a few transmit-receive sequences (sometimes only one). In this configuration, all elements in a transducer produce a single wave (in our case a plane-wave) that insonifies the entire tissue of interest. But because the transmit beam is unfocused, these images are of low quality and lack contrast and resolution [154]. The advantage of HFRI is twofold. Firstly, since the period between subsequent frames (images) is very short, there is strong consistency between frames. This frame-to-frame consistency can be exploited to detect very small changes in tissue displacement. Secondly, HFRI allows us to visualize processes that have fast dynamics, such as local arterial distension or heart movement.

For carotid plaque imaging using the HFRI technique, we focus on the imaging of tissue motion or tissue displacement. In conventional US and HFRI we measure tissue motion

by correlating the signals we receive for image A with the signals we receive some time later for, let us say, image B. If the tissue has moved in between the moments at which images A and B were taken, the echoes for image B will show a delay with respect to the echoes obtained for A (see Fig. 1.3 (b)). Using specialized correlation techniques we can not only measure these delays extremely accurately, but also derive the direction and magnitude of tissue motion from these delays. The principle of relating echo delays to tissue motion is the leading principle for the techniques that are described in the first part of this thesis.

Photoacoustic imaging reveals plaque composition

Plaques differ from healthy arterial tissue in their biochemical composition. Healthy arterial tissue contains collagen fibres and smooth muscle cells but not much lipid, for instance. From histological studies we know that atherosclerotic tissue composition varies greatly [164]. We also know that the accumulation of certain lipids inside plaques is associated with plaque vulnerability [149, 77]. However, the clinical imaging modalities currently available cannot visualize the low levels of lipids inside plaques. This information could potentially be provided by a promising new technique called photoacoustic (PA) imaging. The hypothesis is that PA imaging of the carotid artery wall can be used to visualize lipids, thereby revealing early plaque development and plaque vulnerability. The second aim of this work was to develop PA imaging of the CA wall.

Whereas in US imaging we transmit and receive acoustic waves, in PA imaging we transmit laser light and receive ultrasonic waves, which are then used to create an image. When the tissue absorbs the light, the tissue expands very rapidly, thereby creating a short ultrasonic wave that can be detected with the same transducer that is used for US imaging. The ultrasonic wave provides three pieces of information. Firstly, the time period between light delivery and acoustic detection tells us where the tissue is located. Secondly, the amplitude of the acoustic signal provides information about the optical absorption strength of the tissue. Thirdly, the frequency of the signal provides information about the size of the absorbing tissue structure. Since the optical absorption spectrum of tissue is directly related to its biochemical makeup, this technique provides access to the biochemical composition of arterial plaques. Figure 1.4 (b) shows the optical absorption spectrum for different types of tissue. The PA imaging technique has not yet reached clinical practice, but its potential for use in vascular imaging has already been demonstrated [139, 7, 167, 75, 78, 77]. Applying PA imaging to the CA in order to image tissue composition is the topic of the second half of this thesis.

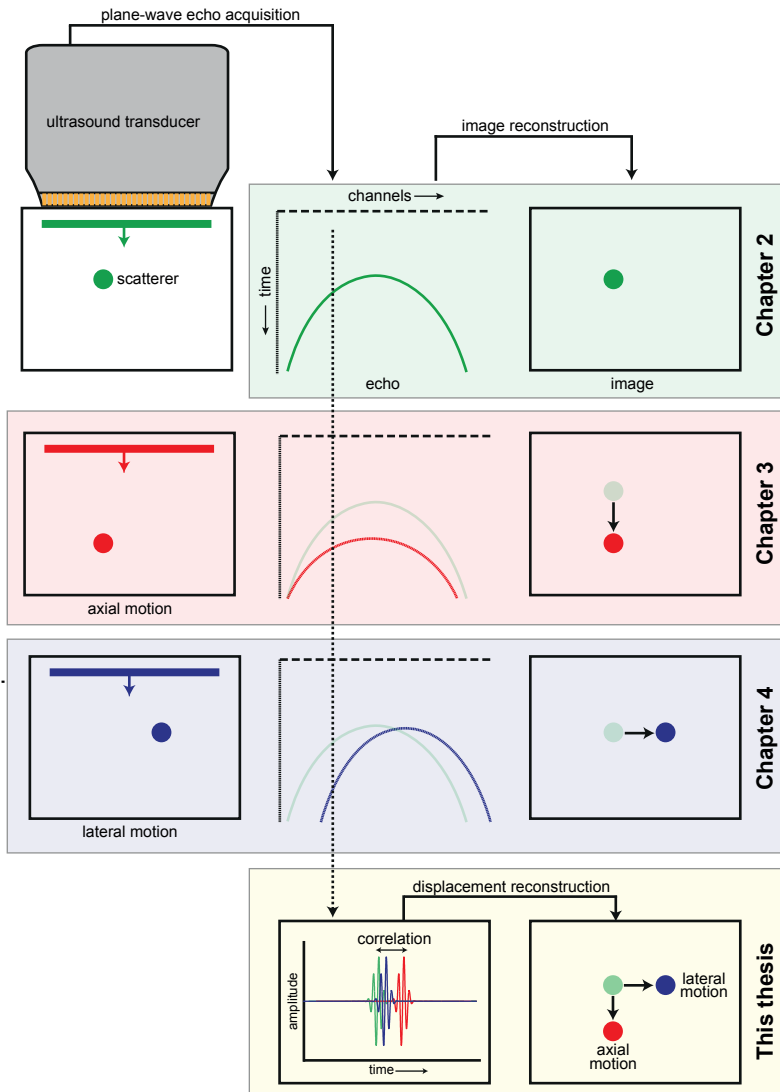


Figure 1.3: **HFRI technique** High-frame-rate ultrasound images can be created using a single plane-wave transmission that is followed by image reconstruction using the echoes recorded by a linear array. Chapter two (green) of this thesis focuses on the imaging reconstruction. When a scatterer moves in the axial direction, the echo will be displaced. Using echo correlation we can relate this delay to the scatterer motion. Chapter 3 (red) presents a method for measuring axial motion in the carotid artery. Lateral movement is difficult to measure with ultrasound imaging. In chapter 4 (blue) a method is introduced for measuring lateral motion in the carotid artery.

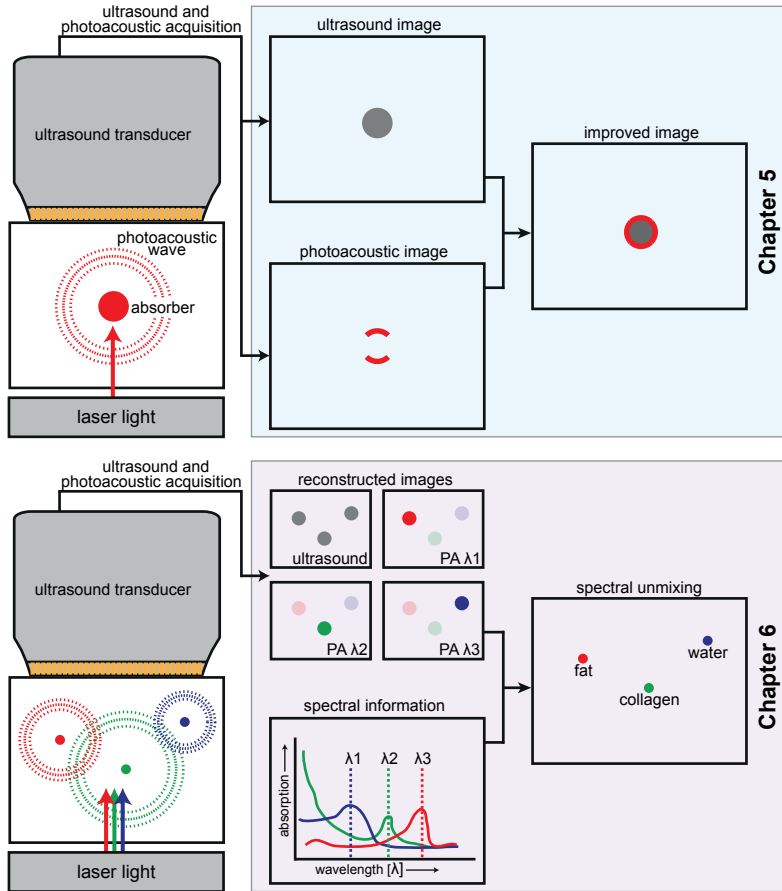


Figure 1.4: **PA imaging technique** In photoacoustic imaging pulsed laser light is converted into acoustic waves that can be recorded by an ultrasound transducer in order to create an image. Conventional image reconstruction can be improved by using information from an additional ultrasound image as is shown in chapter 5 (top part). The photoacoustic signal strength depends on the optical absorption spectrum, which is specific for each tissue type. In chapter 6 the PA signal at different wavelengths is related to tissue composition inside the carotid artery wall (lower part).

Thesis outline

This thesis describes the development of several new techniques for imaging tissue motion, based on ultrasound high-frame-rate imaging. One difficulty with the high-frame-rate imaging technique is the enormous amount of data that it produces. In chapter two, a fast and accurate image reconstruction method is applied to high-frame-rate image data that deals with this issue. This method forms the basis for an algorithm to estimate axial (towards-and-away-from the transducer) tissue motion, which is described in chapter three. This motion-algorithm was tested on carotid arteries in longitudinal view in a group of healthy volunteers and in two patients with known atherosclerosis. The HFRI data presented in this chapter visualize the tissue dynamics in unprecedented detail. The difficulty of estimating lateral (left-and-right)

tissue motion was solved with a new method that is presented in chapter four. This method was successfully tested on the carotid artery of a healthy volunteer.

In the second part of this thesis it is shown how photoacoustic imaging can be used to reveal the biochemical composition of the arterial wall. Despite the difference in contrast mechanisms between ultrasound and photoacoustic imaging, the images provided by these techniques also have interesting overlap. This overlap is the subject of chapter five, which describes how to improve photoacoustic image reconstruction using information derived from a complementary ultrasound image. This technique could potentially be used to reveal small plaques within the arterial wall.

The proof that photoacoustic imaging can indeed reveal the biochemical composition of the artery wall is provided in chapter six. In this chapter, images of a diseased artery embedded in a neck-mimicking phantom are captured using a small optical probe and a normal ultrasound transducer. To apply this concept in patients it will be necessary to illuminate the carotid via a small probe inside the throat and to place a transducer in the neck.

The final chapter, chapter seven, examines the newly developed ultrasound methods and the prospects of photoacoustic imaging of the carotid artery. It concludes with an assessment of the requirements for photoacoustics to become a useful clinical tool.

Part I

**High frame-rate imaging reveals
plaque dynamics**

Fourier domain image reconstruction

This chapter has been published as:

Pieter Kruizinga, Frits Mastik, Nico de Jong, Antonius F.W. van der Steen, and Gijs van Soest, Plane-wave ultrasound beamforming using a nonuniform fast Fourier transform, *Ultrasonics, Ferroelectrics and Frequency Control, IEEE Transactions on* 59, no. 12 (2012).

Abstract

Beamforming of plane-wave ultrasound echo signals in the Fourier domain provides fast and accurate image reconstruction. Conventional implementations perform a k -space interpolation from the uniform sampled grid to a non-uniform acoustic dispersion grid. In this paper, we demonstrate that this step can be replaced by a non-uniform Fourier transform. We study the performance of the non-uniform fast Fourier transform (NUFFT) in terms of signal-to-noise ratio and computational cost, and show that the NUFFT offers an advantage in the trade-off between speed and accuracy, compared to other frequency-domain beamforming strategies.

2.1 Introduction

Lately μm μm the method of plane-wave transmission and post-acquisition beamforming has attracted renewed attention. The high frame rates that can be achieved with plane-wave imaging have enabled powerful new functional imaging modalities [113, 110]. Jian-yu Lu and coworkers demonstrated that beamforming of limited diffraction beams (such as a plane wave) can be significantly sped up when evaluated in the Fourier domain. Such methods are of benefit especially in cases where full axial resolution should be retained, for example motion detection in high frame rate imaging with advanced phase tracking algorithms. Practically, one performs a two-dimensional (2D) fast Fourier transform (FFT) of the received echoes, followed by an interpolation of the Fourier data to an acoustic dispersion grid $k_z = \sqrt{k^2 - k_x^2}$ and a 2D inverse fast Fourier transform (IFFT) to obtain the beamformed signals. For a schematic overview of this method see Fig 2.1(a). Lu *et al.* supported this method by extensive theoretical and experimental studies [102, 103, 20].

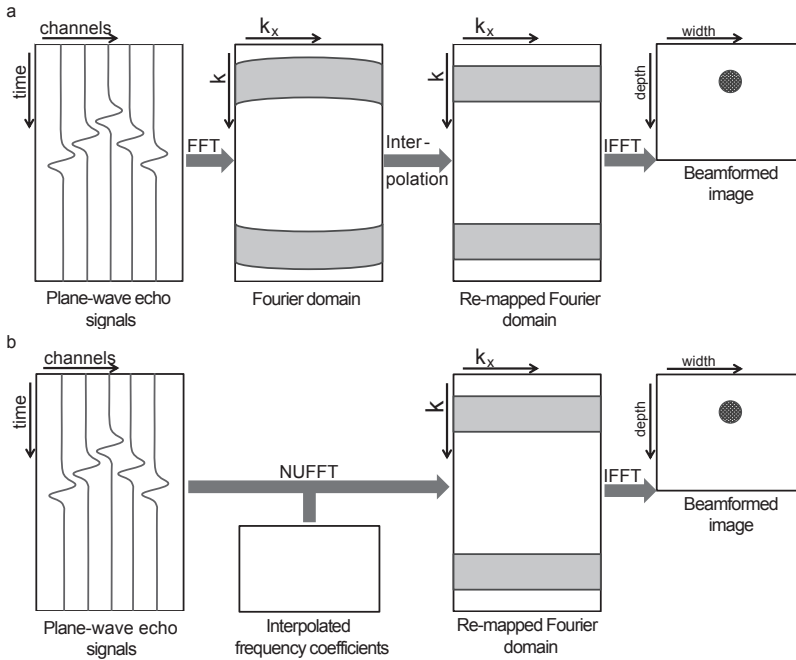


Figure 2.1: Schematic overview of (a) Lu's remapping method, and (b) the proposed NUFFT method.

When a plane-wave is used to insonify the medium, the received echo signals can be beamformed in the Fourier domain. The frequency or k -space representation of the echoes in the Fourier domain is such that the wavenumber k is defined as $k = \omega/c$, where $\omega = 2\pi f$ denotes the angular frequency and f the temporal frequency. When a 2D FFT is applied to the received signals we have k in the time dimension and k_x , the lateral component of k , $k_x = \frac{2\pi}{\text{pitch}}$, where pitch is the center-to-center distance between two neighbouring elements. In a pulse-echo experiment, the recorded spectrum R contains both the transmitted wave vector $k_T = (k_{Tz}, k_{Tx})$ as well as the received echo wave vector $k_R = (k_{Rz}, k_{Rx})$. To obtain a

beamformed image of the object we have to re-map the received spectrum $R(k_{tz}, k_{tx}, k_{rx})$ to the frequency grid of the object denoted by $O(k_z, k_x)$. The k -domain dependencies are schematically represented in Fig. 2.1. In the situation of pulse-echo plane wave transmission, steered under angle θ , the relation between both spectra is:

$$k_{rx} = k_x - k \sin \theta \quad ; \quad (2.1)$$

$$k = \frac{k_z^2 + k_x^2}{2k_z \cos \theta + 2k_x \sin \theta} \quad . \quad (2.2)$$

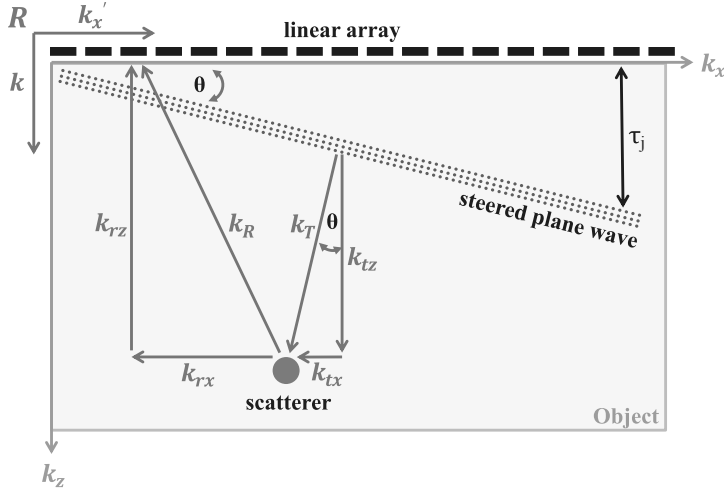


Figure 2.2: Schematic representation of the k -domain wave vectors

A plane wave can be steered by applying increasing time delays to every subsequent element of the transducer array, denoted in the figure by τ_j . When the received echo signals are reversely time-shifted by τ_j (which equals a shift in k_x), $R(k_{tx}, k_{rx})$ will completely coincide with $O(k_x)$, eliminating the need for interpolation in spatial frequency direction. Furthermore, the evanescent field, associated with $k^2 < k_x^2 + k_z^2$ should be set to zero using the boundaries provided by $|k_x| \leq k$ [20, 25].

Direct application of an IFFT on data that is non-equidistantly sampled may create artefacts and loss of signal [150, 57, 137, 16]. Ideally, the frequency samples are remapped to the object grid O_{k_z, k_x} before an 2D IFFT can be applied to get the beamformed signals.

Several solutions have been proposed to handle the error introduced by application of Fourier methods to a non-uniformly spaced R -grid. A straightforward solution is to increase the sampling density in the Fourier domain (e.g. by zero-padding the echo data [124, 174, 101]). This operation reduces the interpolation error, hence the beamforming will be more accurate. Another method symmetrizes the recorded signals around $t = 0$, through which the *sine* terms of the FFT will integrate to zero leaving only interpolation errors with the *cosine* terms [57]. In this paper, we propose to beamform the data in k -space using a *nonuniform Fourier transform*. In this study we demonstrate that the non-uniform fast Fourier

transform (NUFFT) is an accurate and computationally efficient algorithm to perform image reconstruction for plane wave ultrasound imaging.

The observation that motivated this work is the successful application of different NUFFT approaches in various medical image reconstruction settings, such as in MRI, where the signals can be acquired at selected points in the frequency domain [52, 152, 45, 132], frequency domain OCT [170, 179] and CT [119]. In the field of medical acoustics the usefulness of the NUFFT has been demonstrated in reconstruction of photoacoustic images [57, 137], and in simulations of ultrasound tomography imaging [16, 177, 178].

In this paper we propose to apply the NUFFT in plane wave ultrasound beamforming. We compare the NUFFT approach with other established frequency remapping methods. In Fourier domain beamforming of acoustic signals, regularly sampled data in k -space need to be remapped to a non-uniform acoustic dispersion grid. This is achieved by interpolating the uniformly spaced samples to the nonuniform sample locations. Instead of k -space interpolation of the grids, it is possible to directly calculate the non-uniform Fourier transform by means of the nonuniform discrete Fourier transform (NDFT) [45]. The NDFT has the form:

$$X(\omega_m) = \sum_{n=0}^{N-1} x_n e^{-i\omega_m n}, \quad m = 1, \dots, M, \quad (2.3)$$

where x_n are equally-spaced signal samples, ranging from 1 to N and ω_m , the nonuniformly spaced frequency nodes ranging from 1 to M . The Fourier transform thus needs to be computed for every nonuniform frequency node. The result of the NDFT is exact but has a computational cost of $O(MN)$ operations. In real-world applications, the computation time required by the NDFT will be too large to be practical. The NUFFT is an approximation of the NDFT that allows a fast solution to the non-uniform transform problem. Since the introduction of the technique by Dutt and Rokhlin [36] in 1993, several NUFFT methods have been proposed [14, 98]. The NUFFT was extended to multidimensional transforms [132, 52], and actual software implementations were published [128, 84, 57]. In this study we will use the NUFFT implementation by Fessler *et al.* [45].

Mathematically the NUFFT can be described by:

$$Y_k = \sum_{n=0}^{N-1} x_n e^{-i(2\pi/K)kn}, \quad k = 1, \dots, K-1, \quad (2.4)$$

$$\hat{X}(\omega_m) = \sum_{j=0}^J Y_{(k_m+j)} u_j(\omega_m), \quad m = 1, \dots, M, \quad (2.5)$$

where Y_k denotes the resampled FFT with K points of signal x and $\hat{X}(\omega_m)$ is the approximated nonuniform frequency samples of signal x . The $u_j(\omega_m)$'s are the appropriate frequency interpolation coefficients [45]. Determining the optimal interpolation coefficients and applying them in a computationally efficient manner (through pre-computing) is key to all NUFFT methods.

The main advantage of the NUFFT with respect to the NDFT is its computational

efficiency. The major argument for using the Fourier domain approach instead of conventional delay-and-sum (D&S) beamforming is about the computational gain. Considering simple D&S beamforming we have a computational complexity of $N_e N_s N_e$, where N_e are the number of transducer elements and N_s are the number of samples of the beamformed signals. The frequency remapping method proposed by Lu *et al.* comprises a 2D FFT, an interpolation and a 2D IFFT. This comes down to a computational load of $N_e N_s S \log(N_e N_s S) + N_e N_s S + N_e N_s S \log(N_e N_s S)$, where S is the sample densification factor in the time direction. Without pre-computation (selecting the correct interpolation coefficients) the NUFFT by Fessler *et al.* offers a computation count of only $K \log N + JM$, where K denotes the number of resampled frequency locations (typically $K \approx 2N$) and J , the neighbourhood size used in the interpolation. The total computational load for the whole beamforming procedure would therefore be: $N_e K \log(N_s) + N_e N_s \log(N_e) + J N_s N_e + N_e N_s \log(N_e N_s)$. The first two terms arise from a NUFFT for each channel over all samples on the K/N upsampled grid, and a regular FFT for all N_s frequency nodes over all channels, the third is the computation of the interpolation coefficients, and the last comes from the 2D IFFT. If we consider a fixed imaging depth of 8192 samples, roundtrip and linear interpolation ($J = 1$), we can evaluate the computation time as a function transducer elements at a 1 Teraflops operation benchmark. Fig. 2.3 shows the computation times for the various beamforming methods.

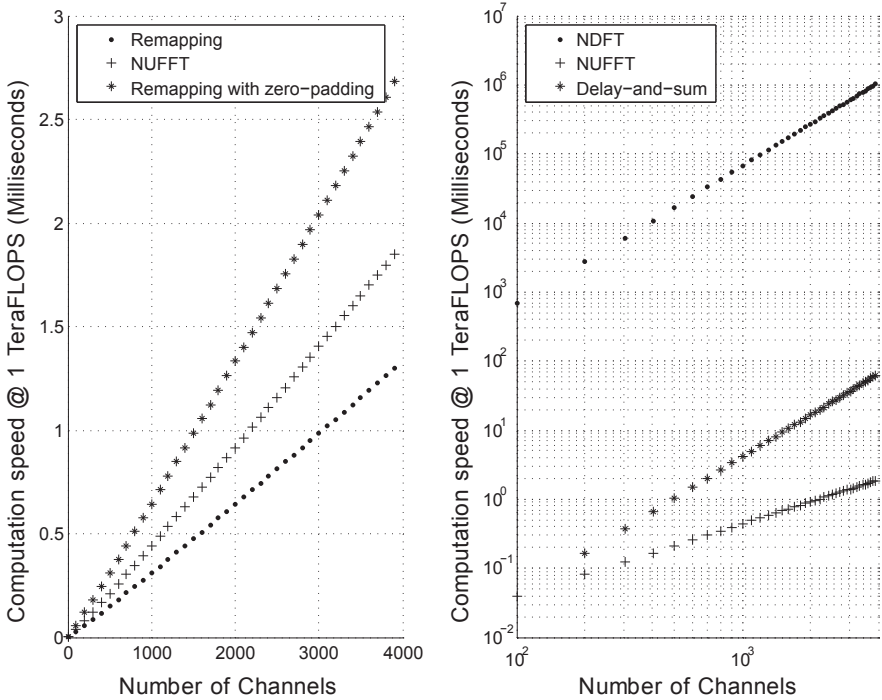


Figure 2.3: Theoretical values of computation speed at one Teraflops considering the operations needed for the various beamforming methods

2.2 Methods and Materials

Experiment

We compared both Fourier resampling methods using experimental data that was obtained by plane wave imaging of an ultrasound phantom by CIRS Inc. (Model: 040GSE [1]) and of a home-built wire phantom. The wire phantom contained 15, 90 μm nylon wires in water, diagonally positioned in depth with an axial inter-wire spacing of 10 mm and a lateral spacing of 2 mm. See Fig. 2.4 for a schematic of both imaging phantoms. A broadband linear array with 192 elements, from which the middle 128 were connected, (pitch: 245 μm , bandwidth: 4-9 MHz (Vermon, Tours, France) was interfaced with an open 128 channel ultrasound system (Lecoeur Electronique, Chuelles, France). In transmit a Gaussian-envelope pulse of 1.5 cycle, with a center frequency of 8 MHz was used. The acquisition depth was set to 100 μs , roundtrip, using 80 MHz sampling at 12 bits. For the nylon-wire-in-water experiment a sampling frequency of 40 MHz was used. For the tissue phantom experiment we used a time-gain-compensation ranging from 25 to 75 dB.

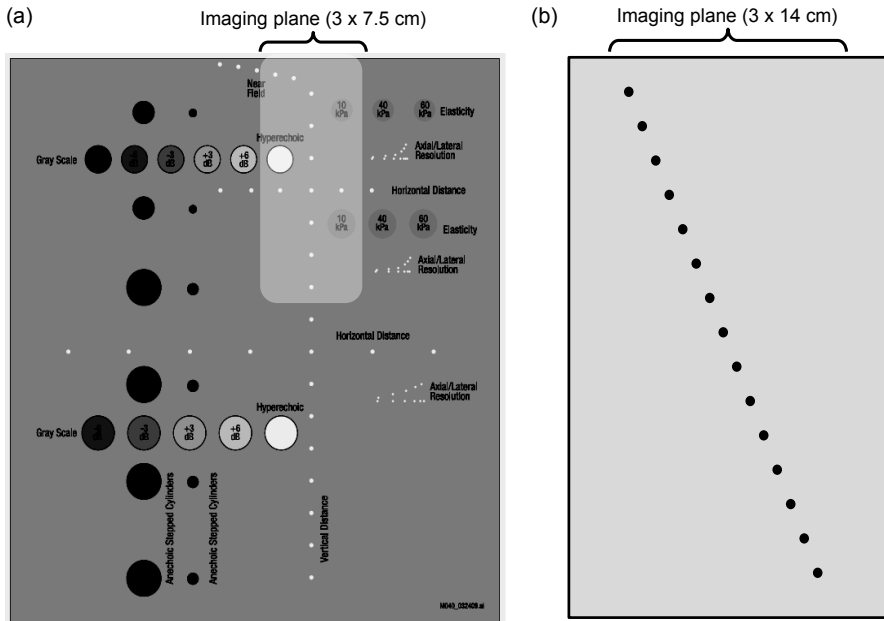


Figure 2.4: Schematic drawing of (a) the tissue mimicking phantom by CIRS and (b) home-built wire-phantom.

Image Reconstruction

We evaluate the performance of two Fourier beamforming methods, compared to the exact NDFT. The metrics used to assess performance are signal-to-noise ratio (SNR) and computation time. For image purposes, the envelope of the unfiltered beamformed signals was determined which then was normalized with respect to the maximum envelope value before logarithmic compression was applied. The image reconstructions were done using

Matlab R2011a on a 3 GHz dual-core office PC.

A dedicated experiment to evaluate computational efficiency was implemented on a desktop PC running Matlab 2011b (The Mathworks, Natick, MA) with Jacket v2.0 (AccelerEyes, Atlanta, GA) and a Tesla C1060 graphics card (NVIDIA, Santa Clara, CA) with 4 Gb of memory. We beamformed a synthetic data set consisting of 100 frames and varied the number of samples and channels to see the effect on the overall processing time. The processing times were measured using Matlab *tic/toc* timing functions. The median time over 30 runs was considered as a robust frame processing time estimation. For the *graphics processing unit* (GPU) implementation we developed our own code in which we considered linear remapping with an indexed lookup table that could be stored separately.

Frequency remapping method

The frequency sample remapping method proposed by Lu *et al.* was implemented as follows: a 2D FFT was applied to the received echoes. The frequency samples were interpolated, using linear interpolation, to the object grid using the relations (2.1) and (2.2). Alternatively, the echo data was zero padded in the time dimension (appending zeros to the end of the recorded signals) in order to minimise the interpolation error. A 2D IFFT was subsequently applied to obtain the beamformed signals.

NUFFT

For this study, we chose a reasonably fast, and accurate, NUFFT implementation by Fessler and Sutton [45]. Advantages of this particular NUFFT are its proven low error-count, low level of complexity and the existing implementation in Matlab [152, 2]. Like most NUFFT methods, Fessler's NUFFT uses an upsampled FFT in combination with a frequency-domain interpolation to find the nonuniform frequency samples.

To find the optimal interpolation coefficients, Fessler *et al.* formulated a min-max criterion in the sense that the maximal approximation error (between X_m and $\hat{X}(\omega_m)$) over all signals x is minimal when a specific set of interpolation coefficients is chosen. This min-max criterion thus requires that for every nonuniform frequency location ω_m the interpolation coefficients should first be computed before selecting the right set of coefficients. Advantageously, these interpolation coefficients can be precomputed and stored to minimize the operation count of the NUFFT.

The NUFFT Matlab implementation provided by Fessler *et al.* allows for a wide range of other interpolation methods to compute the frequency locations used in the NUFFT computation. For the image reconstruction comparisons we used either an upsampling factor of 2 with linear interpolation, or the aforementioned min-max interpolation, with a Kaiser-Bessel interpolation kernel, a neighbourhood size of 6 and no other scaling factors [45]. All interpolation coefficients were pre-computed and stored. The beamformed images were obtained by applying a regular 1D FFT in the spatial dimension, and a 1D NUFFT for all channels independently in the time or depth dimension. A regular 2D IFFT was used to obtain the beamformed signals.

NDFT

As discussed in the introduction, exact Fourier domain beamforming can be performed using the NDFT. We use this image reconstruction method as our SNR benchmark for evaluating the performance of the other techniques. The beamforming procedure was similar to that of the NUFFT, however the actual NUFFT was replaced by a straightforward implementation of (2.3).

Delay-and-sum

For completeness we included a beamformed image obtained with the delay-and-sum (D&S) method. D&S can be realized in various schemes, optimizing sampling, apodization and other parameters for speed and beamforming accuracy. For the purpose of this paper, comparing frequency domain beamforming methods, we did not consider these details. For every beamformed sample we simply choose for all channels j the nearest samples for which the delay satisfies $\tau(x_j, x, z) = [\sqrt{(x - x_j)^2 + z^2} + z]/c$, where z denotes the depth and x the lateral direction; x_j is the location of the j th element. For an extensive discussion of D&S beamforming in plane-wave ultrasound see [113].

2.3 Results

Image reconstruction

A comparison of the performance of the beamforming techniques for imaging small hyperechoic targets was obtained by plane-wave ultrasound imaging of the vertical distance group of the CIRS phantom (see Fig. 2.4(a)). Figure 2.5 was obtained by beamforming one, zero-angle plane-wave insonification, reconstructed by the conventional D&S methods and the exact NDFT.

A further comparison of Fourier transform beamforming techniques is displayed in Fig. 2.6. It concerns the normal remapping method proposed by Lu *et al.* and the NUFFT method with a two times upsampled grid and a Kaiser-Bessel min-max interpolator with a neighbourhood size of 6.

The SNR differences between the various reconstruction techniques may be evaluated by considering a more controlled experiment (a localized scattering object in water at 20°C). We studied the image reconstruction of the last (deepest) positioned nylon wire of the wire phantom (See Fig. 2.4); results are shown in Fig. 2.7. The comparison is made between five Fourier resampling approaches: the NDFT, linear remapping, linear remapping with a twofold increased sampling density, the NUFFT method with linear interpolation based on a two times upsampled grid and the NUFFT method with a two times upsampled grid and a Kaiser-Bessel min-max interpolator with a neighbourhood size of 6. Image reconstruction using the exact NDFT is displayed in Fig. 2.7 (a). Sub-image (b) in Fig. 2.7 shows three different amplitude levels based on the image intensity values obtained with the NDFT method. These amplitude levels are used for the SNR comparison analysis. The SNR in all the five other images was calculated on the basis of the mean pixel value in the signal area (either [0 -6] or [0 -20] dB) and noise area (either [-6 -40] or [-20 -40] dB). The measured SNR values for the various methods are listed in Table 2.1.

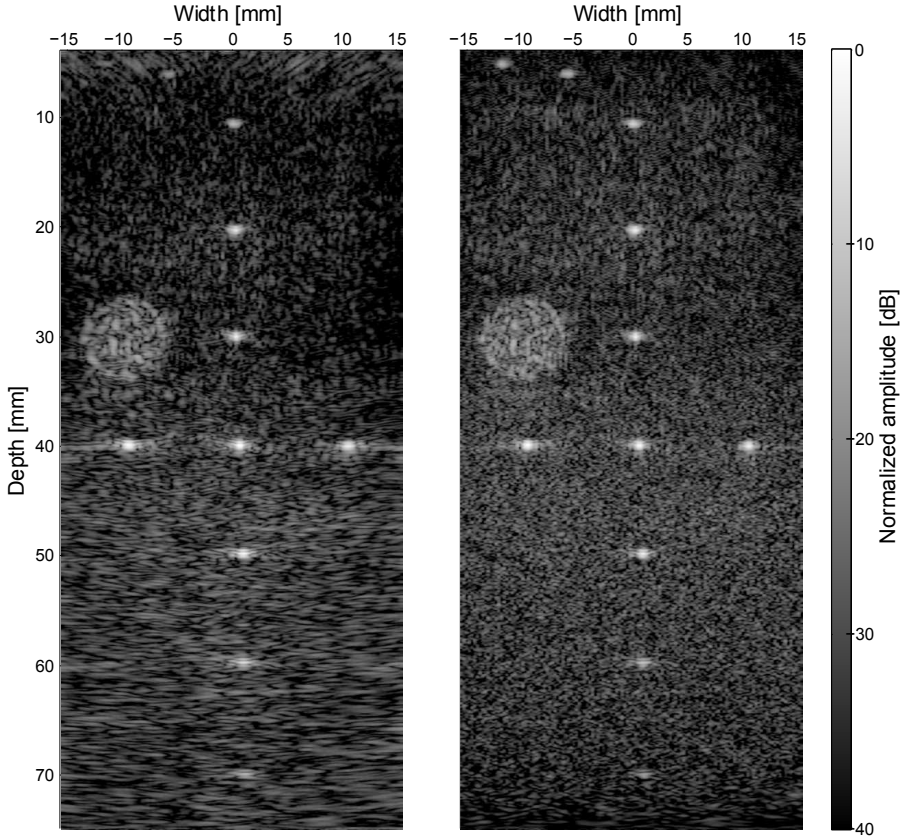


Figure 2.5: Plane-wave ultrasound images of small hyperechoic targets reconstructed by (left) delay-and-sum method, and (right) NDFT method.

Method	-6 dB	-20 dB
NDFT	27.2 dB	19.1 dB
Linear	22.8 dB	14.9 dB
Linear 2 x	26.8 dB	18.9 dB
NUFFT 2 x	27.0 dB	18.7 dB
NUFFT min-max	27.2 dB	19.1 dB

Table 2.1: Measured SNR values for the various Fourier resampling methods measured at the -6 and -20 dB signal levels.

Computational efficiency

The computational cost of the Fourier-resampling methods was assessed by measuring the processing time for an individual frame of a particular size (samples \times channels). We compared normal linear remapping, linear remapping with a twofold increased k-space cover-

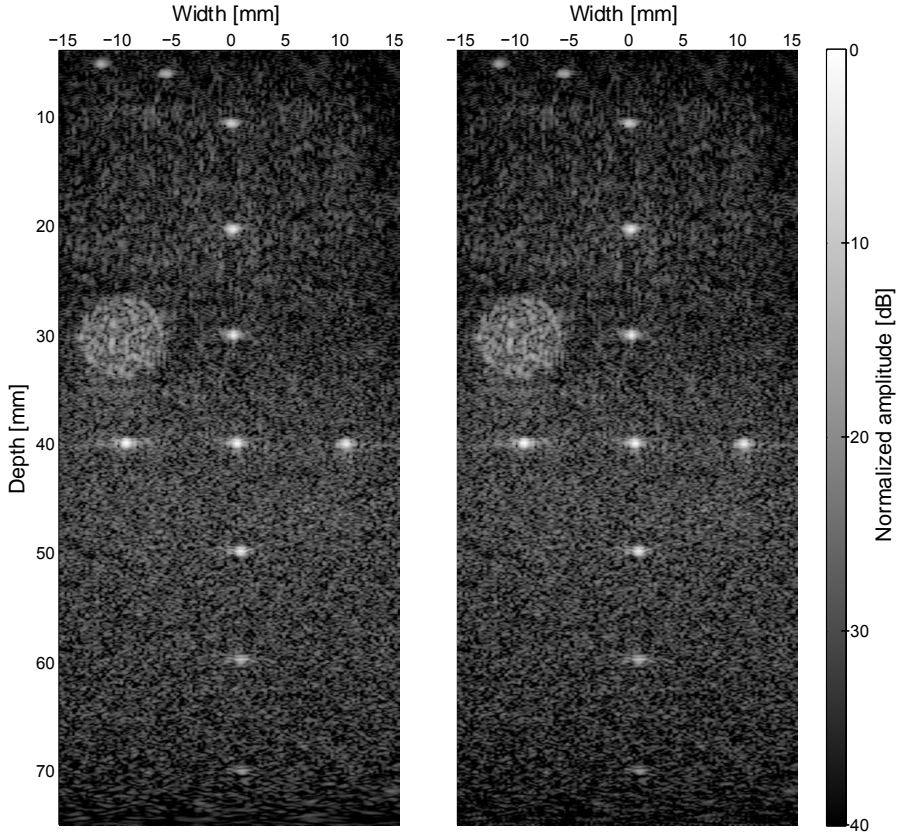


Figure 2.6: Plane-wave ultrasound images of small hyperechoic targets reconstructed by (left) Normal remapping method, and (right) NUFFT method.

age, the NUFFT method with linear interpolation based on a twofold upsampled grid, the NUFFT method using the min-max interpolator and our own GPU implementation using linear remapping. Table 2.2 shows the frame processing times (in milliseconds) for a small selection of frame sizes.

Method	2048× 64	1024× 128	2048× 128	4096× 128	8192× 128	2048× 256
Linear	32	52	68	113	177	144
Linear 2 x	46	66	93	193	305	212
NUFFT 2 x	35	56	74	133	215	159
NUFFT min-max	39	60	82	150	255	174
Linear GPU	0.38	0.37	0.84	1.9	4.5	2.0

Table 2.2: Overview of the processing times (in milliseconds) needed for the various Fourier-domain methods to beamform one frame (of size samples×channels).

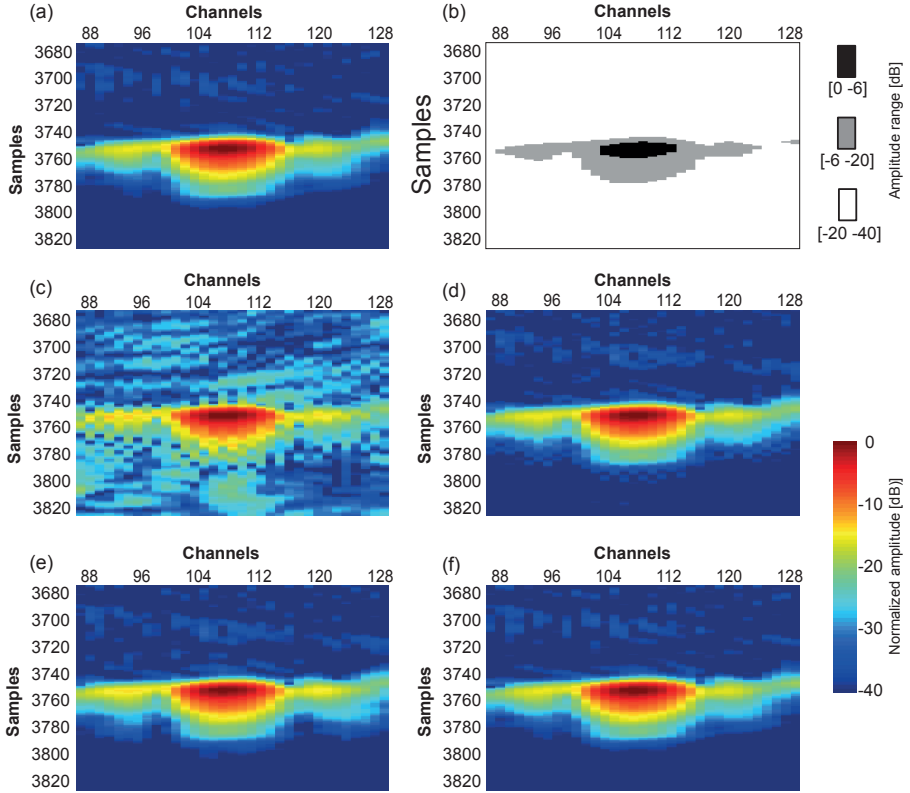


Figure 2.7: Plane-wave ultrasound image reconstruction of a $90\ \mu\text{m}$ nylon wire in water at a depth of 14 cm with (a) NDFT method, (b), SNR pixel plot based on amplitude levels in image (a), (c) Normal remapping method with linear interpolation, (d) linear interpolation with a $2 \times$ densification of the Fourier spectrum in the time dimension, (e) NUFFFT method with linear interpolation based on a twofold upsampled grid (f) NUFFFT method with a twofold upsampled grid and min-max Kaiser-Bessel interpolation.

2.4 Discussion

The comparison between D&S and NDFT beamforming displayed in Fig. 2.5 shows that the Fourier domain approach results in an even speckle size over the entire depth, and that all wires are reconstructed using the Fourier method, including those in the near field. With D&S, a similar result could probably be obtained when apodization and fine delay interpolation are applied. These adaptations should reveal the wires in the near field and produce a more evenly sized speckle. Nevertheless, it is interesting to observe that the Fourier domain method inherently incorporates these refinements. Fourier domain beamforming can be derived directly from the Green's function for the imaging system and hence produces a more accurate reconstruction of the actual scatterer distribution, without additional apodization and fine interpolation [102, 103, 20].

The relative differences in normalized amplitude between the linearly interpolated fre-

quency remapping method and the NUFFT with Kaiser-Bessel min-max interpolation are in the order of 5%. As a result, the advantages of either technique are not immediately apparent from a comparison like the one displayed in Fig. 2.6, which uses logarithmic compression to display a large dynamic range. Lu *et al.* similarly concluded that a two-fold densification of the echo data provided the best trade-off between image quality and computational cost [101]. The importance of accurate Fourier resampling becomes more pronounced, from the image reconstruction of a single scattering object in water, as shown in Fig. 2.7. Figure 2.7 (c) clearly shows that the error introduced by linear interpolation with no resampling performs causes a loss in SNR of about 4.5 dB with respect to the NDFT method. Increasing the sample density in the time dimension by a factor two improves the image quality considerably. The NUFFT method with linear interpolation based on a two times upsampled grid achieves a similar performance, emphasizing the importance of the interpolation scheme used in Fourier domain beamforming. This observation is corroborated by the performance of the NUFFT, an upsampling factor of two and the min-max interpolator, which replicates the SNR of the exact NDFT.

The data in Table 2.2, a selection of computation times for the various Fourier-resampling methods, demonstrates a speed-up of frame processing time by about 15% (average) using the NUFFT min-max method compared to the linear remapping with upsampling. The NUFFT reconstruction of an isolated scatterer is slightly more accurate (Table 2.1) at a lower computational cost. A second observation is the enormous reduction of processing time achieved by using a GPU. Fourier-domain beamforming could greatly benefit from the massive parallel processing power offered by a GPU system. Realizing these high beamforming frame rates with GPU's might open up new possibilities such as real-time 3D imaging. The NUFFT is an excellent fit for implementation on GPU systems [179, 148]. Implementation of the min-max interpolation on the GPU is currently ongoing and will offer the most accurate reconstruction with possibly kiloframes per second processing speed. In the case of GPU computing, there is time penalty for memory transfer from the host to the GPU and vice versa. Current technology progress aims to reduce this transfer time but for now it remains a significant bottleneck in practice.

Regarding Fourier domain beamforming, we found it instructive to see that the transmit and receive wave vectors, k_T and k_R , though both confined in k , can be treated separable. Changing one of them will have an effect on the beamformed image. When changing the transmission vector k_T , e.g. by changing the transmission angle θ , the phase and amplitude of the scatter source will be modulated accordingly. Compounding the resulting beamformed signals, either coherently (improving resolution) or incoherently (smoothing speckle) will improve the overall image quality. The change of k_T will thus have a physical effect that can be exploit to improve the image. Improvement can also be obtained when changing the reception wave vector k_R e.g. by applying linear delays in reception either pre- or post-acquisition [104, 55].

Both the remapping method and the NUFFT method rely on interpolation of complex Fourier data. As the basis for image formation is the reconstruction of a propagating wave, the physically meaningful quantities that need to be accurately represented are the amplitude and phase of the wave. We found that interpolation of the *real* and *imaginary* parts of the data, as opposed to interpolation of *magnitude* and *phase*, introduces a significant error in

the reconstructed image. Figure 2.8 illustrates the reconstruction of our test target for linear interpolation of the real and imaginary part of the spectrum, compared to linear interpolation of the magnitude and phase. Interpolation of the real and imaginary parts of the spectrum results in a strongly reduced viewing depth.

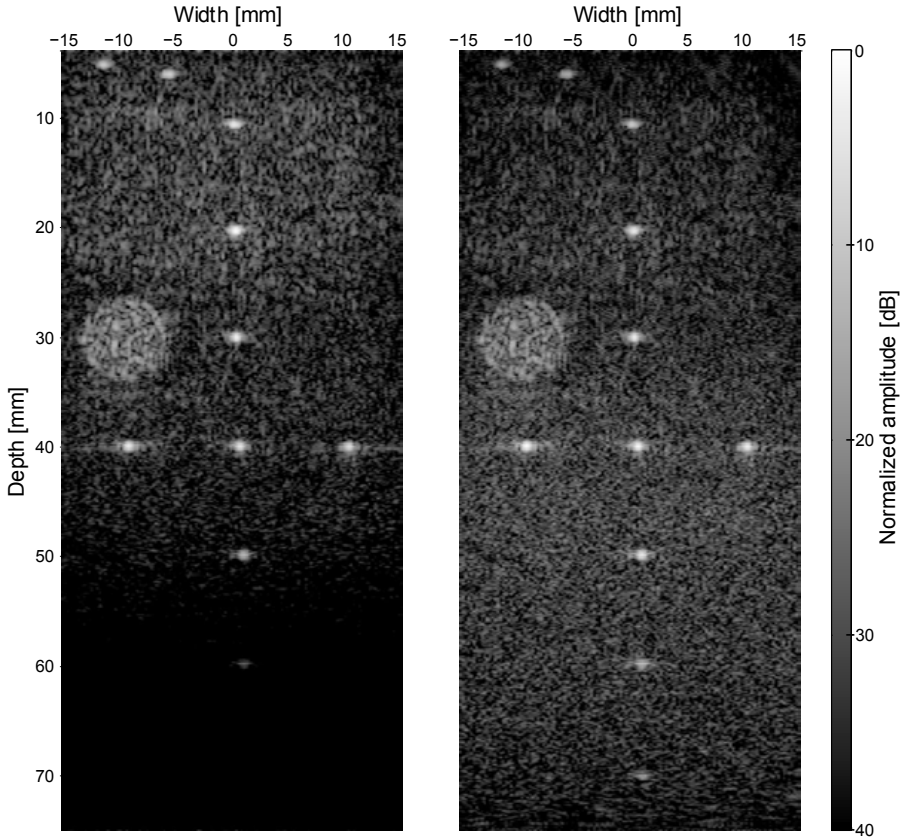


Figure 2.8: Plane-wave ultrasound images of small hyperechoic targets reconstructed by (left) linear interpolation of the *real* and *imaginary* parts, and (right) linear interpolation of the *magnitude* and *phase*.

Besides the beamforming algorithm, there are other factors which affect image quality. The band-limited transmission pulse, a finite transducer aperture with only 128 elements, 12-bits digitization, frequency dependent attenuation, and the assumption of a fixed speed of sound, limit the improvement that can be achieved through more accurate image reconstruction. Nevertheless, we think that the continuing evolution of ultrasound technology (increasing number of channels (3D), increased transmit and receive bandwidth, increased SNR and more refined applications for fast plane wave imaging) will necessitate an accurate and fast Fourier domain beamforming method, and the NUFFT is a highly suited candidate to fulfil this goal.

2.5 Conclusion

We successfully applied a non-uniform FFT to Fourier domain beamforming in plane-wave ultrasound imaging. For the inverse Fourier beamforming problem of plane wave ultrasound the NUFFT offers a fast and accurate solution compared to the earlier proposed remapping method.

Acknowledgment

The authors would like to thank Prof. Jeffrey A. Fessler and Prof. Jian-yu Lu for enlightening discussions and implementation details on the NUFFT and plane-wave beamforming respectively. We also thank Robert Beurskens for his technical support on the Lecoeur system and Michiel Manten for construction of the wire phantom.

Imaging carotid artery wall dynamics

This chapter has been published as:

Pieter Kruizinga, Frits Mastik, Stijn C.H. van den Oord, Arend F.L. Schinkel, Johannes G. Bosch, Nico de Jong, Gijs van Soest and Anton F.W. van der Steen, High-definition imaging of carotid artery wall dynamics, *Ultrasound in Biology & Medicine* 40, no. 10 (2014).

Abstract

The carotid artery (CA) is central to cardiovascular research, because of the clinical relevance of CA plaques as culprits of stroke and the accessibility of the CA for cardiovascular screening. The viscoelastic state of this artery, essential for clinical evaluation, can be assessed by observing arterial deformation in response to the pressure changes throughout the cardiac cycle. Ultrasound (US) imaging has proven to be an excellent tool to monitor these dynamic deformation processes. We demonstrate in this paper how a new technique called high frame rate US imaging captures the tissue deformation dynamics throughout the cardiac cycle in unprecedented detail. Local tissue motion shows distinct features of sub-micrometer displacements on a sub-millisecond time scale. We present a high definition motion analysis technique based on plane wave US imaging able to capture these features. We validated this method by screening a group of healthy volunteers and compared these results to two patients with known atherosclerosis to demonstrate the potential utility of this technique.

3.1 Introduction

The healthy artery wall is a layered structure with non-linear elastic properties, that enable it to sustain rapid and large variations in blood pressure [140]. Muscular arteries, such as the carotid and coronary arteries, respond actively and passively to the systemic pressure cycle, modifying their diameter or tone to physiological circumstances. Under the influence of age and chemical and mechanical stresses, the artery wall may be affected by atherosclerosis, a systemic inflammatory disease that leads to the formation of plaques consisting of calcifications and lipid-rich necrotic material. Lipid-rich plaques may become unstable and rupture, in which case an atherothrombotic reaction can lead to cerebral or cardiac ischemic events [18, 162, 134, 146]. Advanced atherosclerosis also compromises vascular function and elastic response of the arteries, in a phenomenon known as arterial stiffening. Loss of elasticity of the arterial wall may result in systemic arterial hypertension [121]. A full assessment of vascular elasticity as well as plaque stability requires mapping of the local biomechanical properties of the artery wall: atherosclerosis is heterogeneous in its prevalence and severity. Soft plaques are more prone to rupture than stiff ones [53, 28, 141] and arterial stiffness varies throughout the body. Local biomechanics can be probed by imaging the tissue velocity in response to the systemic pressure variations.

Those local variations are critical for plaque stability: a rupture will occur if the weakest point lacks sufficient strength to withstand the applied stress, a condition which cannot be gauged by average measurements [19, 28, 134]. Especially locations with large tissue strain are prone to rupture. The amount of tissue deformation can be obtained by measuring the tissue velocity under varying load [61, 136, 32]. In this paper we aim to measure the tissue velocity of the carotid artery (CA) wall. The CA is important because of high incidence of atherosclerosis in this artery, the strong association with cerebrovascular events [54, 96] and the relation between atherosclerosis in the CA and atherosclerosis in other vascular beds, such as the coronary arteries [159, 100, 62, 72]. The CA is also superficially located making it an ideal imaging target for screening applications.

Arteries can also become stiff, thereby losing the ability to support large and rapid pressure variations. The most reliable indicator of arterial stiffness is thought to be arterial pulse wave velocity (PWV) obtained with ultrasound (US) echo-tracking [67, 12, 8, 121, 96]. The propagation speed of the pulse wave (PW), a pressure wave generated by the heart in systole, can be related to arterial elasticity using the Moens-Korteweg equation [90], whereby stiffening of the arterial wall causes the PW to propagate faster [64]. In recent years, several research groups have refined the quantification of the PWV in the CA using high-frame-rate ultrasound imaging (HFRI) [81, 39, 148, 63, 22, 107, 59]. While the techniques developed in these studies adequately measure the PWV, they do not transcend the limitation of using a single parameter to describe the overall elastic state of a complete arterial segment, in this case the CA. Such a single parameter assumes a constant elastic state throughout the cardiac cycle and a constant elastic state across the whole region. These two assumptions ignore two important observations. Firstly, since the elastic state of the artery wall varies with blood pressure [140] and heart rate [95] the propagation of the arterial pulse wave is nonlinear [48, 23]. Secondly, applying an average PWV to an entire arterial segment does not allow for the assessment of local variations in the elastic properties within the wall [143].

Accurate assessment of arterial disease thus necessitates local evaluation of the tissue dynamics. The typical length scales and tissue velocities involved lead to requirements of high temporal and spatial resolution. In the case of the CA we want to image the interaction of the incoming phase any arterial pulse wave (PW) with the CA wall over some distance. Considering a PWV of several meters per second [89] and an interaction length in the order of millimeters we require a modality that can provide frame rates in the order of kilohertz. Giving that the tissue velocity during the PW interactions is only a few millimeters per second [107, 39] we require that the modality is capable of measuring sub-micron displacement. The only imaging tool available today that can fulfill both requirements is HFRI [102, 153, 161, 60, 37].

Here we present a high-definition motion-analysis technique based on plane-wave US imaging, which allows us to visualize arterial wall dynamics at short time and small spatial scales. We measure arterial wall motion on the basis of instantaneous phase echo differences between successive frames obtained with plane wave US imaging. We will show that the first order difference of the instantaneous phase of the beamformed signals provides an efficient way for measuring tissue motion locally. With this method we can now capture the full dynamics of pressure waves interacting with the CA wall. To test our method we scanned a group of healthy volunteers ($n=23$) and patients with CA arteriosclerosis ($n=2$) using HFRI at an average frame rate of 4.6 kHz. We will show that motion in a diseased artery wall with plaque is different from the motion observed in a healthy artery. We will also provide proof that this technique can be used to obtain the PWV. The validity of the proposed motion derivation is shown by means of reproducibility and consistency over the volunteers, over several cardiac cycles per volunteer and frame-to-frame motion.

3.2 Methods and materials

Using the US technique, the resolution of delay estimation is very good in the direction of the transmit beam (axial motion) and it is poor in the direction perpendicular to the beam (lateral motion). We therefore decided to restrict ourselves to axial motion, although it should be noted that there are techniques that can measure the complete tissue displacement vector with US imaging [79, 153, 37]. Fortunately the lateral motion of the CA wall in the longitudinal view is predominantly slow (induced by e.g. breathing) and easily separated from the rapidly changing axial motion, with the latter intrinsically related to arterial distension [51, 176].

Ultrasound imaging relies on the detection of reflected (and backscattered) ultrasonic pulses by tissue. When tissue moves, the next resulting reflection will show a delay with respect to the earlier echoes. Measuring this delay provides a direct tool for assessing tissue motion. Delay estimation in US is often done by cross-correlating the received echoes [105]. Instead of cross-correlating the echoes we can also use the phase of the signals to determine the delays. The phase can be unwrapped to obtain a measure of the exact location of the echoes along each image line, as proposed by [171]. However, unwrapping may introduce errors as a result of noise when the phase is close to $\pm\pi$. Instead of unwrapping the phase we can also apply a first-order time difference along the frame dimension. When the phase change between two successive frames is $\leq \pm\pi$ we obtain a direct measure of tissue motion which is directly related to the Doppler shift as was demonstrated by [58]. The $\leq \pm\pi$ coherency condition translates to a high-frame-rate requirement. In the case of HFRI of the

carotid artery, we not only easily satisfy the frame rate condition but also have a large number of phase samples available (in both space and time), which makes the phase-difference method once more worthy of consideration.

Phase-difference method

The phase-difference method involves five different steps.

1. We apply beamforming to the received radiofrequency (RF) signals after transmitting plane waves in the tissue. The beamforming is done in the Fourier domain, which can be very computationally effective [20, 91]. It requires a forward two-dimensional fast Fourier transform (FFT), an interpolation of the Fourier coefficients, and an inverse Fourier transform. By zeroing the conjugate or negative part of the spectrum prior to back transformation (equal to the Hilbert transform), one obtains the analytical beamformed signal $R(t)$, which can be separated into magnitude and phase image by means of the following equations:

$$E(t) = \sqrt{(R_r^2(t) + R_i^2(t))}, \quad (3.1)$$

$$\phi(t) = \arctan\left(\frac{R_i(t)}{R_r(t)}\right), \quad (3.2)$$

where $E(t)$ denotes the magnitude or envelope image and $\phi(t)$ the phase image. The signals $R_r(t)$ and $R_i(t)$ denote the real and imaginary parts of the analytical signal respectively. Every image $E(t)$ and $\phi(t)$ is stored in a separate 3D matrix. The envelope matrix is used to display conventional B-mode images and to mask the velocity images. The phase matrix is used for our motion analysis; see Fig. 3.1 for a schematic representation of the 3D phase matrix.

2. We obtain the first-order difference of the phase matrix along the frame dimension. This phase-time-difference directly yields the velocity of every pixel at each time point.
3. The $\pm 2\pi$ wrapping that remains after the first order difference is corrected by subtracting 2π from all values $> \pi$ and adding 2π to all values $< -\pi$.
4. For further regularization, all random-phase values resulting from echoes below a certain envelope threshold are masked out. Non-physiological velocity values, resulting from noise are set to zero.
5. Since we assume a certain continuity between neighboring samples, we applied a smoothing filter to reduce high-frequency velocity noise, using a separable 3D Gaussian convolution with a small kernel.

Temporal integration along the frames yields local tissue displacement, while local acceleration may be obtained by a second differentiation.

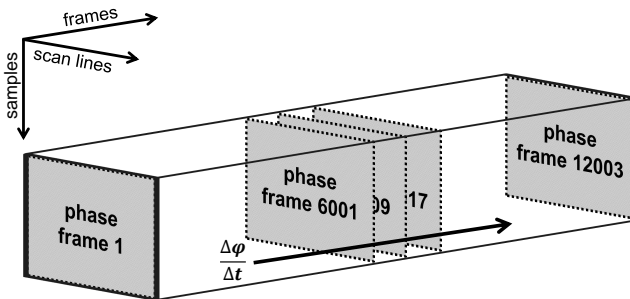


Figure 3.1: Schematic impression of the 3D phase-difference matrix

The code described above was implemented in Matlab 2012a (The Mathworks, Natick, MA) with Jacket v2.0 (AccelerEyes, Atlanta, GA) running on a 8-Core Intel Xeon 3.07 GHz workstation (Dell) with 48 Gb of memory and a GTX-680 4 Gb graphics card (NVIDIA, Santa Clara, CA). This allowed for a throughput of about 2 minutes starting from 16 Gb raw RF data to the complete set of B-mode and tissue motion images. This time period may be further shortened by choosing a different computing platform such as C/C++ or CUDA.

Carotid artery wall motion analysis

By measuring the distension of the CA in terms of displacement, velocity and acceleration, we gain insight in the elastic state of the artery as a whole and obtain values which can be used to calculate PWV locally, at every instant of the cardiac cycle. To this end, we defined separate regions-of-interest (ROI) for the anterior and posterior wall. The first frame of the scan was used to define the position of the ROIs. In Matlab, two lines were manually aligned with the walls (using the routine *imdistline*). A fixed number of samples above and below these lines were then selected to provide the complete ROI. It was assumed the ROI included the wall during the complete scan. The advantage of using these ROIs was that 3D phase processing could be further accelerated since only the samples within each ROI required processing. Based on the ROI selection we derived a centerline for the lumen, whereby the pressure wave is assumed to propagate from right to left and along the direction of the centerline. Figure 3.2 provides a schematic overview of the ROI and centerline selection.

All samples along each image line ($L_1 \cdots L_n$ in Fig. 3.2) belonging to the ROI and the 30 dB fidelity mask were adjusted for the centerline angle and averaged. For every image line ($L_1 \cdots L_n$) a distension profile was obtained by subtracting the averaged samples of ROI 2 from ROI 1. This resulted in a total of N distensibility curves (represented in terms of velocity), where N is the number of scan-lines present in both the anterior and posterior ROI.

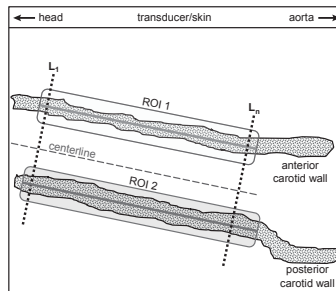


Figure 3.2: Delineation of the regions of interest for distension analysis.

Pulse wave detection

Features within the arterial distension waveform, such as the *ystolic foot* (SF) at the start of the distension waveform, and the *dicrotic notch* (DN) which signals closure of the aortic valve, display transient behavior along the arterial wall and can therefore be used to obtain the PWV [63, 66]. The PWV can be best estimated by comparing acceleration waveforms derived for

every line perpendicular to the blood flow direction [66]. In this study we derived the PWV at the SF and at the DN. The acceleration waveforms were obtained by first order difference of the computed distensibility curves and a 60 Hz low-pass 4th order Butterworth filter to suppress the high frequency noise [65]. For every scan-line two peaks, corresponding to the SF and DN, in the acceleration profiles were identified (using the routine *findpeaks*). The slope of a least square regression line through the peak locations provided the PWV (see Fig. 3.6 for an example). For every scan we averaged all SF PWV and DN PWV observations that gave a value within physiological bounds of 1 to 20 m/s.

In vivo study

In vivo validation of the proposed method was performed on a group of 23 healthy volunteers and on 2 patients with known atherosclerosis. For the healthy volunteer group we scanned both CAs while the person was in supine position. We recorded blood pressure, height, weight and age of the person. The two patients were scanned one day before undergoing endarterectomy surgery. All volunteers and patients gave written informed consent before HFRI scanning. The study was approved by the medical ethics committee of the Erasmus Medical Centre, Rotterdam - The Netherlands.

Ultrasound equipment and software settings

The ultrasonic plane waves were transmitted using a broadband (4-9 MHz, -6 dB bandwidth) linear array consisting of 128 elements (Vermon, Tours, France). All elements were excited simultaneously with a 2 cycle, 8 MHz Gaussian modulated sine pulse, with pressures well below the FDA limit. No surface heating of the array was observed. The array was interfaced with a 128 channel programmable ultrasound system using 12 bits, 80 MHz sampling (Lecoeur Electronique, Chuelles, France). Acquisition depth for each of the various volunteers and patients was varied between 20 and 32 mm. The scanning period was adjusted to the heart rate and set to obtain at least two complete heart cycles. Imaging frame rates from 4 up to 7 kHz were realized through a tradeoff between imaging depth, number of imaging frames and acquisition time. This system achieved a maximum frame rate of 35 kHz [92].

The plane wave preview mode provided a refresh rate of one frame per second, limited by the data transfer rate of the Lecoeur ultrasound system. As soon as a full longitudinal view of the CA was obtained the HFRI mode was activated and several thousand frames were acquired over a period of 2 to 3 seconds. After acquisition the data was transferred from the ultrasound system to a powerful processing computer. The RF was bandpass filtered using a 4th order Butterworth digital filter. Beamforming was done in the Fourier domain using complex linear interpolation and resampling to a 40 MHz grid [91]. The envelope fidelity mask threshold was set to -30 dB. The velocity cutoff for extreme non-physiological values was set to ± 12 mm/s. The size of the 3D Gaussian kernel was 5 *samples* \times 3 *scan lines* \times 7 *frames*. Within each ROI a total of 180 samples along each line was considered for distensibility processing.

3.3 Results

The phase-difference method allows extraction of single-pixel tissue motion. Figure 3.3 shows a three dimensional representation of CA wall velocity data acquired in this study. Three arbitrary US frames with overlaid velocity data show the in-plane motion. The first

frame shows the CA during positive distension, the second frame shows the CA during negative distension (reduced lumen diameter), and the third frame shows again a small distension of the CA. Two cross sections through the walls over time are displayed to highlight the amount and detail of the velocity information present. The total length of this data portion is just half a heart cycle. In Fig. 3.4 we show how each pixel contains unique

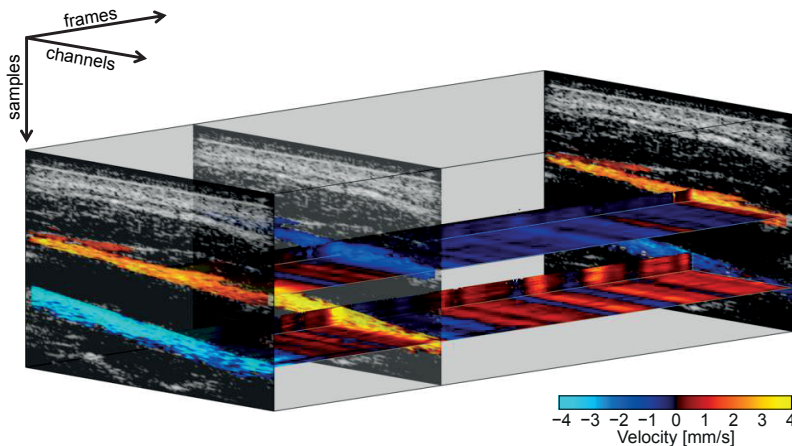


Figure 3.3: Three dimensional representation of carotid artery wall velocity for the period of half a heart cycle.

velocity information. The ultrasound (US) image in the left panel (a) shows a plane wave B-mode frame overlaid with tissue velocity data at one particular moment in time. The right panel (b) shows the tissue velocity curves over time at three different positions, indicated by the yellow numbers (1, 2, and 3) in (a) and are spaced approximately 15 mm apart. The three velocity curves in Fig. 3.4 (b) span a period of 60 ms with each dot representing a single frame. The peak velocities occur at different time points, a fact attributed to the position of these curves along the wall during a passing arterial pulse wave. The arterial pulse travels from right to left. The dashed vertical line in the right panel indicates the time point of the ultrasound frame. The velocity distension profile shown in the inset of Fig. 3.4 (b) shows the complete cycle and the box indicates the origin of the velocity curves shown below. Complementary to the previous figure we show in Fig. 3.5 pixel unique velocity information for a diseased artery wall during the same DN feature. The right panel shows tissue velocity curves at three different positions, where 1 and 2 are located along the thickened intima-media complex and 3 is located on a plaque.

Figure 3.6 shows the arterial distension velocity waveform obtained by subtracting the velocity of the anterior wall from that of the posterior wall for a typical healthy CA. The top graph (a) shows the distension (red), velocity (blue) and acceleration (black) of the CA. The image in (b) shows the distension velocity along the artery over time. The lower six subfigures (c) and (d) are magnified versions of the distension velocity (b) at the onset (SF; upper three panels) of the waveform and at the dirotic notch (DN; lower three panels). In the magnified image, the gray dots indicate the peak corresponding to the feature being tracked; the white lines are regression lines yielding the PWV in meters per second.

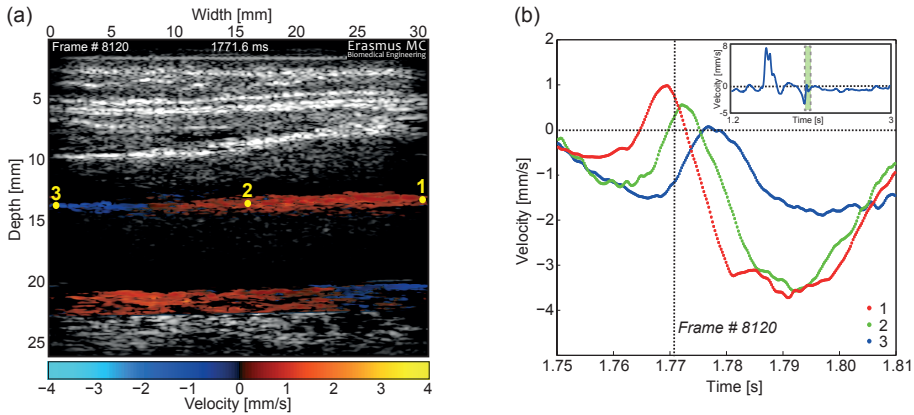


Figure 3.4: **Pixel unique tissue velocity profiles in healthy artery wall.** In the right panel (b) three different tissue velocity profiles are shown that belong to three individual pixels on the arterial wall of a healthy volunteer as depicted in the US frame in panel (a). The curves are part of the DN distension feature and show transient behavior from right to left (1 to 3) with respect to the peak velocity.

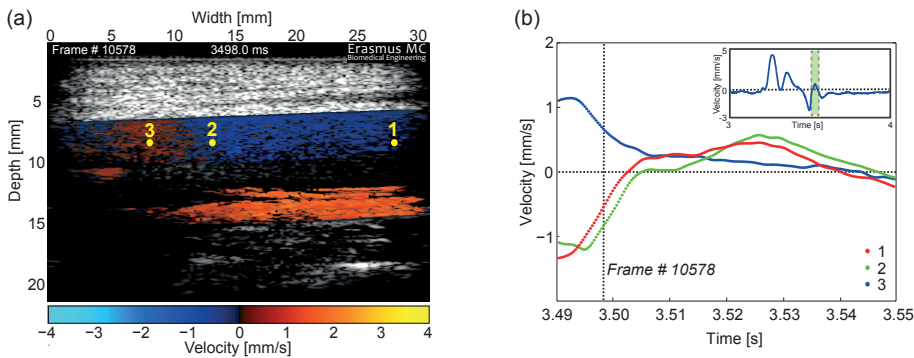


Figure 3.5: **Pixel unique tissue velocity profiles in a diseased artery wall.** The velocity curves 1, 2 and 3 shown in panel (b) originate from pixels of the anterior wall of a diseased artery shown in left panel (a). Pixel no.3 belongs to a plaque and shows a different course compared to the velocity curves 1 and 2.

HFRI combined with the phase-difference method as proposed here allows imaging of tissue motion in great detail. Figure 3.7 (b) shows six different tissue velocity frames from a 4.5 kHz HFRI scan obtained from a healthy volunteer. The graphs in Fig. 3.7 (a) shows the combined distension (red), velocity (blue) and acceleration (black) waveforms of the artery. The red dots on the magnified graph (inset) indicate the frames that are shown below (Fig. 3.7 (b)). The arbitrarily selected frames 7291, 7299, 7315, 7339, 7371, and 7441 are taken around the SF observed in the distension waveform. Other observations from the HFRI carotid study involving 23 healthy volunteers can be found in Table 3.1.

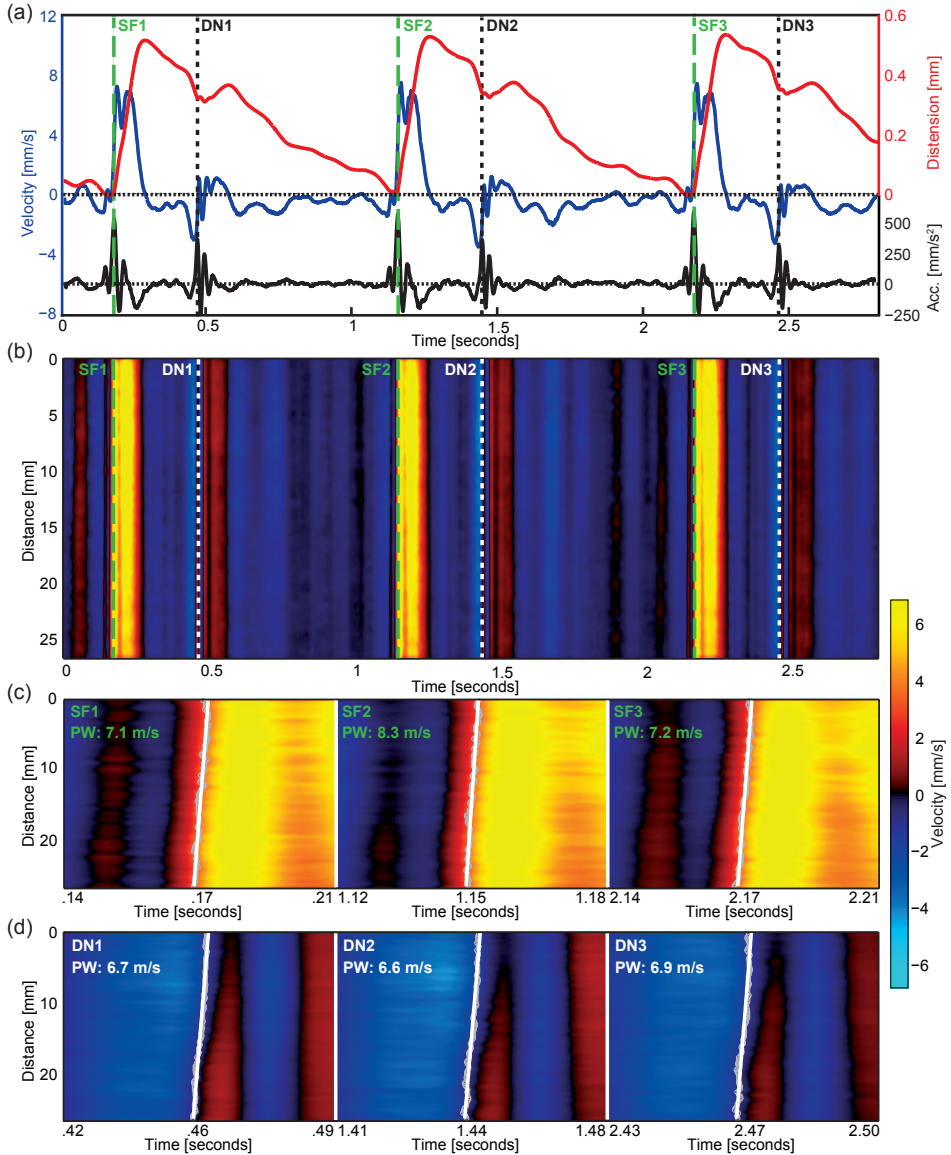


Figure 3.6: **Measuring pulse wave velocity.** The top figure (a) shows the distension, velocity and acceleration curves of a healthy carotid arterial wall. Subtracting the anterior wall velocities from the velocities of the posterior wall yields the distension velocity along the artery wall as depicted in (b). The PWV can be measured by estimating the slope of transient PW phenomena with respect to time and arterial wall distance. In subfigure (c) and (d) we show the transient PW at the SF and DN for three subsequent cardiac cycles, which are magnified subsets of (b).

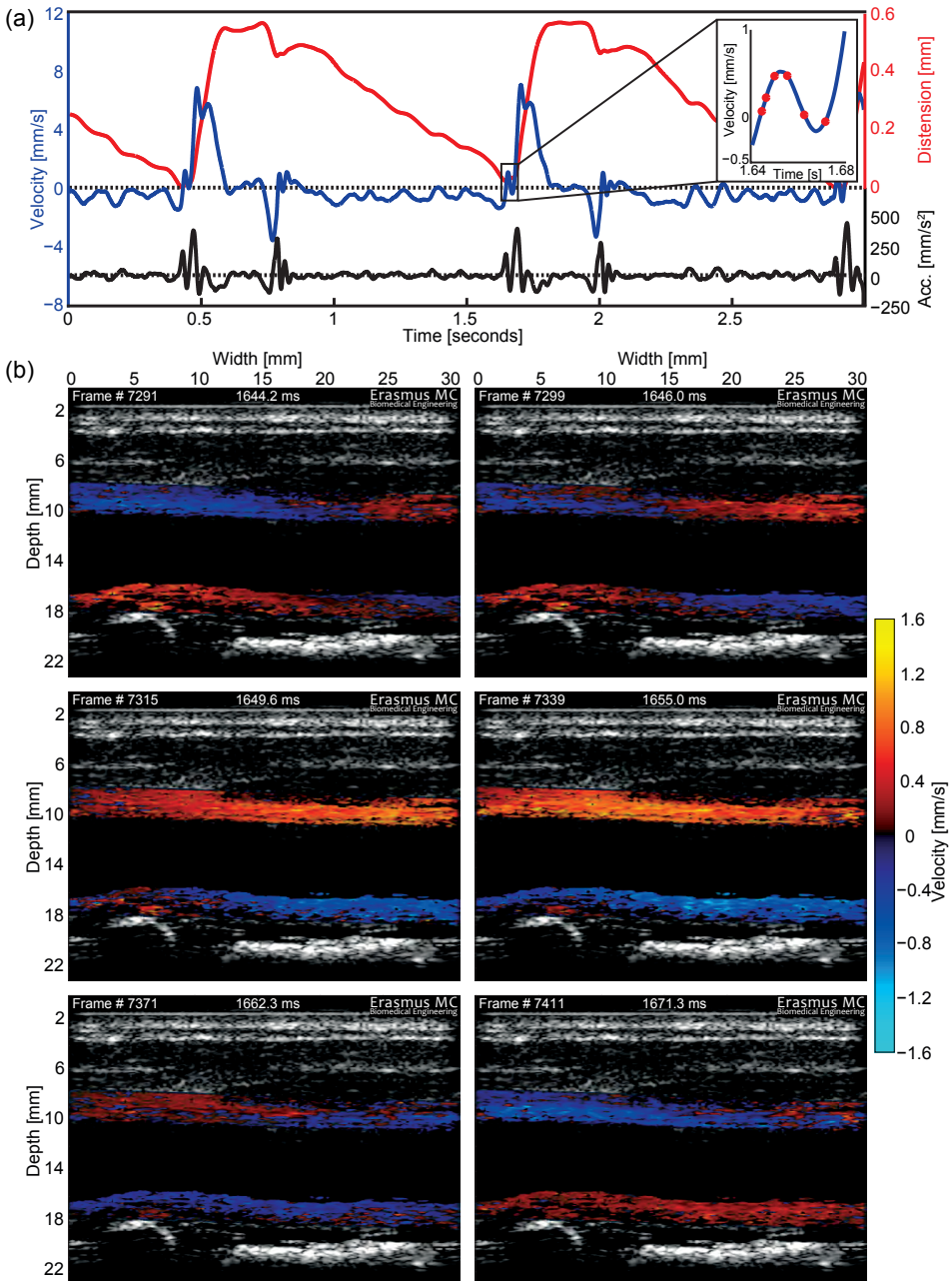


Figure 3.7: **Imaging transient phenomena along the arterial wall.** The interaction of the PW with the CA wall can be visualized with HFRI. This figure shows six individual tissue velocity frames from a healthy carotid artery during a 27 ms episode. The PW comes in from right to left. The top graph (a) shows the distension waveforms of the same artery.

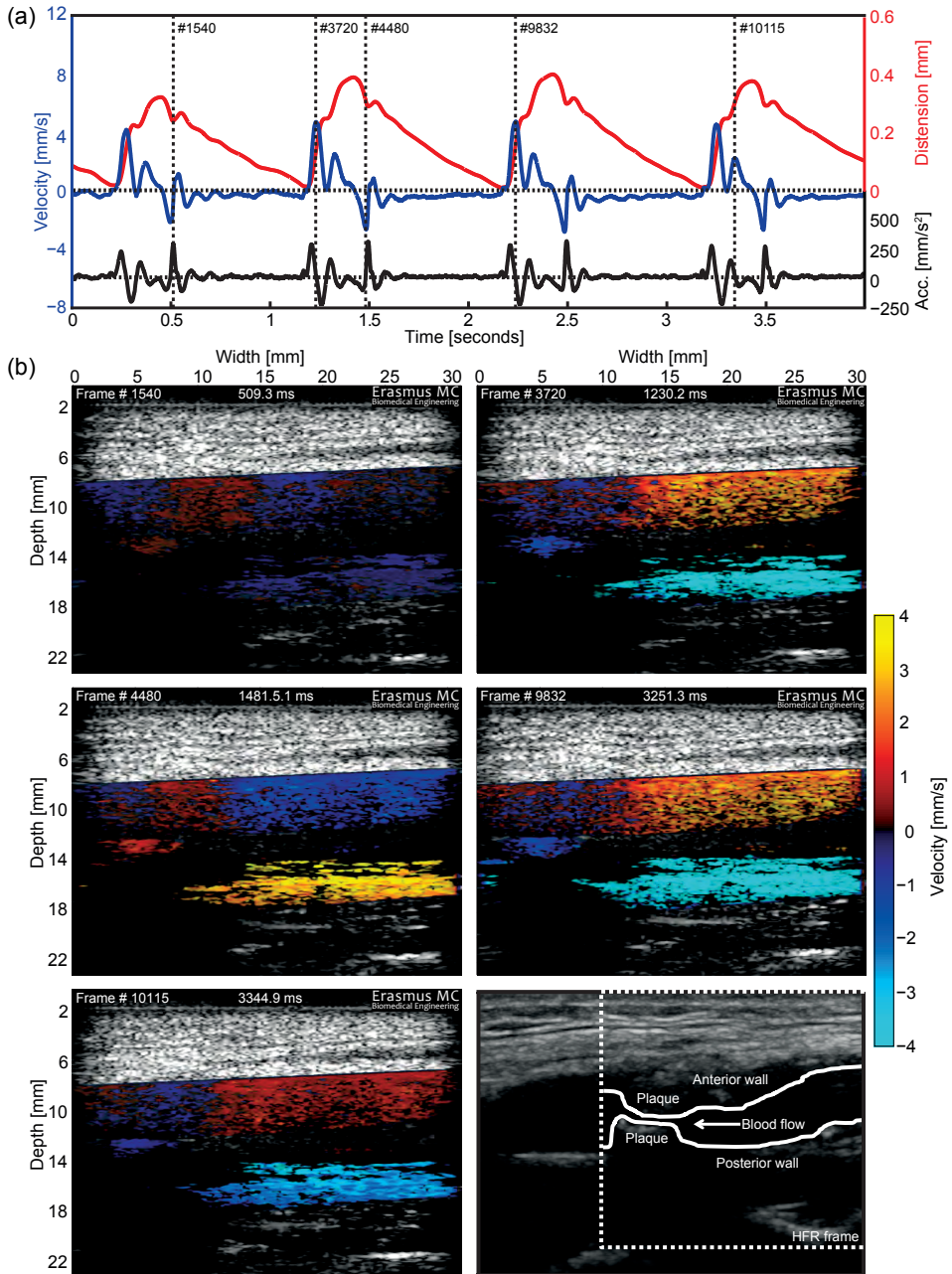


Figure 3.8: **HFRI of a diseased CA.** The top graph (a) shows the distension waveforms of the artery of a patient with a severe CA stenosis ($> 70\%$). Five arbitrarily selected tissue velocity frames are shown in (b). The plaque observed at the left side of these frames shows distinct tissue velocity with respect to the anterior and posterior wall. The bottom right US frame in (b) is obtained with a commercial US scanner. Overlaid contours indicate the lumen, plaque location and the field of view that correspond to the HFRI frames.

Figure 3.8 shows the result of a HFRI scan, combined with the phase-difference tissue motion method, from a patient with >70% diameter stenosis. Figure 3.8(b) shows five frames (1540, 3720, 4480, 9832 and 10115) with the instantaneous velocity overlaid on top of the classical B-mode image. The stenosis can be observed upstream in the images (left side). The bottom right image shows an US image of the artery with stenosis obtained using a commercial machine. The superimposed contours indicate the lumen, plaque location and the field of view that correspond to the HFRI frames. The locations of the frames with respect to the overall arterial wall velocity distension are indicated by the black dashed vertical lines in the top graph. Frame 1540 shows an overall arterial motion (blue) that differs from the motion of the plaque (red). Frames 3720 and 9832 show the artery at peak positive velocity. Although taken during two different heart cycles the similarity between the two frames is very apparent. Frame 4480 shows the artery at peak negative velocity. Frame 10115 shows the artery during the second episode of positive distension velocity - an observation made in this patient only. The combined distension (red), velocity (blue) and acceleration (black) waveforms of the artery as a whole are shown in the top graph.

Study parameter	Value	Values found in Literature
CA Diameter	6.1 ± 0.7 mm	5 – 7 mm [23, 129, 157]
Distension	5.9 ± 2.1 %	6 – 12 % [129, 157]
Velocities (min)	-2.8 ± 0.7 mm/s	-4 mm/s [59]
Velocities (max)	5.6 ± 1.6 mm/s	9 – 11 mm/s [129, 59]
Acceleration (min)	-132 ± 54 mm/s ²	-200 mm/s ² [59]
Acceleration (max)	261 ± 95 mm/s ²	500 mm/s ² [59]
PWV SF	6.8 ± 2.4 m/s	3 – 9 m/s [22, 39, 59, 63, 81, 107, 129]
PWV DN	7.7 ± 3.4 m/s	3 – 9 m/s [22, 63, 81, 148]
Heart rate	62.7 ± 8.4 bpm	
Blood Pressures (low)	74.5 ± 7.5 mmHg	
Blood Pressures (high)	124.7 ± 8.9 mmHg	
Age	33.9 ± 9.1 years	
BMI	24.4 ± 3.8	
Female	26%	

Table 3.1: Mean values \pm standard deviation, obtained with the high frame rate carotid study involving 23 healthy volunteers.

3.4 Discussion

In this paper we present an efficient, high-definition motion-analysis method for assessing tissue dynamics that we applied to measure motion in the wall of the CA. The phase-difference method produces a tissue velocity profile that is unique for each pixel. Integration and differentiation of the tissue velocity profiles with respect to time generates displacement and acceleration profiles. Although the analysis can only be applied if frame-to-frame motion is small ($\ll \pi$), when assessing wall motion in the CA this condition can easily be met by applying high-frame-rate plane-wave imaging.

When combined with the phase difference method, HFRI provides a wealth of infor-

mation on CA wall motion. Examples of the detailed tissue dynamics that this method can generate are shown in the 3D representation in Fig. 3.3, in the pulse wave velocity (PWV) close-ups in Fig. 3.6, in the velocity snapshots overlaid on the B-mode images in Figs. 3.7 and 3.8, and in particular in the raw individual pixel velocities shown in Figs. 3.4 and 3.5. We found the detailed motion profiles extracted from the phase difference method to be highly reproducible (see also Figs. 3.6, 3.7 and 3.8) and in good agreement with those found in the literature [69, 81, 157, 148, 63, 107]. [29] showed before that time delay estimation using the phase difference method produces similar results as the widely used cross-correlation method.

In order to quantify our image analysis method and to compare it with established methods from the literature, we chose to study the PW in particular. This is a well-studied phenomenon that is readily identifiable in our data. An elaborate example of PW propagation is shown in Fig. 3.6, panels (c) and (d). The PWV was calculated according to the times at which the acceleration peaks arrived along the CA wall. Note that the six PWV values measured during this scan are all different. The average PWV at the SF is 7.5 m/s, and the PWV at the DN is lower, namely, 6.7 m/s. The velocities measured in this individual are somewhat unexpected since they run counter to the expectation that the PWV at the DN is be higher than at the SF due to the increased stiffness of the arterial wall at higher systolic pressures [23]. The averaged data (Table 3.1) does confirm the expected relation between pressure and PWV. This variance in PWV suggests that a single PWV value is not sufficient to assess the elastic state of the artery [138]. As argued in the introduction, an accurate description of the nonlinear elasticity of the CA - that includes both the PW and other wave-wall interactions [59] - requires temporal and spatial resolution.

Our method provides both spatial and temporal resolution, as demonstrated in the visualization of the transient interaction of the incident PW with the arterial wall. In Fig. 3.7 (b) we show six discrete velocity frames around the onset of the distension waveform. As the PW enters from right to left, the artery expands slightly and contracts again in a period of 20 ms. At an acquisition frame rate of 4.5 kHz this event spans approximately 90 frames, while the interaction of the wall with the incoming phase of the PW covers about 20 frames. During this interaction, we measured tissue displacements of the order of $1 \mu\text{m}$. [148] have previously suggested that going beyond 1 kHz frame rate is not necessary for estimating PWV. While such a low frame rate might allow for a simple estimate of the cycle-averaged PWV in an entire segment, it is certainly not enough for a full assessment of artery wall dynamics, as we have demonstrated in this study.

The high-speed tissue motion observed in healthy subjects provides a baseline for comparison with diseased arteries. Figures 3.5 and 3.8 show the first result of this exploration. While the three velocity curves in Fig. 3.5 and the five frames (out of $>12,000$) in Fig. 3.8 can by no means cover all the features that were observed during this 4 second scan, they do demonstrate that the movement of a diseased artery is completely different to that of a healthy artery (compare Fig. 3.4 and 3.5). The five frames in Fig. 3.8 show how a heavily calcified plaque (calcification was confirmed by CT scan) moves together with the posterior wall and generates sharp velocity gradients with the anterior wall. It is likely that a strain analysis reveals a region of high strain around the plaque where it moves relative to the anterior wall. As well as this difference in artery movement, there is also a marked difference in the distension profiles between the healthy volunteers (Figs. 3.6 and 3.7) and the atherosclerotic

patient (Fig. 3.8). While the distension velocity profile of the two volunteers (blue curve) first shows a large positive velocity pulse followed by a negative one, that in the patient shows a characteristic pair of positive pulses, with a moment of zero velocity in between. This reproduces the "late systolic peak" commonly observed in aging and associated with increased wave reflection [85]. The velocity distension cycle concludes with a slow recovery during diastole. A patient study in a larger cohort is needed to further qualify and quantify to what extent the dynamics in diseased arteries differ from the dynamics observed in healthy arteries.

The analysis of the scans from the healthy volunteers ($n=46$, 23 volunteers, each with two CAs) showed that there are several factors during acquisition and data processing that affect the quality of our results. Firstly, for accurate PWV determination the artery must be precisely aligned with the transducer surface and the image should show the lumen at maximum diameter. This view corresponds with a cross-sectional view straight through the middle of the CA. A good predictor for a successful scan is when the intima-media complex is observed. Secondly, finding a good view was complicated by the low frame rate of the preview mode. Since not all scans in this study met these criteria, in some cases (4 out of 46) it was not possible to obtain a reliable PWV. Thirdly, we found PWV estimation to be strongly influenced by the characteristics of the low-pass filter applied to the scan-lines, a finding similar to that of [64, 65]. Finally, in many cases we observed that the posterior wall motion is stronger than that of the anterior wall, which is most likely caused by transducer pressure on the tissue overlying the CA.

By combining HFRI with the proposed phase difference method we were able to monitor all CA wall dynamics throughout the cardiac cycle. This method allowed us to observe various dynamic phenomena, including PW propagation, PW-wall interaction, layer compression, wave reflections and many more. We also showed that the tissue velocity fields in healthy and diseased arteries are different. These velocity fields can be used to calculate local strain and strain rate, factors which are directly related to local elasticity and which have demonstrated utility in several clinical applications. Despite their utility, in this paper we did not consider local strain and strain rate, since a better understanding of the lateral tissue motion component is required before the strain can be accurately computed.

3.5 Conclusion

The natural local deformations of the human carotid artery wall include displacements in sub-micrometer dimensions on a sub-millisecond time scale. In this paper we have demonstrated that these slight and rapid deformations can be captured by means of high-frame-rate ultrasound imaging together with a newly developed phase difference method. This method is extremely efficient in computational terms and offers high temporal and spatial resolution. By screening the carotid arteries of a group of healthy volunteers and two patients with atherosclerosis, we have demonstrated that high-frame-rate imaging can visualize tissue dynamics in unprecedented detail.

Vector Displacement Imaging

This chapter is submitted as:

Pieter Kruizinga, Frits Mastik, Johannes G. Bosch, Nico de Jong, Anton F.W. van der Steen and Gijs van Soest, Measuring submicron displacement vectors using High Frame Rate Ultrasound Imaging, *Ultrasonics, Ferroelectrics and Frequency Control, IEEE Transactions on*.

Abstract

Measuring the magnitude and direction of tissue displacement provides the basis for the assessment of tissue motion or tissue stiffness. Using conventional displacement tracking by ultrasound delay estimation, only one direction of tissue displacement can be estimated reliably. In this paper we describe a new technique for estimating the complete two-dimensional displacement vector using high frame rate ultrasound imaging. We compute the displacement vector using phase delays that can be measured between pairs of elements within an array. By combining multiple element-pair solutions we find a new robust estimate for the displacement vector. In this paper we provide experimental proof that this method permits measurement of the displacement vector for isolated scatterers and diffuse scatterers with high (submicron) precision, without the need for beam steering. We also show that we can measure the axial and lateral distension of a carotid artery in a transverse view.

4.1 Introduction

Ultrasound imaging allows us to visualize tissue motion inside the human body. The often complex dynamics of tissue motion provide insight in the underlying physiology of the processes we image. These dynamics may change when tissue becomes diseased [61, 136, 15]. For example, the motion dynamics and tissue stiffness of lesions within arteries that are affected by atherosclerosis, contain crucial information regarding the vulnerability of these lesions [18, 53, 28, 134, 146].

Unfortunately, the accuracy of lateral displacement estimation (displacement in the direction perpendicular to the beam) is generally poor compared to the axial (parallel to the beam) displacement estimation [35]. This discrepancy in the quality of displacement estimation also manifest in high frame rate ultrasound imaging (HFRI), where only a limited number of transmit beams are used to estimate displacements in an entire image. Displacement estimation with HFRI is further complicated by the scale of frame-to-frame displacements, which are generally small and therefore difficult to measure. Despite these difficulties, HFRI remains an attractive clinical tool in cases where tissue motion shows rapid dynamics, such as in the distension of the carotid artery [102, 153, 161, 60, 37, 93] or cardiac motion [82, 15].

Only few techniques have been proposed to measure tissue displacements (also named tissue Doppler) in two directions using HFRI. The majority aim to measure the blood velocity vector [169, 161, 37]. In these cases the frame-to-frame displacements are large and a reasonable estimate of the lateral displacement seems feasible. Measurement of the 2D displacement vector with HFRI of more solid tissue (for the purpose of elastography) has been accomplished by Tanter *et al.* [153]. They proposed to estimate the displacement vector by employing the classical vector Doppler method using triangulation. By subdividing the array in two (left and right) sub-arrays, combined with conventional beamforming and standard speckle tracking, the authors managed to estimate the displacement vector with reasonable accuracy (variance of $8 \mu\text{m}$ for a $50 \mu\text{m}$ lateral displacement without compounding).

In this paper we propose to estimate the displacement vector using array data prior to image reconstruction. Lateral motion of tissue produces a unique variation in pulse-echo signal delays across the elements of the array. The resultant delay in the image after conventional beamforming is mostly affected by axial motion, as the subtle delays due to lateral displacement are averaged out in summation. The general idea of this work is to compute the displacement vector using these small delays before they are lost in the beamforming. Similar approaches have been proposed before to measure blood velocity [169, 160, 55].

We capitalize on lateral phase gradients by formulating a geometrical two-element solution for computing the displacement vector, that we use as the basis for estimation of lateral motion. The pooled analysis of many of these solutions results in a method that is relatively robust to outliers and interference noise. The method is specifically designed for use with HFRI plane-wave data obtained with non-steered transmissions. It enables imaging of the tissue displacement vector in cases where the frame-to-frame displacement is very small ($< 1 \mu\text{m}$). These subtle displacements have clinical value in cases such as arterial distension

measurements [92] and shear wave elastography [153]. We provide experimental proof that we can measure the displacement vector with a precision below $1 \mu\text{m}$ for single and diffuse scatterers. We also show that our method can be used to extract the displacement vector in vivo in the case of a transverse view of a human carotid artery.

4.2 Methods and Materials

The general idea for measuring scatterer displacements using non-beamformed (array) data is rather straightforward. A moving scatterer will cause a delay in the echoes received by an array of elements. When the scatterer moves perpendicular to the array the delay will be approximately equal for all elements. When the scatterer moves parallel to the array, the delays will, depending on the direction of the displacement increase or decrease monotonically. This relation between displacement and delays is illustrated in Fig. 4.1.

In order to estimate the displacement vector we need to project these delays back to the original displacement. Wang *et al.* proposed to solve this back-projection by employing a least-square solution to this overdetermined system (since there are many delays yet only one vector to compute) [169]. The authors thereby assumed that the delays across an array can always be approximated with a straight line. The angle of this line with respect to the array surface then provides the lateral displacement estimate and the line-offset provides the axial component.

We propose to tackle the back-projection problem by computing many paired estimates of the new scatterer position. We will show that for the delays measured with two elements the solution of the new scatterer position is determined by a simple geometrical relation. This reconstruction can be done for all possible combinations of elements in an array. Choosing the best estimate from this set of solutions will provide the new displacement vector. For this paper we consider plane-wave transmissions and dynamic beamforming. Nevertheless the required location derivation can easily be expanded to other transmission and receive sequences.

Estimating the signal delay $\tau(x_n)$

For every displacement vector we need to estimate the signal delay $\tau(x_n)$ received by every element in the aperture. We estimate these delays using the technique described by Kasai *et al.* [83] by taking the difference of the instantaneous phase signal [93]. This difference can be efficiently computed by the angle from the product of a complex radio frequency (RF) sample and the complex conjugate of the delayed sample in a next frame [83].

An important advantage of HFRI is the consistency between neighboring frames. We therefore estimate this delay by estimating the derivative of the instantaneous phase, resulting in a smoother estimate of $\tau(x_n)$. For derivative estimation we use a modified Savitzky-Golay [133] differentiator (SGD) that works on the analytical RF signal.

The Savitzky-Golay filter fits a least-squares k -degree polynomial through data points. The polynomial coefficients can be pre-computed and used as filter coefficients for a digital convolution filter. Differentiation of the polynomial provides a good estimate for the

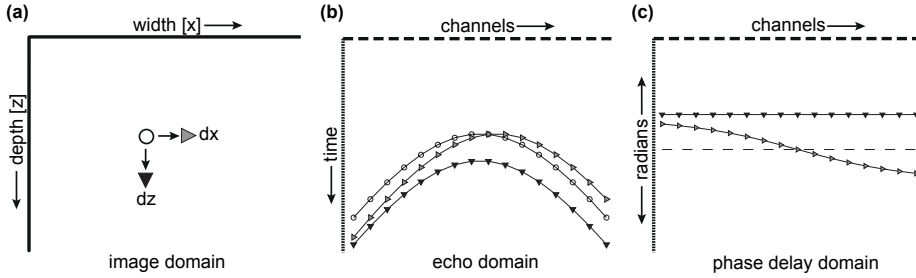


Figure 4.1: **Scatterer displacement causes unique delays across an array of elements** (a) A scatterer may move in the x -direction (gray) or in the z -direction (black). (b) This displacement will show in the recorded signals as a shifted hyperbola ($dx =$ gray, $dz =$ black). (c) The shifted hyperbolas will cause unique phase delays across elements in an array

derivative [108]. The coefficients for the k -degree SGD filter can also be pre-computed and used for convolution which makes it a very efficient process. The M filter coefficients a_m^k of the SGD are symmetric around the midpoint ($m = 0$; and M odd). The derivative of the instantaneous phase is computed by the weighted sum of the products of the data points from one side of the midpoint multiplied with the complex conjugate of opposite data points. This process can be formalized by:

$$\Delta\phi(s, f, x_n) = \sum_{m=1}^{(M-1)/2} \arctan\left(\frac{\text{Im}(R(s, f-m, x_n)R^*(s, f+m, x_n))}{\text{Re}(R(s, f-m, x_n)R^*(s, f+m, x_n))}\right) a_m^k, \quad (4.1)$$

where $a_m^k, m = 1 \cdots (M-1)/2$ are the first coefficients of the SGD filter of length M and degree k , $*$ is the complex conjugate and $\Delta\phi$ is the derivative of the instantaneous phase of sample s , frame f observed by element x_n . The signals $\text{Re}(R(s, x_n))$ and $\text{Im}(R(s, x_n))$ denote the real and imaginary parts of the analytic signal respectively. The delay $\tau(s, f, x_n)$ follows simply from:

$$\tau(s, x_n) = \frac{\Delta\phi(s, f, x_n)}{2\pi f_0}, \quad (4.2)$$

where f_0 is the central frequency of the transmitted pulse.

Derivation for the paired-element vector estimation

We now derive the relation between the delays measured by two elements and the displacement vector using plane-waves in transmission. We define the array for ultrasound signal generation and reception as containing N elements: $x_n, n = 1 \cdots N$. The array is positioned at zero depth ($z = 0$) and the center element is located at $x = 0$. The propagation distance for a plane wave transmitted by the array to a scatterer located at $P = (x, z)$ is then defined by:

$$TP = z \cos \theta + x \sin \theta, \quad (4.3)$$

where θ is the angle between the transmitted wavefront and the array surface.

The propagation distance for an echo originating from P to an element x_n is defined by:

$$RP_n = \sqrt{(x - x_n)^2 + z^2}. \quad (4.4)$$

When the scatterer moves to a new location $P' = (x', z')$, the propagation time of the echo to element n will be delayed by $\tau(x_n)$ which is equal to:

$$\tau(x_n) = (TP + RP_n - TP' - RP'_n)/c_0, \quad (4.5)$$

where c_0 is the speed of sound. We can rearrange eq. 4.5 such that:

$$TP + RP_n - \tau(x_n)c_0 = TP' + RP'_n. \quad (4.6)$$

We estimate $\tau(x_n)$ by application of eqs. 4.1 and 4.2 and can therefore substitute all known values in one element specific scalar d_n , such that:

$$d_n = TP' + RP'_n. \quad (4.7)$$

We now want to find the displacement vector $\vec{\Delta}$ that connects the known location of P with the unknown location P' . Using eq. 4.7 we can describe for one element a path of all possible P' 's. For two elements these paths intersect. The intersection of these paths is the location P' we want to find. Every pair of elements in the array produces one estimate for P' which we denote by p' . In the Appendix section we derive how this intersection (of two ellipsoids) can be calculated.

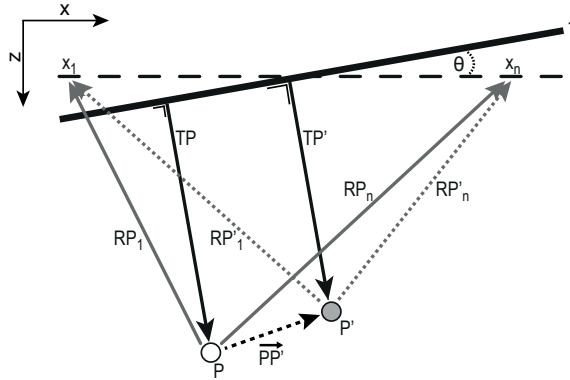


Figure 4.2: **Scatterer displacement can be estimated with only two elements.** When a scatterer located at P moves to position P' all elements in an array will receive a unique delay. For two elements (in this case element x_1 and x_n) the new position P' can be exactly determined using geometrical relations.

Finding the best estimate for P'

We approach the problem of finding P' by considering the ensemble of two-element estimates, using the delays available from the array that has N elements. The total possible number of unique paired solutions is $K = \frac{1}{2}N(N-1)$. Each solution produces one estimate $p'_w, w = 1 \cdots K$. In many cases not all elements will measure a meaningful delay (from eqs. 4.3

and 4.4) due to interference or other sources of noise. Rejecting element delays that are not reliable will improve the overall estimation but will also reduce the number of computations. The formulation of a robust rejection criterion is similar to the problem central to the minimum variance (MV) and coherence factor weighting (CF) beamforming techniques, in the sense that only those echoes that originated from the point of interest are to be considered [70, 170]. We perform this step by filtering the element delays (along the aperture) with a short averaging filter G and subtract this low-pass filtered version L' from the original delays L . The absolute difference $Q = |L - L'|$ provides a means to select meaningful delays by considering only the delays below the threshold Q_t . Interference signals are not smoothly varying across the array and thus will show up as strong deviations.

The remaining filtered delays are then used for the displacement estimation. To further improve the accuracy of the estimation and reduce computation time we only consider paired solutions that are computed with a minimum Δx_{min} and maximum Δx_{max} distance between two elements. With Δx_{max} we can control the effective aperture. Both rejection criteria reduces the number of unique paired solutions to K' . From these K' solutions we simply take the median value from the x and z component independently, such that:

$$P'(x) = \text{median}[p'_w(x) \ w = 1 \cdots K'] \quad (4.8)$$

$$P'(z) = \text{median}[p'_w(z) \ w = 1 \cdots K']. \quad (4.9)$$

The displacement vector $\vec{\Delta}$ is obtained by:

$$\vec{\Delta} = \begin{pmatrix} dx \\ dz \end{pmatrix} = \vec{P} - \vec{P}'. \quad (4.10)$$

Experimental Setup

We conducted two phantom experiments to quantify and validate our method. In the first experiment we imaged nine isolated scatterers during rotation. In the second experiment we imaged a piece of tissue mimicking material which was moved in the x and z direction. Finally, we applied our method to an in-vivo case where we imaged a pulsating carotid artery of a healthy volunteer in transverse view. In all cases we used plane-waves in transmission and frame rates ≥ 3 kHz. The ultrasonic plane-waves were transmitted using a broadband 128 element (4-9 MHz, -6 dB bandwidth, 245 μm pitch) linear array (Vermon, Tours, France) coupled to a 128 channel programmable ultrasound system using 12 bits, 80 MHz sampling (Lecoeur Electronique, Chuelles, France). In transmit we used a 2-cycle, 8 MHz sine pulse with a Gaussian envelope and Tukey aperture apodization.

An isolated scatterer phantom was made by mounting nine steel rods (0.5 mm in diameter) on a holder. We mounted the phantom in a setup with the rods pointing downward in a water tank and manually rotated the holder. For the second set of experiments we used a block of tissue mimicking phantom [156]. The phantom was moved along two dimensions using a stepper motor driven translation stage (BiSlide MN10-0100-M02-21, Velmex, Bloomfield NY). The linear array was placed outside the tank in horizontal position. Acoustic coupling was ensured by a window in the tank covered by a thin acoustic transparent polyethylene film.

Algorithm 1: Displacement Vector Imaging

Data: Non-beamformed complex RF plane-wave frames [Samples ($s = 1 \cdots S$) \times Elements ($x_n, n = 1 \cdots N$) \times Frames ($f = 1 \cdots F$)]

Result: dx -displacement image ($U \times V$) and
 dz -displacement image ($U \times V$)

for $i = 1:U$ do

 for $j = 1:V$ do

1. Get complex RF samples for frames: $[f - A, f + A]$ where $A = \text{int}((M - 1)/2)$ for all elements $x_1 \cdots x_N$ that satisfy the pulse-echo distance $T + R(n)$ for pixel (i, j) .
2. Estimate the element delays $L(x_n) = \tau(s, f, x_n)$ by complex conjugate SGD (eqs. 4.1 and 4.2).
3. Obtain a low-pass filtered version of the delays $L' = L * G$.
4. Discard all corrupted delays $|L(x_n) - L'(x_n)| > Q_t$.
5. Calculate all pair-wise $p'(x, z)$ estimates using $L'(x_n)$ and element distance $\Delta x_{\min} < |\Delta x| < \Delta x_{\max}$.
6. $dx(i, j) = P(x) - \text{median}[p'_{1 \cdots K'}(x)]$.
7. $dz(i, j) = P(z) - \text{median}[p'_{1 \cdots K'}(z)]$.

 end

end

Data Handling

After HFRI data acquisition, the raw RF signals were bandpass filtered using a 4th order Butterworth digital filter. For the tissue mimicking phantom and in-vivo experiment we discarded 11 out of 128 channels which were electronically corrupted. We corrected the acquisition jitter in our system by aligning all RF lines to a transmit signature that was present in all lines. Cross-correlation and sub-sample alignment (using phase shifts in the frequency domain) provided the means to obtain a slow-time stable dataset. The code described above and summarized in Table 1 was implemented in Matlab 2014b (The Mathworks, Natick, MA) with the Parallel Computing Toolbox running on a 8-Core Intel Xeon 3.07 GHz workstation (Dell) with 48 Gb of memory and a GTX-680 4 Gb graphics card (NVIDIA, Santa Clara, CA). Without extensive optimization we achieved a computing performance of 4.5 frames-per-second for the image in Fig. 4.5(a). For all experiments we used a second order SGD filter of length 7. The length of this filter should be chosen such that no phase wrapping occurs within the support of this filter. We used a 5 point average filter to obtain a low-pass versions of the element delays L' . The threshold Q_t for discarding unreliable delays was set to $1 \mu\text{m}$ for all experiments. For the rotating scatterer experiment we did not restrict the element separation distance. For the moving tissue mimicking phantom and the in-vivo experiment we considered only the estimates that were obtained with a minimum element distance Δx_{\min} of 16 elements and a maximum element distance Δx_{\max} of 64 elements. The vectors overlaid on the B-mode images were computed using an average estimate of neighboring pixels. The vectors were color coded according to their direction.

4.3 Results

Phantom imaging

The HFRI scan of nine isolated metal scatterers was used to validate and quantify our method. The scatters were rotated 145° in 1 second. For the analysis we used 2150 consecutive frames spanning a 90° rotation. Figure 4.3 shows the result of our vector estimation algorithm for a single pixel.

The pixel depicted in Fig. 4.3(a) is located in the center of the echo of a rod that was closest to the array in frame 900. The delays we measured for this pixel are shown in Fig. 4.3(b). From these delays we computed all possible displacement estimates. These estimates p'_w are shown in a scatter plot in Fig. 4.3(c). The black box in Fig. 4.3(c) indicates the displacement estimate based on the median value in both directions. The estimated distribution is much narrower in the axial direction, which is the direction of the transmit beam, than in the lateral direction.

Figure 4.4(a) shows one B-mode frame that was acquired during the scan of the rod phantom with the displacement vectors in color overlay. We used a mask defined by a -10 dB envelope threshold to define the regions of interest (ROI) for computation of the displacements. Each ROI resulted in one displacement vector, computed as the average (dx, dz) values in the mask neighborhood. In order to estimate the accuracy of the displacement estimates, we take a low-pass filtered version of the computed (dx, dz) time series, which do incorporate the (real) effects of rotational speed variations and rod misalignment. A histogram of the high-frequency components (containing the estimation error) of the (dx, dz) series computed for the rod closest to the transducer is shown in Fig. 4.4(b). Average projections of the dx - and dz -estimates analyzed in 2150 frames are shown in Fig. 4.4(c) and (d). The two components of the displacement vector are clearly separated. The center rod appears stationary as expected, and the four middle rods move at lower speed than the outer rods in Fig. 4.4(e), showing absolute displacement. Four rods each trace a 90° arc, covering 360° for all four rods in Fig. 4.4(f).

We evaluated our method for a diffusely scattering object by imaging the tissue-mimicking phantom, moving at a programmed constant velocity at a variable angle relative to the transducer. We imaged with a frame rate of 3 kHz during a period of 115 ms. Figure 4.5 shows some findings of this experiment. The phantom was circular in shape with a diameter of approximately 10 mm. For every recording we selected a square ROI of 5×5 mm (as depicted in Fig. 4.5(a)) from which we randomly selected 1000 samples to compute 1000 displacement vectors (100 vectors shown). Figure 4.5(b) shows a time trace of the estimated dx - and dz -displacements while the scattering phantom was moved away from the transducer with an average speed of 3 mm/s at an angle of 45° (a velocity of -2.12 mm/s, or a frame-to-frame displacement of $\pm 0.71 \mu\text{m}$ in both x and z directions at a frame rate of 3 kHz).

From the two graphs in Fig. 4.5(b) we can conclude that the dz -displacement estimation is closer to the true value than the dx -displacement estimation, with a much smaller variance in dz as indicated by the shaded band representing all 1000 estimates. Interestingly we observe a 150 Hz oscillation present in both graphs. This oscillation is due to the natural frequency of the stepper motor (this finding was confirmed by a separate electronic experiment) and was eliminated by subtracting the mean estimate from every frame before

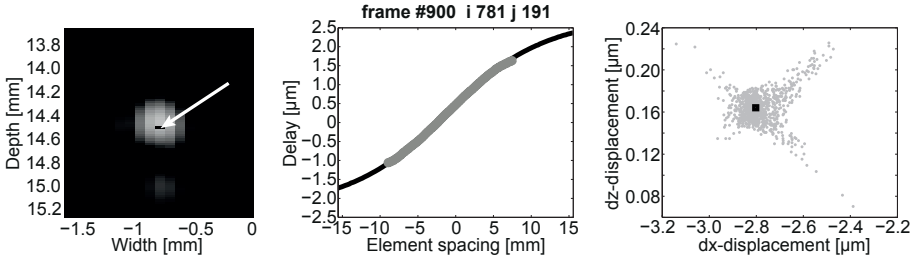


Figure 4.3: **Displacement estimation for a single pixel of a single scatterer** (a) Zoomed version of a B-mode ultrasound image of a metallic rod in water. The pixel indicated by the arrow is the pixel for which the displacement is estimated. (b) The delays corresponding to the pixel in (a) are shown in gray superimposed on the delays that correspond to calculated displacement. (c) All displacement estimates calculated with the paired-element method. The black box indicates the calculated displacement estimate for the pixel depicted in (a). Note that the axes in (c) are scaled differently.

further analyses. The accuracy and variability in the dx - and dz -estimates were extracted from the residuals. The results for $[dx, dz] = [1, 0] \mu\text{m}$, $[dx, dz] = [0, 1] \mu\text{m}$ and $[dx, dz] = [0.71, 0.71] \mu\text{m}$ displacements for 3 different experiments can be found in Fig. 4.5 (c), (d) and (e) respectively. In Fig. 4.5 (f) we show the findings for 6 different experiments for dx -displacement estimations: $[dx] = [-3, -2, -1, 1, 2, 3] \mu\text{m}$.

In vivo scanning

High frame rate displacement imaging can successfully be employed to image arterial distension of the carotid artery as we demonstrated in [93]. In earlier work we only considered axial motion in the longitudinal view of carotid arteries. As a part of the present study, we tested the displacement vector imaging method on a transverse view of a live carotid artery during a 0.9 second recording. Figure 4.6 highlights some findings of this scan. We show 4 individual B-mode frames (Fig. 4.6(a), (b), (c) and (d)) with the estimated displacement vectors in color overlay. We selected a circular ROI that contained only the artery wall and not the lumen.

Two single frames 175 and 2485 at maximum distension velocity are shown in Fig. 4.6(a) and (d) respectively. Although taken in two sequential heart cycles, the motion patterns in these two frames are very similar. Frame 780 in Fig. 4.6(b) is obtained at maximum negative distension. Here the vectors point to the center of the lumen. Frame 1970 in Fig. 4.6(c) captures sideways motion of the entire artery. The dashed yellow lines in Fig. 4.6 (c) indicate the ROI with 8 equal subdivisions that are used to calculate the distension curves displayed in Fig. 4.6(e), computed as the averaged dz difference between segments T and B , and the dx difference between L and R . The x -axis represents time and the y -axis represents displacement per frame in μm . The distension curves show the same features in both directions, although motion along x appears attenuated, as in Fig. 4.5. The lateral artery oscillatory motion is not a distension and hence does not show up.

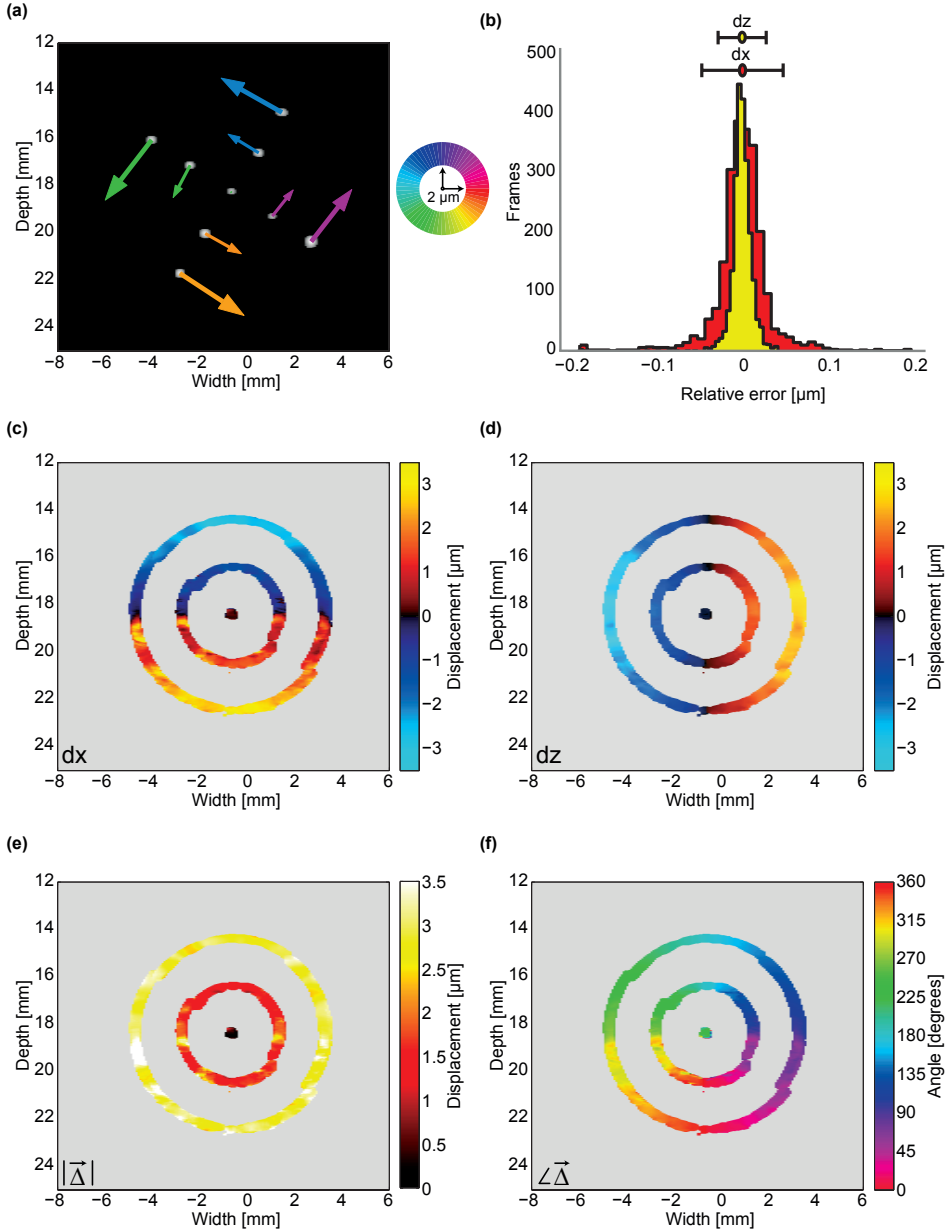


Figure 4.4: **Rotating scatterers imaged with high frame rate displacement vector imaging.** Nine metallic rods (0.5 mm diameter) were rotated over 90° while imaged with ultrasound at 3,000 frames per second. A B-mode frame with the estimated displacement vectors in color overlay is shown (a). The relative displacement error for the 90° trajectory of the top scatterer is shown in the bar plot in (b). The sub-figures (c) and (d) show an average projection of the estimated dx - and dz -displacement components. The average magnitude and angle projection are shown in (e) and (f).

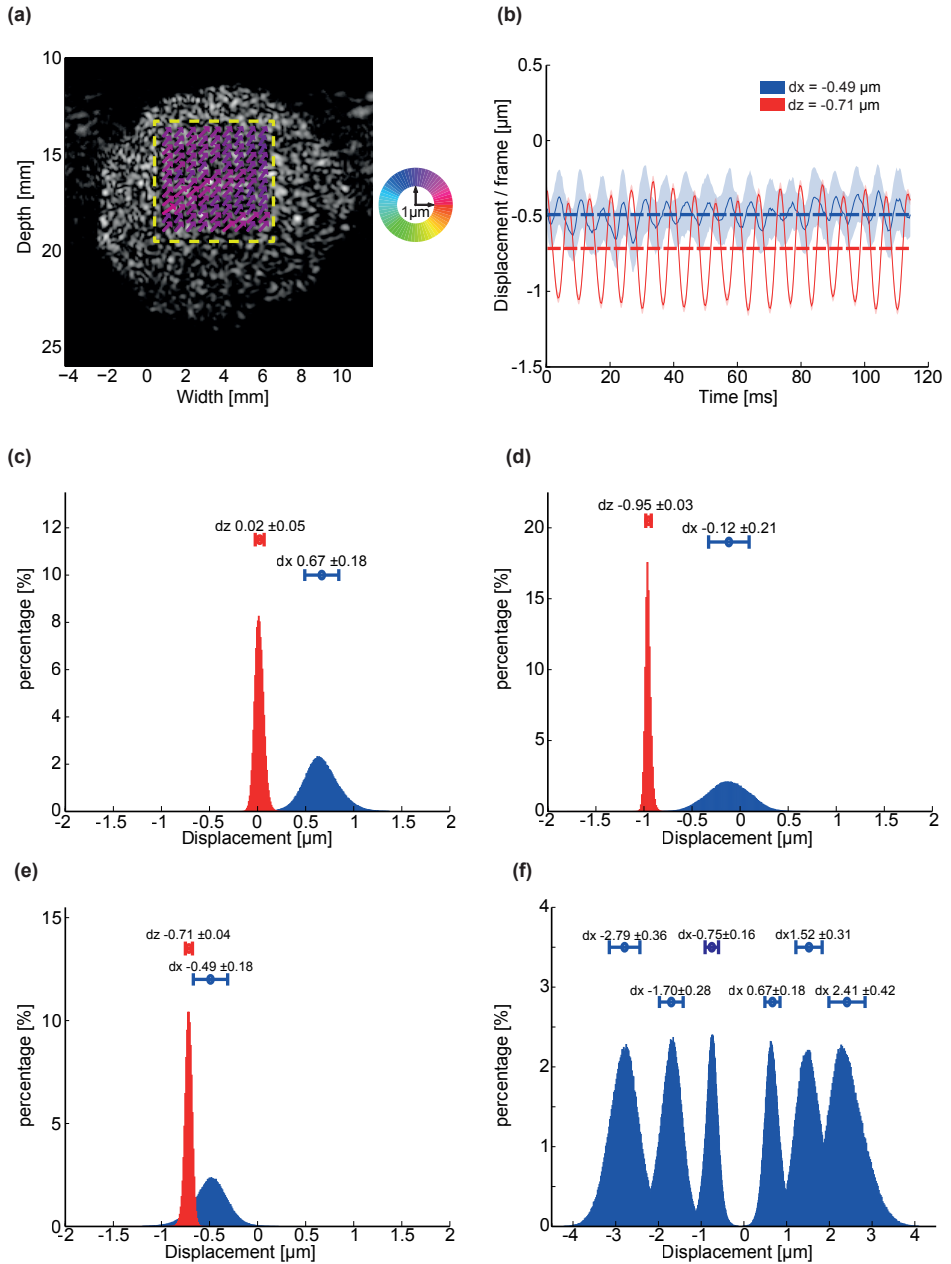


Figure 4.5: **Displacement vector imaging of diffuse scatterers.** A piece of tissue mimicking material was moved during high frame rate ultrasound imaging. (a) B-mode image of the scattering phantom, with a region of interest (dashed yellow lines) for which the displacement vectors (color overlay) are estimated. (b) Time trace of all pixel displacement estimates (shaded area) for a $-0.71 \mu\text{m}$ dx , $-0.71 \mu\text{m}$ dz (mean) oscillatory motion of diffuse scatterers. The cumulative histograms for all pixel displacement estimates are shown for three different scans: (c) $[dx, dz] = [1, 0] \mu\text{m}$, (d) $[dx, dz] = [0, 1] \mu\text{m}$ and (e) $[dx, dz] = [0.71, 0.71] \mu\text{m}$. (f) Histograms for 6 different dx -displacement estimations ($[dx] = [-3, -2, -1, 1, 2, 3] \mu\text{m}$).

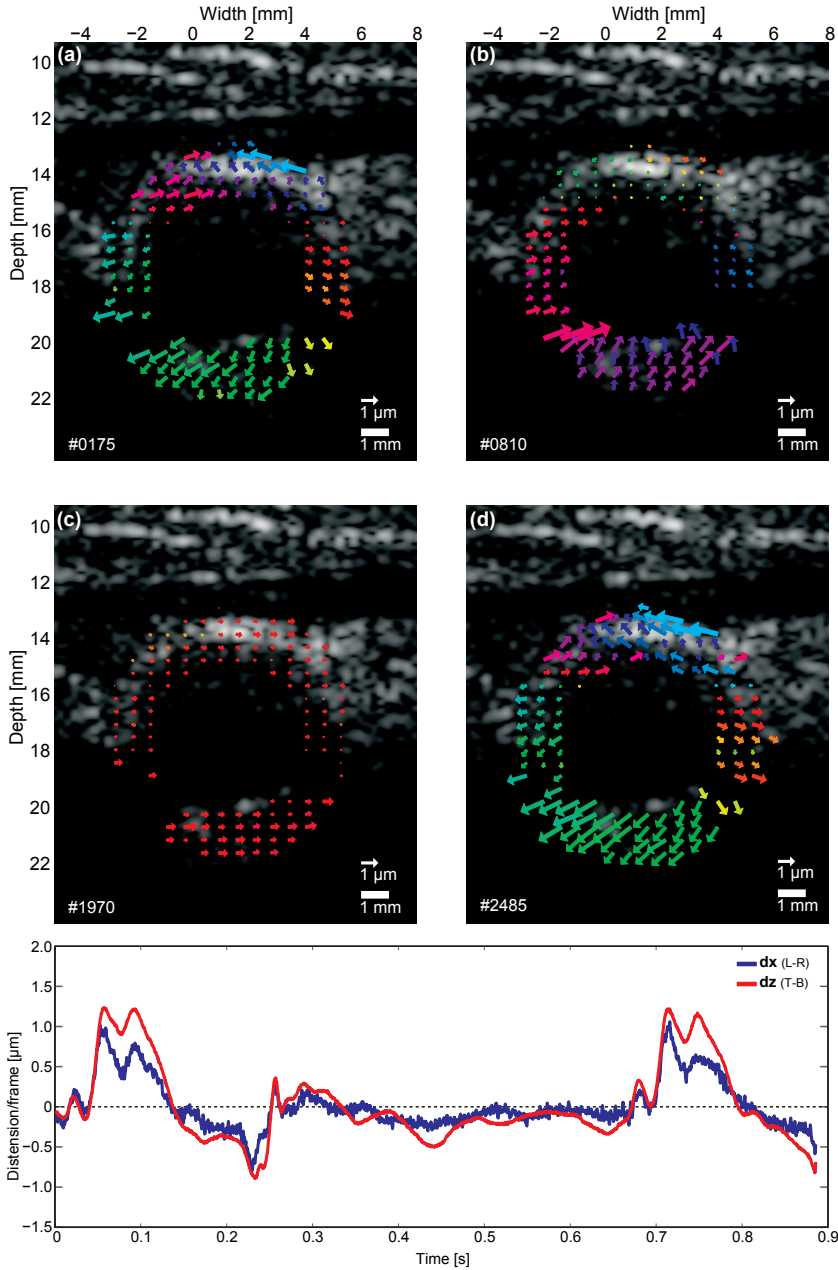


Figure 4.6: **High frame rate displacement vector imaging of a human carotid artery.** A carotid artery in transverse view was imaged with a frame rate of 3 kHz and analyzed with the new vector displacement estimation algorithm. (a)–(d) Individual B-mode frames with overlaid displacement vectors at (a) maximum distension velocity; (b) maximum negative distension; (c) lateral movement of the complete artery; and (d) maximum distension at the next heart cycle. Yellow dashed lines in (c) delineate the ROIs for distension analysis. (e) Distension curves in the z (red) and x (blue) directions.

4.4 Discussion

In this paper we present a new method to measure the displacement vector at high frame rates with micrometer precision. We derived a geometrical solution for a moving scatterer observed using only two plane-wave acquisitions. Using the time-delays measured across an array prior to beamforming provides the means to compute the two dimensional displacement vector with unprecedented precision. The method we propose is relatively robust for interference and noise that is present in experimental HFRI settings.

We validated our method with an experiment comprising rotating isolated scatterers. From the images in Figs. 4.1 and 4.2 it is clear that we can disentangle the dx - and dz -components of the displacement vector from the delays we measured across the array. For an isolated scatterer with no echo interference we can measure the displacement in both directions with a standard deviation close to ± 50 nm, as is highlighted in Fig. 4.2(b). We rotated the scatterer phantom by hand. An attempt to use an electric motor for rotation produced inconclusive results because the gearbox that was coupled to the motor produced very small ($< \mu\text{m}$) vibrations that were picked up by our method.

The delays across an array as a function of lateral scatterer movement are not linear across the array, as was assumed by Wang *et al.* [169], but can be complex in shape, especially for scatterers close to the transducer. We show in Fig. 4.1(b) and (c) that with our pair-wise solution we can approximate this complex relation between the measured delays across an array accurately. Echo interference affects the accuracy of the vector estimation, particularly in the presence of high amplitude echoes. Although the rejection low-pass filter proved to be useful, some of these artifacts still show up at 3 and 9 o'clock in the dx -projection in Fig. 4.2(c). The dx -displacement at these locations should be close to zero but they are not due to the interfering echoes.

We tested our method on diffuse scatterers by moving a piece of tissue mimicking phantom in the xz plane. A minute oscillatory motion pattern, originating in the translation stage motor, was picked up, visible in Fig. 4.3(b). It highlights how precise we can measure displacement with our method and HFRI. In Figs. 4.3(d) and (f) we observe a small negative bias in the dx -displacement estimation, which may be simply due to misalignment between the transducer surface and the x -translation axis. We found that lateral motion was underestimated by about 10-35%, similar to the results of Wang *et al.* [169]. A similar underestimation was observed in the in-vivo experiment. This underestimation was explained earlier by Flax and O'Donnell as an averaging or compression effect at the transducer side of multiple overlapping echoes that are laterally displaced [47]. The underestimation appears to be quantitatively reproducible and may be corrigible in post-processing.

With the results shown in Fig. 4.4 we show that the proposed vector estimation method can provide meaningful results in a complicated in-vivo setting. We demonstrate that with this method we can measure submicron lateral displacements in this highly clinically relevant imaging target [18, 117, 130, 146].

On close inspection of Fig. 4.4(a), (b) and (d), interference between echoes with different displacements (which can be out-of-plane) is seen to affect the estimated vectors in

the posterior and anterior wall, where the dx -displacement exhibits an unexpected pattern. Unfortunately we do not have any ground-truth displacement information. We also note that σ_{dx} was larger in the top and bottom of the artery wall than in the sides. Filtering the dx -estimate based on σ_{dx} may provide a pragmatic solution, which remains to be explored.

Using plane-waves to insonify the tissue causes the echoes to originate from the entire field of view. As a consequence, echoes from similar depth will interfere, complicating delay estimation. We proposed a simple filter criterion to discard these interference signals, but several other strategies have been explored. Compounding of signals or delay estimates from multiple steered transmissions may have particular merit, as echo interference will be built up differently for different angles, and the non-perpendicular wavefronts will improve the lateral motion estimate [153, 113]. Such techniques can be applied to our formalism as well. One clear advantage of HFRI is the consistency between sequential frames. This consistency can be exploited for using intelligent filter algorithms, such as the Savitzky-Golay differentiator we proposed, or to correct for jitter that is present in any ultrasound device. By subsample jitter correction we were able to boost the precision of the displacement estimation thereby pushing the bounds discussed by [165, 166].

HFRI generates large data volumes in a short time. Special attention should therefore be paid to data handling and computational complexity. Our method is computationally straightforward and easy to implement. It is also easy to parallelize, making it an ideal candidate for implementation using graphic processor units. The main cost comes from the large number of two-element estimates that can be calculated for every pixel. Smart selection of the aperture (Δx_{min} and Δx_{max}) and thresholding of unreliable delays are the probable next steps to reduce this computational burden. Application of this technique to future high-speed 3D imaging modalities will allow a full vector characterization of tissue motion and eliminate ambiguity due to out of plane motion.

4.5 Conclusion

Accurate assessment of rapid tissue motion requires HFRI (frame rates > 1 kHz) and two dimensional displacement estimation with sub-micrometer resolution. In this paper we presented a new method to compute the 2D displacement vector using high frame rate plane-wave ultrasound imaging. We propose to estimate the displacement vector using array data prior to beamforming. Pooling many unique displacement estimates obtained from paired elements in an array provides the means for a robust and precise vector estimation method. We showed experimentally that we can measure the displacement vector in-vivo below $1 \mu\text{m}$ resolution using plane-wave transmissions without the need for beam steering.

Appendix

Equation 4.7 describes a path for all possible P' locations. Here we derive how P' is exactly the intersection of two paths described by two elements. Rewriting (4.7) provides:

$$d_n - TP' = RP_1. \quad (4.11)$$

in Cartesian coordinates and squaring both sides gives:

$$(d_n - z \cos \theta - x \sin \theta)^2 = (x - x_n)^2 + z^2. \quad (4.12)$$

For simplicity we substitute the cosine and sine terms, where

$$a = -\cos\theta, \quad (4.13)$$

$$b = -\sin\theta. \quad (4.14)$$

Applying the substitutions (4.13) and (4.14) and expanding (4.12) for element x_1 and x_2 gives:

$$d_1^2 + z^2 a^2 + x^2 b^2 + 2d_1 z a + 2d_1 x b + 2z a x b = x^2 - 2x x_1 + x_1^2 + z^2 \quad (4.15)$$

and,

$$d_2^2 + z^2 a^2 + x^2 b^2 + 2d_2 z a + 2d_2 x b + 2z a x b = x^2 - 2x x_2 + x_2^2 + z^2. \quad (4.16)$$

Subtracting (4.16) from (4.15) gives:

$$d_1^2 - d_2^2 + 2z a d_1 - 2z a d_2 + 2b x d_1 - 2b x d_2 = x_1^2 - x_2^2 - 2x_1 x + 2x_2 x. \quad (4.17)$$

By introducing the constants A and B ,

$$A = \frac{a(d_1 - d_2)}{-b(d_1 - d_2) - x_1 + x_2}, \quad (4.18)$$

$$B = \frac{d_1^2 - d_2^2 - x_1^2 + x_2^2}{-2b(d_1 - d_2) - 2x_1 + 2x_2}, \quad (4.19)$$

we obtain a linear relation between x and z :

$$x = Az + B. \quad (4.20)$$

Combining (4.15) and (4.20) gives:

$$d_1^2 + z^2 a^2 + (Az + B)^2 b^2 + 2d_1 z a + 2d_1 (Az + B)b + 2z a (Az + B)b = (Az + B)^2 - 2(Az + B)x_1 + x_1^2 + z^2. \quad (4.21)$$

Rewriting (4.21) as a quadratic equation in z provides:

$$(a^2 + A^2 b^2 + 2abA - A^2 - 1)z^2 + (aABb^2 + 2d_1 a + 2d_1 Ab + 2abB - 2AB + 2Ax_1)z + (d_1^2 + B^2 b^2 + 2d_1 Bb - B^2 + 2Bx_1 - x_1^2) = 0. \quad (4.22)$$

Introducing the constants

$$C = a^2 + A^2 b^2 + 2abA - A^2 - 1, \quad (4.23)$$

$$D = aABb^2 + 2d_1 a + 2d_1 Ab + 2abB - 2AB + 2Ax_1, \quad (4.24)$$

$$E = d_1^2 + B^2 b^2 + 2d_1 Bb - B^2 + 2Bx_1 - x_1^2, \quad (4.25)$$

results in the following solution for z :

$$z = \frac{-D \pm \sqrt{D^2 - 4CE}}{2E}. \quad (4.26)$$

The conditions $z > 0$, $z < d_1$, $z < d_2$ and $d_1 \neq d_2$ to be used in (4.26) provide one unique solution for z . Using z in (4.20) then gives x .

Part II
**Photoacoustic imaging reveals
plaque composition**

Ultrasound-guided photoacoustic image reconstruction

This chapter has been published as:

Pieter Kruizinga, Frits Mastik, Dion Koeze, Nico de Jong, Anton F.W. van der Steen, and Gijs van Soest. Ultrasound-guided photoacoustic image reconstruction: image completion and boundary suppression, *Journal of Biomedical Optics* 18, no. 9 (2013).

Abstract

Photoacoustic (PA) image reconstruction of data acquired with conventional linear arrays suffers from incompleteness due to limited bandwidth and limited view. This problem is compounded by the dominance of boundary signals suppressing other weaker PA sources. In this study, we propose a method which uses a naturally co-registered ultrasound image to enhance the PA image reconstruction, with the dual aim to reconstruct the sources that suffer from incompleteness and reveal weak sources near a strong boundary. In this method an ultrasound image provides the input for a PA wave field simulation. The simulated PA field can be combined with the measured fields to complete the partial reconstruction or to suppress the dominant boundary signals. Experimental validation of the method was performed with two different phantoms and in-vivo data from the lower arm of a healthy volunteer.

5.1 Introduction

Translating non-invasive photoacoustic imaging (PA) to the clinic likely entails the use of a commercial ultrasound scanner, associated transducer array and a pulsed laser source [87, 11]. This instrument design, providing overlapping fields of view, allows for a natural integration of ultrasonic (US) and PA imaging in a combined modality [38]. In this setup ultrasound (US) can be used to reveal the morphology of the biological structures while PA provides functional information. This implementation of PA imaging, using conventional ultrasound imaging equipment, is constrained to band-limited signal detection in a limited view geometry. These two constraints have serious consequences for PA image reconstruction. Here we consider two consequences: the first is incomplete source reconstruction owing to the limited view geometry. The second consequence is the suppression of weak PA sources in the vicinity of dominant boundary signals as a result of coherent boundary source build-ups and band-limited detection.

The effect of limited view detection in photoacoustic imaging has been addressed before [175, 173, 123]. The acoustic pressure wave generated by a single PA point source is an outward propagating spherical surface [33, 25]. The source of this pressure wave can therefore be reconstructed by a limited number (> 1) of measurements at arbitrary points on this spherical surface. When many PA point sources are packed together the propagating field generated by this compound source is generally not spherically symmetric. Successful reconstruction of an extended source therefore depends critically on the range of wavenumbers (vectors accounting for frequency and direction of the acoustic waves) that can be detected. In the case of limited view geometry, only part of the wavenumbers required for full source reconstruction is detected, resulting in a partial source reconstruction. See Fig. 5.1 for a schematic representation of the limited view problem. Somewhat related to the limited view problem is the suppression of weak sources in the proximity of strong boundary signals. As discussed by Guo *et al.* when PA sources are lined up at a boundary the individual pressures, that arise after the laser pulse (t_0), will constructively (due to the similarity in phase and amplitude) build up to a dominant Huygens wavefront [56]. The sources behind this surface do not necessarily coherently add up to new emerging waves.

Interestingly, US imaging suffers less from the limited view problem and boundary buildup. In US the acoustic scatterers (sources) exhibit individual time characteristics in their wave emission due to relatively slow propagation of the imaging wave (unlike the optical wave used in PA). The boundary buildup effect and its dominance in PA image reconstruction is a well-known phenomenon. The dominant boundary effect can become increasingly dominant in the case of limited bandwidth detection. Bandwidth limitation is understood as an incomplete acquisition of the full frequency spectrum of the PA signal(s) by the transducer. The part of the PA signal that result from a boundary will most likely exhibit high acoustic pressures, due to the buildup effect, at relatively high frequencies which is due to the rapid transition in source strength at a boundary interface. In medical imaging, we generally use a transducer with limited bandwidth, sensitive in the few MHz range, acting as a filter receiving the signal. As a result, we are most sensitive to the high frequency part (> 5 MHz) of the PA signal and not so much to the low frequency part (< 5 MHz) of the waves. As an example, an artery with a diameter of 2 mm will, in a cross-sectional view under the condition of homogeneous illumination, emit most acoustic power around 800 kHz ($F = \frac{c_0}{\delta}$, where

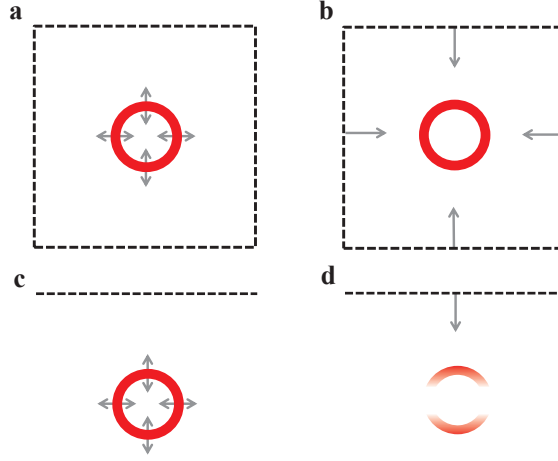


Figure 5.1: Schematic example of the limited view problem. In (a) a circular pressure distribution at t_0 with detectors on all four edges of the imaging plane, indicating the full view geometry. The source reconstruction of situation (a) can be found in (b). Subfigure (c) shows the limited view geometry of the same source as in (a) now using detector points along one edge of the imaging plane as is the case for limited view. The reconstruction using limited view geometry is shown in (d).

F denotes effective frequency, c_0 acoustic propagation speed and δ the effective optical penetration.) [120]. The PA signal that we will detect with a commercial 5 MHz transducer are however the high pressure - high frequency parts of the PA wave resulting from the 2 mm artery.

To formalize the imaging setting, let's consider the inverse problem for PA image reconstruction where we want to reconstruct s being the initial *source* pressure at t_0 , from our measured signals m . We describe propagation of s by the linear operator M (accounting for speed of propagation, dispersion etc.) and let R be the observation operator which converts the pressure field into a measurement. Putting these together we obtain (5.1) for our measured signals and (5.2) for the inverse reconstruction:

$$R(M(s)) = m, \quad (5.1)$$

$$s = M^{-1}(R^{-1}(m)); \quad (5.2)$$

where we assumed the operators R and M to be invertible.

A real-world measurement cannot acquire all data. For example, there is a finite number of transducers and bandwidth limitation in each experiment. We introduce the approximate observation operator \tilde{R} which takes these practical measurement issues into account. This implies that our actual measured signals m_{real} resulting from our source s obey:

$$m_{\text{real}} = \tilde{R}(M(s)). \quad (5.3)$$

Now, reconstruction of we want to reconstruct the original source requires the inverse of M and \tilde{R} . The inverse of M may be found by making assumptions on the properties of the

medium (speed of sound, attenuation, etc.), and by reversing time in the Green's function describing propagation of s . This propagation model will be called \widetilde{M} . Due to the limitations in bandwidth and wavenumber sampling, some frequencies and propagation vectors which are supported by $M(s)$ are not observed in the measurement. These components cannot be used for reconstruction, and as a result, the inverse of \widetilde{R} generally does not exist.

An estimate \hat{s} of the source s based on the measurement m_{real} can be written as, using eq.5.3:

$$\hat{s} = \widetilde{M}^{-1}(\widetilde{R}^{-1}(m_{\text{real}})), \quad (5.4)$$

$$\hat{s} = \widetilde{M}^{-1}(\widetilde{R}^{-1}(\widetilde{R}(M(s)))) \quad (5.5)$$

where we introduce \widetilde{R} as the modified observation operator, containing our knowledge about the measurement process. It accounts for practical limitations of the measurement, and is subject to a regularization which renders it invertible.

In a physical measurement we will never be able to fully reconstruct the original source, as \widetilde{R}^{-1} is not the inverse of \widetilde{R} , despite efforts to approximate \widetilde{R} ; bandwidth limitation is a property of a physical measurement. To improve the quality of \hat{s} we can modify one or more of the three approximated operators. Improving \widetilde{R} requires more measurements of the signal in the first place (larger bandwidth, adding sensor points, etc.). Greater accuracy of the estimated physical parameters of the propagation medium translates into an improved \widetilde{M} . Finally, more detailed information about the measurement itself (including instrument and object) may improve \widetilde{R} .

Previously, it has been shown that an acoustic velocity map derived from US measurements can be used to improve the reconstruction of PA images [80, 111]. These studies used the fact that both US and PA reconstruction rely on a shared physical parameter, the speed of sound propagation. The improved reconstruction results from a better estimation of the M operator. Another use of US information for improved PA source reconstruction is based on deformation tracking with US imaging to separate real PA sources from background clutter as was shown by Jaeger *et al.* [74, 73]. Here \widetilde{R}^{-1} is improved to generate a better estimate \hat{s} by discarding all the components of $\widetilde{M}^{-1}(\widetilde{R}^{-1}(\widetilde{m}_{\text{real}}))$ that do not move with the tissue structure as imaged by ultrasound. In this paper we will address the limited view and limited bandwidth reconstruction problems discussed above by augmenting \widetilde{R} with simulated detectors, taking advantage of morphological information derived from an US image to improve image reconstruction in cases where limited view geometry and band limitation applies.

The technique we introduce here was inspired by the observation that large-scale features in a PA image often resemble those seen by US. This suggests that differences in optical and acoustic properties of structures perceived in the images are tissue properties and thus often appear together. In other words, structures perceived with US will also contribute to the PA field, albeit by a different contrast mechanism. In our method we take an ultrasound image of the same scene as the source input for a PA wave field simulation. To improve source reconstruction hampered by limited view we use the predicted field to acquire the

missing wavenumbers and use them to improve PA image reconstruction. To suppress the dominant boundary signals we use the predicted field to mask-out the strong boundary signals perceived with the band and view limited transducer.

We explicitly write the limited-view measurement as:

$$m_l = \widetilde{R}_l(\widetilde{M}(s)), \quad (5.6)$$

where \widetilde{R}_l denotes our limited view signal acquisition. The reconstructed source based on the measured data m_l , \hat{s}_{exp} , is obtained by:

$$\hat{s}_{exp} = \widetilde{M}^{-1}(\widetilde{R}_l^{-1}(m_l)). \quad (5.7)$$

We propose to fill in the missing wavenumbers in m_l by estimating them based on the tissue morphology.

We construct a simulated source s_{sim} , based on the ultrasound image and \hat{s}_{exp} by an algorithm *A*:

$$s_{sim} = A(\hat{s}_{exp}; s_{US}), \quad (5.8)$$

where s_{US} is an estimate of s , assuming a constant or smoothly varying pressure distribution within its support; its borders are derived from a segmentation of the ultrasound image. With a PA field simulation we can now compute the simulated signals m_{sim} .

$$m_{sim} = \widetilde{R}_{sim}(\widetilde{M}(s_{sim})), \quad (5.9)$$

In the simulation we consider \widetilde{R}_{sim} as a closed surface signal acquisition as depicted in Figs. 5.1 (a) and (b). We choose $\widetilde{R}_{sim} = \widetilde{R}_{sim,l} + \widetilde{R}_{sim,c}$ as the augmented observation operator including the missing wavenumbers not captured in the actual experiment, though retaining the bandwidth limitation of \widetilde{R} . The set of complementary observations is represented by $\widetilde{R}_{sim,c}$, as observed by virtual detectors on the right, bottom and left border of the imaging region in Figs. 5.1 (a) and (b). Based on s_{sim} , we can obtain the limited view signals $m_{sim,l}$ and the complementary signals $m_{sim,c}$ by:

$$m_{sim,l} = \widetilde{R}_{(sim,l)}(\widetilde{M}(s_{sim})), \quad (5.10)$$

$$m_{sim,c} = \widetilde{R}_{(sim,c)}(\widetilde{M}(s_{sim})). \quad (5.11)$$

Minimization of $m_l - m_{sim,l}$ may serve to calibrate the procedure *A*. The above formulation of the PA measurement problem will form the basis for the image reconstruction algorithm we describe in this work.

In order to complement an image with missing wavenumbers due to limited view geometry, we add the simulated measurement to the actual experimental data to estimate \hat{s}_{cmp} :

$$\hat{s}_{cmp} = \widetilde{M}^{-1}(\widetilde{R}^{-1}(m_l + m_{sim,c})). \quad (5.12)$$

For the boundary suppression reconstruction \hat{s}_{bs} we subtract the boundary signals resulting from large-scale structures as seen in the ultrasound image:

$$\hat{s}_{bs} = \widetilde{M}^{-1}(\widetilde{R}^{-1}(m_l - m_{sim,l})). \quad (5.13)$$

As s_{sim} , resulting from the ultrasound segmentation, is homogeneous or smoothly varying, the simulated signals $m_{sim,l}$ will contain only signals that correspond (in case of band limitation) to the boundary of s_{US} . When $m_{sim,l}$ is subtracted from m_l we obtain a set of signals that includes all signals that do not belong to the boundary of s , thus resulting in a boundary suppressed image.

Figure 5.2 shows a schematic overview of the proposed method. We validated this method for both applications by simulations and experimentally using two different vessel mimicking phantoms and in-vivo data obtained from the lower arm of a healthy volunteer.

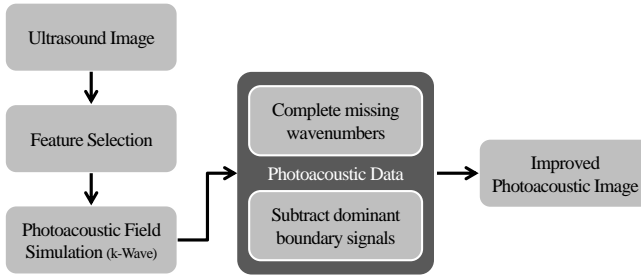


Figure 5.2: Schematic overview of the proposed ultrasound guided photoacoustic image reconstruction method.

5.2 Methods and Materials

Simulation

The technique of image completion and background subtraction can be tested by simulating PA and US imaging. All simulations in this paper were performed using the freely available acoustic field simulation Matlab toolbox *k-Wave* [3, 26, 158] in two spatial dimensions. We defined five unique PA sources:

1. a homogenous filled circle, mimicking a blood-filled vessel lumen;
2. a homogeneous ring, mimicking the source expected from a vessel wall;
3. a square with a source strength that is discontinuously decaying with depth;
4. a square with continuously decaying source strength and four point sources near the upper boundary;
5. a square with continuously decaying source strength.

All sources, except the last one, have an acoustic impedance difference with respect to the surrounding medium. Acoustic contrast was induced by a random scattering mask with an average impedance of 1.55 MRayl compared to 1.48 MRayl of water. Detectors were placed at all four edges of the simulation grid. Ultrasound plane wave imaging was simulated with the top row detector points and a short 2 cycle 8 MHz transmission pulse. Image reconstruction of the received ultrasound field was done through beamforming in the Fourier domain [91]. A

8 MHz, 60% band pass filter was applied to mimic band limitation normal for conventional PA acquisition. Photoacoustic image reconstruction was performed with use of the time reversal k-Wave implementation. More details on this simulation can be found in table 5.1.

Simulation Parameter	Simulation only	boundary suppression phantom experiment	all other experiments
Grid size	1024 × 1024	760 × 860	886 × 906
Voxel size [μm]	30	37	35
Maximum Frequency [MHz]	25	20	22
Speed of sound [m/s]	1480	1480	1510
Density [kg/m^3]	1000	1000	1000
Acoustic absorption [dB/(MHz/cm)]	0.5	0.5	0.5
Simulation duration [sec.]	137 (av.)	84	129

Table 5.1: Input parameters for PA field simulation with k-Wave.

Phantom

For experimental validation of the boundary suppression technique we prepared a polyvinyl alcohol (PVA) mimicking phantom with three inclusions in the wall. For the preparation of PVA we dissolved 20 g PVA grains in 200 ml water at 80 °C. To induce scattering of light and sound we added 1 g of SiC (800 mesh) and 1 g of SiO₂ (1 - 10 μm) to 200 ml 9 % PVA mixture. Two batches of 40 ml each with different optical absorption coefficient (μ_a) were prepared by adding Ecoline ®508 Prussian blue water based ink (Royal Talens, Apeldoorn) in two concentrations: 2 ml (μ_{a1}) in solution 1 and 0.5 ml (μ_{a2}) in solution 2. The vessel wall was made using solution 1, and the three inclusions were made using solution 2 [86]. The inner and outer diameters of the vessel were respectively 6 and 10 mm. The inclusions measured 1x1, 1x2 and 1x3 mm in cross section. The length of the phantom was 40 mm. The PVA solution was poured into a mold and put through six freeze-thaw cycles to create a stiff gel phantom.

For the image completion experiment we mimicked the photoacoustic source emerging from lumen of a carotid artery with a diameter of 6 mm. For this purpose we used a slightly modified version of the recipe of Teirlinck *et al.* [156]. In short 18 grams of Agar was dissolved in a mixture of 0.5 l demineralised water, 7 ml 50 wt. % aqueous solution Benzalkoniumchloride (ACROS Organics) and 8 ml Glycerol (VWR). To induce optical and acoustic scattering we added 2 g of TiO₂ (Sigma-Aldrich). For optical absorption we added 1 ml of Prussian blue ink. This mixture was put in a pressure chamber to clear any air trapped during the dissolving process. The mixture was then heated to 90 °C. After heating the dissolved agar mixture was poured into a cylindrical plastic tube with an inner diameter of 6 mm left to cool down and solidify.

Imaging

We used a wavelength tuneable laser (OPOTEK Vibrant B/355-II) generating 5 ns pulses at 10 Hz repetition rate at 650 nm for PA signal generation. The laser was coupled to a one-to-two fiber bundle linear array that could be interfaced with the linear array ultrasound transducer. For PA signal detection and US imaging we used a 128-element linear array (pitch: 245 μm , pulse-echo -6 dB bandwidth: 4-9 MHz (Vermon, Tours, France) connected to an open 128-channel US system (Lecoeur Electronique, Chuelles, France), capable of digitizing signals with 80 MHz sampling at 12 bits. For the US image formation we compounded multiple lines beamformed plane wave insonifications over a -7 to +7 degree steering angle. Beamforming of both the PA and US signals was done in the Fourier domain [158, 102, 91]. For the image completion phantom experiment we performed image reconstruction by time reversing the signals [3]. The in-vivo images were obtained from the lower arm of a healthy volunteer. The arm was kept stable in water with a temperature of 38 °C. In all experiments we averaged 60 frames to obtain a practical signal-to-noise ratio.

Ultrasound guided image reconstruction

The procedure for ultrasound-guided photoacoustic image reconstruction is outlined in Eqs. (5.1) – (5.13). Several choices need to be made in the practical implementation of $\tilde{\mathbf{M}}$, $\tilde{\mathbf{M}}^{-1}$, $\tilde{\mathbf{R}}$, $\tilde{\mathbf{R}}^{-1}$ and particularly \mathbf{A} . We present here a minimal scheme to demonstrate the functionality of the reconstruction methods, which can be adapted to specific applications.

All propagating ultrasound fields, whether for simulation or reconstruction, were implemented in the *k-Wave* toolbox [3] referenced above, used in Matlab (The Mathworks, Natick, MA) version R2012a. This models $\tilde{\mathbf{M}}$ (forward) and $\tilde{\mathbf{M}}^{-1}$ (backward propagation). Realistic assumptions on the speed of sound, acoustic absorption, dispersion etc. for this operator have to be made in order obtain an image. In our experiments we consider no specific prior knowledge of $\tilde{\mathbf{M}}$ so we assume the medium to be homogeneous and used the same parameters for all reconstructions, save for the speed of sound which is higher at elevated temperature.

The implementation of the observation operators such $\tilde{\mathbf{R}}_{sim}$ and $\tilde{\mathbf{R}}^{-1}$ in our case is straightforward. In all simulations we defined detector points at every grid cell along four sides of the simulation grid. All detectors record the acoustic wave field for every time step, stored as a pressure trace per detector. The actual measurement is emulated by $\tilde{\mathbf{R}}_{sim}$ integrating the simulated detector traces over the physical transducer element surfaces. Band limitation, characteristic for a conventional US transducer was introduced by filtering the received signals with a 4th order Butterworth band pass filter (4-10 MHz). In the simulation, pressure traces were filtered with the band pass filter supplied with the k-Wave toolbox. The operator $\tilde{\mathbf{R}}^{-1}$ upsamples the experimentally recorded radio frequency (RF) signal m_l or m_{sim} to the simulation grid. The same detector points were used to re-emit the acoustic field for time reversed image reconstruction.

The algorithm \mathbf{A} constructs a PA source s_{sim} based on information from US image and an initial PA source estimate \hat{s}_{exp} . It consists of two steps: segmentation of the relevant structures in the US image, and assignment of a source pressure to these structures in order

to match the experimentally observed PA signal. In the present study, aiming to demonstrate the principle of filling in missing wavenumbers in PA using information from the US image, we opt for manual segmentation (Matlab function *roi_poly.m*). A variety of methods have been proposed for automated US segmentation and border detection [118]. These tend to be application specific, however, and their performance depends strongly on US image quality. Development of such an automatic segmentation technique goes beyond the scope of this paper. After selection, the region of interest (ROI) was discretized on the simulation grid and a source pressure s_{sim} was assigned, scaled to the intensity observed in the original PA image reconstruction. A possible small mismatch between the selected ROI and the real PA source may be compensated through a channel dependent cross correlation between the experimental data and the simulated data. For in-vivo image completion we allowed a minor resize of the ROI based on height difference observed between the PA artery and the height of the ROI. For both the intensity scaling and the height correction we used two user defined control points for every artery in the PA reconstruction corresponding to the top and bottom boundary PA artery signal.

The processing of image completion and boundary suppression of the phantom data was done on the raw pre-beamformed experimental signals. In-vivo photoacoustic signal quality was too poor to allow direct summation and time reversal of m_{exp} and m_{sim} . For this reason, we performed the ultrasound-guided image reconstructions using beamformed signals.

For image completion we segmented features in the ultrasound image corresponding to a photoacoustic source of interest that could potentially be hampered by incomplete reconstruction due to limited view. Using s_{sim} as defined in (5.8), m_l as measured, and (5.11) and (5.12), we computed the ultrasound-guided PA reconstructions.

For boundary suppression we selected features in the US image corresponding to anatomical structures that may also be recognized in the PA image, attributed a source pressure, and performed PA wave field simulation. A mask was created based on the normalized envelope of the simulated signals, setting to zero all data points in m_l at which $m_{sim,l}$ exceeded a threshold value as a practical approximation to (5.13). This procedure reduces the sensitivity of \hat{s}_{bs} , which is much smaller than s in general, to alignment and calibration errors. The result was filtered and beamformed to obtain the boundary-free photoacoustic image.

5.3 Results

Simulation

Image completion and boundary suppression was studied using simulated targets. Figs. 5.3(a) and 5.3(b) show the simulated plane wave ultrasound scan and the PA pressure map at $t = 0$ respectively. Image reconstruction of the PA source using the top row detectors (the same as used for US imaging) can be found in Fig. 5.3(c). The reconstructed limited view image obtained from the US estimated PA source $s_{sim,l}$ is displayed in Fig. 5.3(d). The result obtained with the image completion method is shown in Fig. 5.3(e): the missing arc segments in the top two objects, and the missing sides of the square objects have been filled in with information derived from the US image. The absence of ultrasound contrast in the rightmost square means

that these missing wave vectors cannot be filled in. The effect of boundary suppression is shown in Fig. 5.3(f): the circular structures, lacking internal contrast, disappear. The leftmost square object only shows the internal boundary, which has PA but not US contrast. The small sources just below the top of the middle square are now clearly resolved. Again the square target on the right is unmodified.

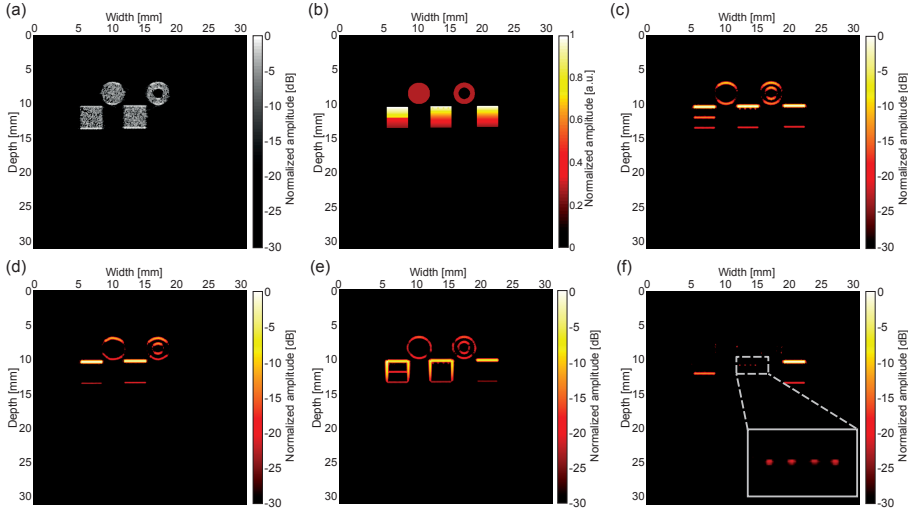


Figure 5.3: (a) Image obtained from the simulated sources after plane wave US imaging. (b) PA source pressures at zero time. (c) PA source reconstruction by time reversing the signals obtained by detector points at the top row of the simulation grid. (d) PA source reconstruction with data obtained from the estimated PA source. (e) Result obtained with the image completion method. (f) Result obtained with the boundary suppression method.

Image completion phantom experiment

Figure 5.4 presents the experimental realization of PA imaging completion on the cylindrical phantom. The US image of the phantom obtained with plane wave imaging in Fig. 5.4 (a) and the direct PA image \hat{s}_{exp} in Fig. 5.4 (b) are combined to generate the augmented PA source \hat{s}_{cmp} shown in Fig. 5.4 (e). The simulated limited view PA image $\tilde{M}(\tilde{R}^{-1}(m_{sim,l}))$ in Fig. 5.4 (c) and the full simulation reconstruction s_{sim} in Fig. 5.4 (d) are intermediate steps. Figure 5.4 (f) shows an overlay image of (a) and (e). The sides of the circular PA source are completed by the US-derived information.

Boundary suppression phantom experiment

The boundary suppression method was demonstrated experimentally on a vessel phantom with low-absorbing inclusions in the wall. A microscopy cross section of the object is shown in Fig. 5.5(a). Neither the US [Fig. 5.5(b)] nor the PA image [Fig. 5.5(c)] of the phantom has adequate contrast for the inclusions. The PA signal generated by the large-scale structure, which obscures the inclusions, can be simulated based on the US image, according to $\tilde{M}^{-1}(\tilde{R}^{-1}(m_{sim,l}))$. It is shown in Fig. 5.5(d). Subtracting this from the measured PA data \hat{s}_{exp}

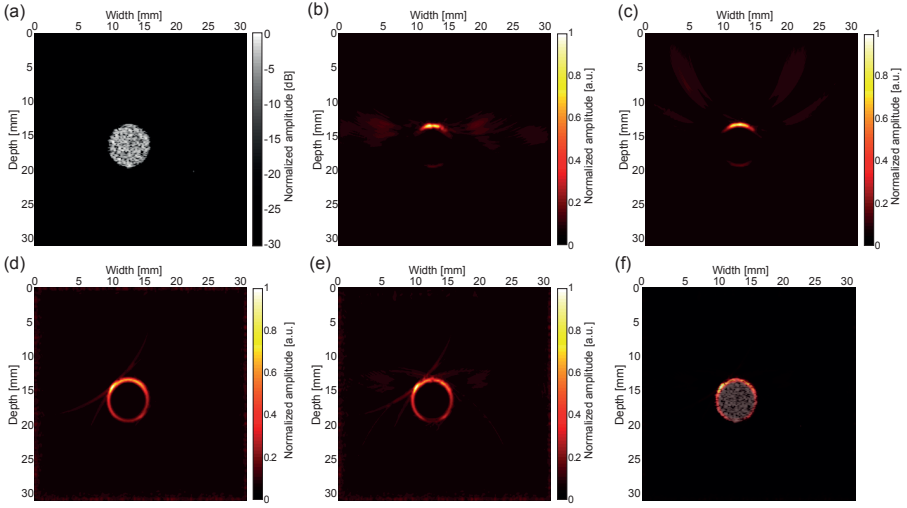


Figure 5.4: (a) US image and (b) PA image of the cylindrical phantom. (c) Reconstructed PA image from simulated signals obtained in limited view geometry. (d) Reconstructed PA image from simulated signals obtained in full view geometry. (e) Completed PA source based on data in (b) and (d). (f) Fusion of the ultrasound image shown in (a) and the completed PA image (e).

yields the PA signal of the inclusions $\hat{\delta}_{bs}$, shown in Fig. 5.5(e). This image clearly shows the heterogeneous structure of the phantom wall. Note that all images are normalized to their respective maxima.

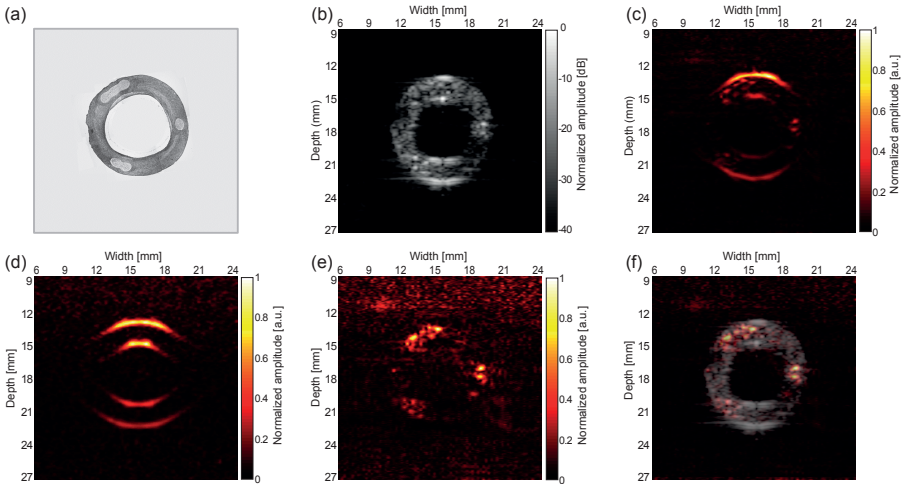


Figure 5.5: (a) Microscopy cross-sectional image of the vessel phantom. (b) US image and (c) PA image of the vessel phantom. (d) Simulated PA image. (e) Boundary-suppressed PA image. (f) Overlay of US and boundary-suppressed PA image.

In vivo imaging

To demonstrate that this method can also be applied in-vivo we conducted another experiment where we imaged a cross-section of the arm of a volunteer. In this experiment we identified the skin as a dominant boundary and selected a blood vessel for image completion. Figure 5.6 (a) shows the ultrasound image that was used to identify the water-skin boundary and the blood vessels perceived as darker regions, non-scattering regions in the image. The original photoacoustic image can be seen Fig. 5.6 (b). The skin and the partially imaged blood vessels are clearly identifiable. The image displayed in Fig. 5.6 (d) is the result after boundary suppression in the image domain. The final image (f) is the result of both boundary suppression and image completion in the case of two arteries.

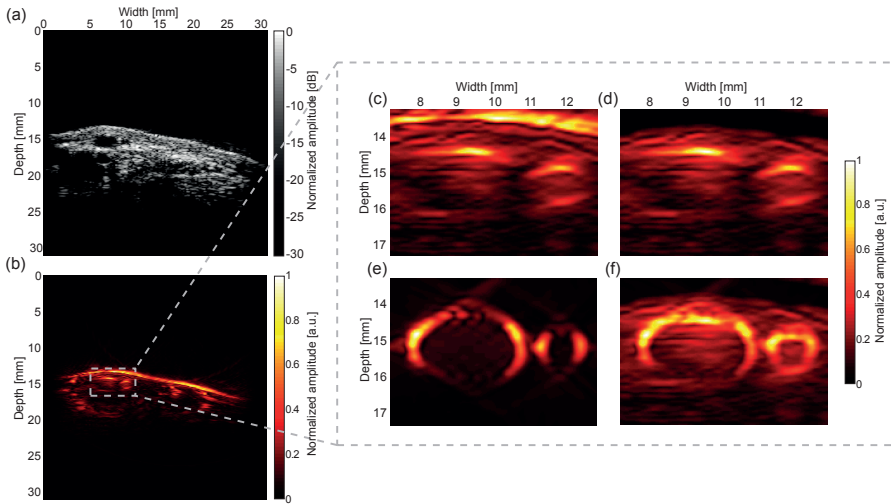


Figure 5.6: Ultrasound guided photoacoustic image reconstruction in vivo, imaging the arm of a volunteer. (a) Cross-sectional ultrasound image; (b) PA image of the same cross-section. (c) Zoomed region, containing two blood vessels. (d) PA image after boundary suppression of the signal from the skin. (e) Complementary simulated PA source $\tilde{M}^{-1}(\tilde{R}^{-1}(m_{sim,c}))$. (f) Image of the two blood vessels after boundary suppression and image completion.

5.4 Discussion

In this paper we propose ultrasound guided photoacoustic image reconstruction. This method uses information derived from US and PA images to simulate the full PA pressure field. We apply this concept to two techniques for US-augmented PA image reconstruction: image completion and boundary suppression. Both techniques, under certain conditions, are applicable to in-vivo PA imaging, as we demonstrated in this paper.

For the image completion technique we used the simulated signals to complete the experimental data with wavenumbers that were not captured due to limited view, i.e. those perpendicular to the transducer. Image completion may be especially useful for the interpretation of images containing blood vessels, as the relevant anatomy can be more readily

recognized. This also facilitates automated image analysis [122]. Blood vessels are of interest to PA imaging because they strongly absorb light, and may be used for monitoring of tissue oxygenation and local metabolism.

Our approach for image completion shows similarities to the technique called “iterative time reversal”, included in *k-Wave*. Both methods rely on the simulation of missing wavenumbers at virtual detectors. The main difference is that iterative time reversal requires the initial acquisition of the transverse k-vectors by a second, perpendicular, transducer to start the optimization. We propose, in contrast, to generate an estimate of $m_{sim,c}$ in a single step based on independent image data.

For the boundary suppression technique we used the simulated signals to suppress the experimental signals that emerged from strong boundary interfaces. Boundary suppression is applicable to a variety of cases where a small PA source is located close to a dominant interface, which would make the object of interest difficult to identify. One aspect of the technique that contributes to improved visualization is that the signal originating from the object of interest now constitutes the full dynamic range of the image. The US based simulation of the PA background selectively removes the signal originating from the large-scale structure. This cannot be achieved by the simple application of a threshold or mask. Exact colocation also enables the separation of multiple sources (clutter and object) within the signal envelope, relating to the limited bandwidth situation discussed in the introduction.

We demonstrate US augmented PA reconstruction in two dimensions in the present paper. The methods can easily be generalized to three spatial dimensions. The computational tools for this extension are available, and the assumptions we make hold equally valid.

Assumptions and limitations

The ultrasound guided image reconstruction method proposed in this paper relies strongly on the assumption that structures that appear in US also contribute to the PA field, as was illustrated by the simulation experiment (Fig. 5.3). This assumption is not necessarily valid in all imaging settings, and proper application of the method requires adequate judgment of the user. Still, in many cases a large-scale similarity between US and PA images of a scene is observed. This can be explained by the fact that image contrast in both modalities depends on tissue-specific properties. Optical absorption is the main contrast mechanism for PA imaging, but its variation may coincide with changes in echogenicity, density, and speed of sound which are responsible for US contrast. The complementarity between the modalities is reinforced by the fact that the image reconstruction is almost identical.

The quality of the US image has a strong impact on the accuracy of the PA source reconstruction. The simulated source s_{sim} depends on the quality of the input s_{US} . High quality US images of a known anatomy may allow automated segmentation by a customized computer-based algorithm A . Likewise, the initial estimate \hat{s}_{exp} requires accurate knowledge of the medium and imaging system parameters in order to compute \tilde{R}^{-1} , $\tilde{\tilde{R}}^{-1}$ and \tilde{M}^{-1} . The data presented in the present study could benefit from better signal-to-noise ratio and resolution in the US data, offered by high-end commercial imaging systems. More realistic modelling of transducer characteristics (directionality, impulse response) will improve $m_{sim,l}$.

Sophisticated signal and image processing techniques can be applied to ensure optimal registration between experimental and simulated data. We require a constant or smoothly varying pressure distribution within the support of s_{sim} on $t = 0$. Strong variations in the source pressure without acoustic contrast will generate a spurious PA signal that may or may not be of interest, but is not affected by our reconstruction. An example is the horizontal line in the bottom left object in Fig. 5.3.

5.5 Conclusions

We propose a new method for image completion and boundary suppression in PA imaging. We show that morphological information derived from an US image can be used to predict the PA wave field by simulation. We use these modelled signals to either complete the initial PA reconstruction or subtract features that are common in both images thereby enhancing the specific contrast offered by normal PA. This goes beyond simply overlaying the data obtained by US and PA separately. Rather, we use information from one modality (US) to simulate the expected signal in the other (PA). The simulated measurement in the second modality can be used to constrain or augment the – often ill-posed – problem of image reconstruction. We demonstrated the validity of the method with phantom and in-vivo measurements.

Acknowledgment

The authors would like to thank Victor Stoev for his assistance during the experimental work. Also thanks to Geert Springeling and Michiel Manten for constructing excellent setups and phantom moulds to perform the experiments mentioned in this paper.

Photoacoustic imaging of carotid artery atherosclerosis

This chapter has been published as:

Pieter Kruizinga, Antonius F.W. van der Steen, Nico de Jong, Geert Springeling, Jan Lukas Robertus, Aad van der Lugt and Gijs van Soest, Photoacoustic imaging of carotid artery atherosclerosis, *Journal of Biomedical Optics* 19 no. 11 (2014).

Abstract

We introduce a method for photoacoustic imaging of the carotid artery, tailored towards detection of lipid-rich atherosclerotic lesions. A human common carotid artery was obtained at autopsy, embedded in a neck mimicking phantom and imaged with a multimodality imaging system, using interstitial illumination. Light was delivered through a 1.25 mm diameter optical probe that can be placed in the pharynx, allowing the carotid artery to be illuminated from within the body. Ultrasound imaging and photoacoustic signal detection is achieved by an external 8 MHz linear array coupled to an ultrasound imaging system. Spectroscopic analysis of photoacoustic images obtained in the wavelength range 1130-1250 nm revealed plaque-specific lipid accumulation in the collagen structure of the artery wall. These spectroscopic findings were confirmed by histology.

6.1 Introduction

The carotid artery (CA) supplies the brain with oxygenated blood. A healthy CA consists of elastic collagen-rich material allowing it to sustain large and rapid variations in blood pressure. A CA affected by atherosclerosis shows degradation of the collagen structure, thickening of the intima and formation of complex plaques that contain regions with a lipid-rich necrotic core, calcifications and often intraplaque hemorrhage. Such “vulnerable” plaques may rupture and cause cerebral ischemic events [18].

The CA is easily accessible for non-invasive imaging, making it a viable target for screening of a population at risk for cardiovascular or cerebrovascular events [142]. Common imaging modalities used for CA screening are ultrasound (US), X-ray computed tomography (CT) and magnetic resonance imaging (MRI). These techniques provide mostly morphological information such as vessel wall thickening, accumulation of atherosclerosis and luminal narrowing. They lack however the capability of providing chemically specific information crucial in the clinical evaluation of the CA [117].

There is an unmet clinical need for a diagnostic technique that can improve risk stratification based on CA plaque characteristics. In the variable composition of atherosclerotic tissue, several plaque lipids have been identified that are associated with vulnerability [149]. Noninvasive imaging of CA plaque lipidomics may better assess the risk of future events, to inform medical or surgical therapeutic strategies.

Photoacoustic (PA) spectroscopy is a method to image tissue composition using the chemically specific optical absorption spectrum for contrast. For vulnerable plaque imaging, we aim to visualize plaque lipids. Distinct spectral features in the near-infrared absorption spectrum as sampled by intravascular PA (IVPA) can be exploited to identify lipids [167, 75] and to discriminate between fatty acids in normal tissue and cholesterol species found in plaques [78, 76]. In this paper we investigate the possibility of non-invasive PA imaging of CA plaques, with the aim to distinguish lipid-rich plaque from fibrous tissue and healthy vessel wall.

Conventional PA devices operate in reflection mode, delivering the light close to the US probe [34]. For imaging the CA in patients this approach meets with several problems. Seen from the skin, the CA is a fairly deep target, overlaid by skin, muscle, and often the jugular vein. Based on CT-angiography data (100 patients) we found an average distance of 2.9 cm from the skin to the common CA, and only 1.2 cm between the pharynx and the CA.

The skin is a strongly light attenuating tissue [10], particularly if there is a layer of subcutaneous fat which we expect to be common in the patient population to be investigated with this technique. There will be a strong PA signal generated near the surface of the transducer [87], and incomplete overlap between the non-collinear light and US receive beams, leading to signal generation outside the imaging plane [114].

We therefore propose to image the CA by means of interstitial illumination (from the pharynx) and external (neck side) US detection aiming to circumvent the aforementioned problems (Fig. 6.1).

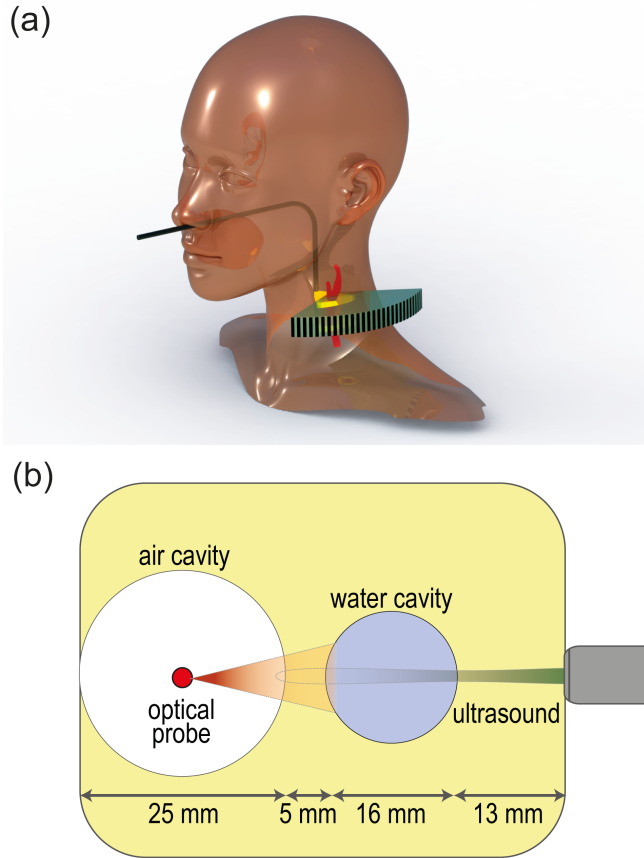


Figure 6.1: (a) An impression of the proposed method for photoacoustic imaging of the carotid artery employing internal illumination via the pharynx and external signal detection and ultrasound imaging using a concave array via the neck side. (b) Schematic overview of the neck phantom.

6.2 Methods and Materials

To test whether internal CA illumination can work for PA imaging we built a small optical probe comprising a multimode 400 μm low-OH fiber (Pioneer Optics) with a 34° angle (yielding maximum light reflection in a 0.22 NA fiber) polished tip covered by a quartz cap deflecting the beam. The fiber was embedded in a 1.25 mm rigid steel tube to allow easy handling for the beam characterization and controlled phantom experiments. A flexible probe for in vivo application was also built and tested, but not used in the experiments described in this paper.

The 400 μm optical fiber was coupled to a wavelength tunable pulsed laser (OPOTEK Vibrant B/355-II) using a tapered fiber (1 mm entrance, 360 μm exit diameter; Oxford Electronics, Four Marks, UK). The average pulse energy out of the optical probe at 1200 nm was 2.5 mJ in a spot of approximately 5 mm diameter, which results in a fluence well below the ANSI safety limit of 100 mJ/cm². For PA signal acquisition and US

imaging we used a conventional linear US array (ATL 12L5; center frequency 8 MHz, 256 elements) interfaced to a research US system (Verasonics V1; 256 transmit, 128 receive channels).

We mimicked the in-vivo imaging geometry with a phantom made with 18 g agar, 500 ml water and 1.5 g 5-75 μm SiO_2 particles (Sigma-Aldrich) [21]. One air-filled cavity (25 mm diameter) in the phantom mimicked the pharynx; another cavity is filled with water to hold the imaging target [see Figs. 6.1 (b)]. The rigid optical probe was mounted on an electronically controllable rotation motor (T-RS60A, Zaber Technologies) and a home-built manual linear stage for vertical positioning.

Ex-vivo validation of the proposed imaging method was performed with a post-mortem common carotid artery (CCA) obtained at autopsy from the Department of Pathology of the Erasmus Medical Center (MC), according to a protocol sanctioned by the Medical Ethics Committee of the Erasmus MC. The artery was fixated overnight using 4% buffered formaldehyde to prevent tissue degradation during imaging. The artery was put upright in the phantom cavity filled with a saline solution.

We performed PA spectroscopic imaging of the CCA using 25 wavelengths ranging from 1130-1250 nm with steps of 5 nm. The received PA signals were amplified, digitized (14-bits, 45 MHz sampling) and 64 times averaged prior to Fourier domain beamforming [158]. For every scan we obtained a 3D stack of 25 PA spectral images and one US image. US imaging was performed using a synthetic aperture transmit-receive sequences, dynamic beamforming in receive and image compounding. For both PA and US imaging the middle aperture consisting of 128 elements was used.

We designed a three-step tissue classification method using least-squares (LSQ) spectral unmixing [88]. We first normalize every pixel spectrum \mathbf{x}_i and every reference \mathbf{x}_R to its maximum value. In the second step, we unmix the spectrum at every PA image pixel with 4 lipid reference spectra [78], using the `lsqnonneg.m` Matlab routine. Finally, pixels with a high residual (using a heuristically determined threshold of $\|\mathbf{x} - \mathbf{x}_R\| > 2$) were further decomposed with two known tissue spectra (water and collagen [7]). The reference spectrum with the largest weight was used to label the main tissue component detected in the image. We omit a compensation for possible coloring of the local fluence as a result of wavelength-dependent light attenuation. Water and collagen, the dominant absorbers in the mucous and muscle tissue occurring in the path from the pharynx to the CA, have relatively weak and slowly varying absorption spectra in the wavelength range 1130-1250 nm, compared to strong and distinct absorption of the lipids we seek to detect. This is sufficient for classification of the most abundant tissue component, unlike quantitative spectroscopy which retrieves absolute concentrations of chromophores [24].

6.3 Results

In Fig. 6.2 we show three spectral (1130, 1200 and 1250 nm) PA images superimposed on an US image obtained from the diseased CCA inside the neck phantom. The relatively high water absorption around 1200 nm causes PA signal generation at the pharynx-neck interface (left side). PA signal generation inside the artery wall is observed in all three images with a clear signal increase inside the artery wall at 1200 nm [Fig. 6.2(c)]. No PA signal was detected for

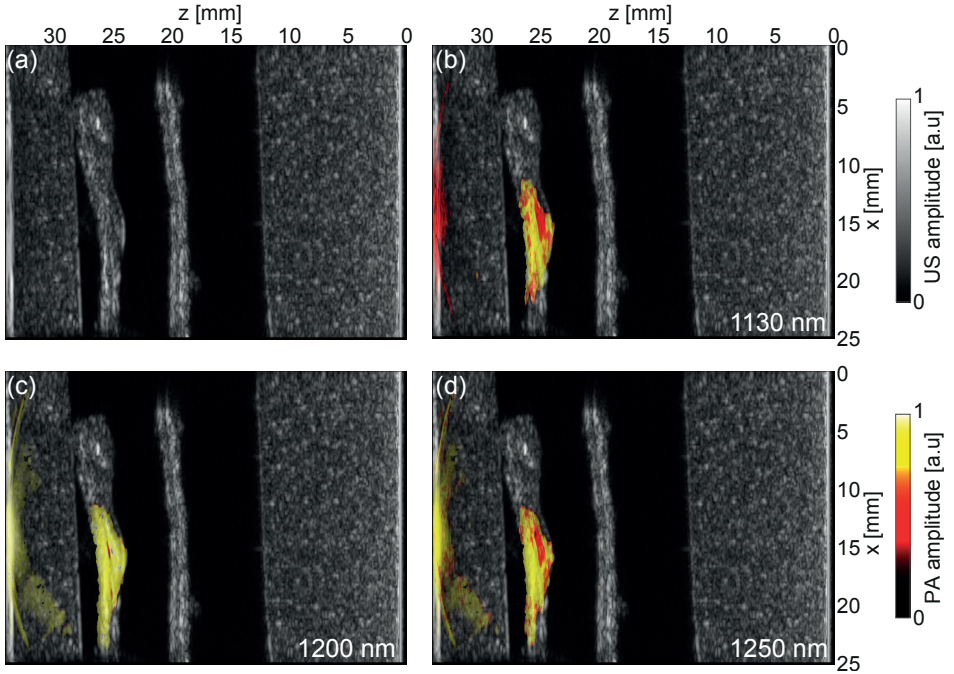


Figure 6.2: (a) Ultrasound (US) image of a diseased human carotid artery inside a neck phantom. (b-d) Superimposed photoacoustic (PA) images obtained at 1130, 1200 and 1250 nm respectively. The US transducer was positioned on the right and the light was administered from the probe positioned in the cavity mimicking the pharynx on the left. The US image shows mild thickening of the intima. In the PA images we observe signals from the artery wall with localized signal increase at 1200 nm (c) indicative for the presence of lipids.

the far wall of the CCA. Figure 6.3 shows the same US image as shown in Fig. 6.3(a-d) with now superimposed the result of the PA spectral unmixing for the tissue types: water, collagen, fatty acids and cholesterol species dominant in diseased plaque tissue. The artery generates PA signals that are spectrally distinguishable by their collagen and lipid signature. Inside the artery wall we observe a lipid accumulation inside the collagen structure. Histology using Oil Red O (ORO) lipid staining [right images in Fig. 6.3 (b)&(c)] confirms the presence of lipids at the location where the PA tissue classification shows plaque lipids. The general morphology highlighted with Resorcine Fuchsine (RF) stain [left images in Fig. 6.3 (b)&(c)] confirms the presence of a collagen rich tissue at the location where PA tissue classification shows collagen.

6.4 Discussion

The data shown in Fig. 6.3 suggest that it is possible to image atherosclerotic plaque composition using spectroscopic PA imaging in the CA. We demonstrated image contrast specific for plaque lipids in an ex vivo setting that closely mimics the in vivo geometry, exploiting endogenous absorption contrast in the wavelength range 1130-1250 nm. US imaging revealed intima thickening caused by the plaque, but could not provide tissue specific

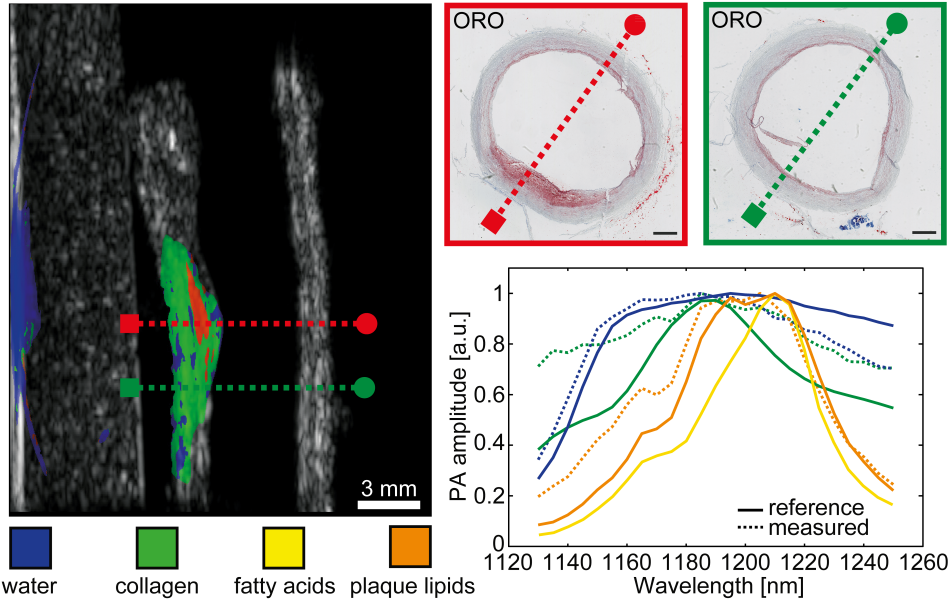


Figure 6.3: Photoacoustic (PA) imaging of a lipid plaque in a carotid artery ex vivo. Left panel: tissue composition (water, collagen, fatty acids and plaque lipids) identified by PA spectroscopy, are color coded and overlaid on the US image. Plaque lipid accumulation inside the collagen structure of the artery wall can be observed. Top right: histologic sections of two sites in the image using Oil Red O (ORO) stain indicating the presence of lipid. The dashed lines indicate the corresponding imaging plane. Right bottom: normalized reference and measured spectra used for spectral unmixing.

contrast. Figures 6.2 and 6.3 also demonstrate the feasibility of using a transmission geometry for PA carotid imaging, employing internal illumination with a small diameter optical probe and external signal detection.

The data presented here show that it is possible to use near-infrared light near $1.2 \mu\text{m}$ to image lipids at a relatively large depth, water absorption notwithstanding. The phantom used here does not mimic the complexity of the neck in terms of tissue heterogeneity, optical and acoustic attenuation. It does represent the relevant scattering and geometrical properties, however, as well as the dominant water absorption. An in-vivo imaging device would use a flexible optical probe that can be passed through the nose down to the pharynx, comparable to the position of a nasogastric feeding tube. Probe localization and positioning can be aided by real-time monitoring the PA response of the pharynx wall. The small size of such a probe (approximately 1 mm) means that patient comfort is not compromised. The optical design of the tip is subject of further study, with the aim to minimize the applied fluence, while optimizing the sensitivity and noise characteristics of the US signal detection chain. An improved signal-to-noise ratio would also permit imaging of the entire circumference of the artery [see Figs. 6.2 and 6.3]. The use of a customized transducer and optimal signal acquisition as was demonstrated in [34] could provide the means to translate this idea to an in-vivo clinical imaging device. In vivo imaging would further require improvements in speed (both scan speed and pulse rate) of the laser.

In contrast to IVPA, it is quite conceivable to perform multi-wavelength spectroscopic imaging *in vivo*. This opens up the possibility to study patient-specific plaque lipid profiles, which may provide new variables for prognostic imaging of vulnerable plaque. The example included in this study shows that lipids can be detected in a plaque that looks very mild by US, which shows a geometrical assessment only. The data we show in this letter demonstrates that this does not adequately characterize the disease. Likewise, in more advanced plaques there is a wide variety in lipid composition, and some of these components are associated with plaque instability [149]. With spectroscopic PA imaging, we may non-invasively study plaque lipidomics *in vivo*.

6.5 Conclusion

In this study, we introduced a new technique for chemically specific imaging of carotid atherosclerosis. We demonstrated that the CA can be imaged using internal illumination from the pharynx, external signal detection and external US imaging. We obtained spectral information in the wavelength range 1130-1250 nm to identify plaque specific lipids. This technique has the potential to provide new information for risk stratification or to reveal early stages of atherosclerosis, as was demonstrated in this letter with a diseased post-mortem human CCA.

Acknowledgments

The authors would like to thank Dr. Koen W.A. van Dongen and Dr. Martin D. Verweij for using the Verasonics system, which was funded by the ZonMW - *Transducer development for next generation medical ultrasound modalities* project. Also thanks to Kim van Gaalen for the histology images.

Discussion and conclusions

This thesis demonstrates several new techniques that can be used for non-invasive imaging of atherosclerotic plaques in the carotid artery (CA). The first part of the thesis deals with techniques that involve high frame rate imaging (HFRI) as a means for revealing the mechanical properties of arterial plaques. For this purpose, a new image reconstruction technique for HFRI was developed. This technique was then later extended to capture the axially oriented motion dynamics of the CA wall. This technique was tested on a group of healthy volunteers and in two patients. The difficulty of measuring tissue motion in the lateral direction was solved using a new method that was presented in the final chapter of part I. Part II of this work deals with the photoacoustic (PA) imaging technique as a means for revealing the biochemical makeup of arterial plaques. First, a new method was developed to improve conventional PA image reconstruction by using complementary ultrasound (US) images. To allow in-vivo PA imaging of the CA, a new method was proposed whereby the light to the CA is delivered using a small optical probe placed inside the pharynx. The method was tested on an ex vivo diseased carotid artery that was embedded in a neck-mimicking phantom. Spectroscopic information revealed a small lipid plaque inside this ex vivo CA. The final chapter discusses these findings and the future perspectives opened up by this research.

The use of high frame rate ultrasound

HFRI is one of the buzzwords in current research involving ultrasound (US). The term HFRI refers to all kinds of transmit-and-receive sequences that allow us to obtain images at very high acquisition rates >1000 frames per second (fps) [154]. The technique of using only a few transmissions (sometimes only one) to obtain a complete image has been around for some time [31, 144, 102, 153]. However, recent technological advancements in parallel acquisition and fast processing of large data sets, have renewed interest in this technique, leading to its successful utilization in several applications [13, 23, 110, 92, 15, 93]. Studying the HFRI technique has been further facilitated by the availability of commercial US systems, which include both systems for clinical use (Aixplorer®; SuperSonic Imaging, Aix-en-Provence France) and systems that are open and programmable.

From an academic perspective it not surprising that HFRI has received this renewed attention. After all, there are several aspects of the HFRI technique that present interesting challenges to researchers. HFRI produces a vast amount of data in a short period of time.

This data needs to be stored, transferred, processed and analysed within a reasonable time frame. It is by no means a trivial task to extract from these gigabytes of raw data just a few clinically relevant parameters. Research efforts currently have two main aims: to speed up data processing times, and to investigate whether data exploration can be made more interactive. Such studies are essential for determining the extent to which the data space is explored and exploited. The use of powerful graphic cards to this end appears to be fruitful, as chapter 2 shows. The inherent consistency of HFRI data makes it both effective and feasible to perform data conditioning, such as de-jittering prior to parameter estimation (chapter 4).

Image reconstruction is another interesting aspect of HFRI. Reconstructing a high-quality image with just one transmission and one recording is certainly challenging, especially since each additional computation must be performed on not one image but on >10,000 images per scan. Chapter 2 shows that image reconstruction performed in the frequency domain can be accurate and computationally efficient: processing only those frequencies that are inside the detection band reduces the number of computations dramatically. This approach provides the means to vary reconstruction parameters (e.g. speed of sound) in order to obtain the best reconstruction without losing too much processing time. Research on this topic is currently ongoing in our laboratory.

A further interesting challenge of HFRI lies in how to derive the desired relevant information from the data the technique generates. Although the advantage of HFRI mainly becomes apparent when it is used to visualize fast dynamic processes, visualization alone is not always enough. The related parametric information, such as arterial pulse wave speed or amount of tissue deformation, tends to be far more valuable. The required frame rates are therefore dictated by the tissue motion dynamics on the one hand and the desired spatial and temporal resolution on the other. For the CA, the lower range of 2,000 to 35,000 frames-per-second appears to be adequate for capturing all the dynamics within the artery wall [92].

In further experiments to obtain parametric information, arterial motion in the CA was studied from a longitudinal view, where the motion is predominantly axially oriented (towards and away from the transducer) (see chapter 3). The visualization of fast transient pulse-wave phenomena was used to estimate pulse wave velocities (PWV), which are associated with arterial stiffness: the stiffer the artery wall the faster the pulse wave will propagate. After looking at the velocity patterns throughout the artery wall and evaluating the variability of the PWV in subsequent cardiac cycles, it was concluded that this single parameter is unlikely to be adequate for evaluating the disease state of the artery. Moreover, the detailed motion patterns occurring in the plaques of patients with carotid artery disease are qualitatively and quantitatively different from the motion patterns occurring in the arteries of healthy volunteers. Visualization of arterial pulse waves that interact with the arterial wall may therefore provide a more complete picture of how healthy and diseased arteries behave. No other imaging technique can provide this kind of detailed information. Future studies will demonstrate how these observations can be translated into parameters that have clinical value.

Following on from the studies of arterial motion, a closer look at plaque deformation was initiated, which required an accurate method of measuring tissue displacement. Arterial plaques are subject to deformation under varying loads, and the amount of deformation,

called strain, is a reflection of plaque vulnerability. This is because locations with large tissue strain are prone to rupture [28]. However, reliable estimations of strain depends on reliable estimations of tissue displacement in all directions [61, 32]. To this end, a new method for vector displacement imaging was developed that allowed us to measure tissue displacement in two directions, instead of only the axial motion that was measured in chapter 3. This is the first method that enables imaging of tissue displacement in two dimensions with approximately uniform accuracy, as is shown in Fig. 4.6. The potential of this technique is especially highlighted by the graph in Fig. 4.6 (e), which shows that ultra-small ($< 1 \mu\text{m}$) physiological displacements can be measured in all directions in vivo.

Such measurements of ultra-small tissue motions and deformations may well enable early detection of plaques. During plaque development, the local biomechanical properties of healthy arterial tissue change as a result of the accumulation of heterologous material inside the arterial wall and the breakdown of elastin and collagen [145, 71, 50, 112]. It may be possible to use the proposed method for vector displacement imaging to reveal these small lipid-containing plaques by means of strain analysis of a complete arterial segment. Future studies will be directed at incorporating this method in the analysis of arterial tissue in terms of both strain and strain rate (strain as a function of time). Apart from use in detecting plaques, the high-definition information on healthy arterial wall motion may therefore also be used to improve current biomechanical models of arterial motion in order to better understand differences between healthy and diseased arterial tissue [155].

The image quality of HFRI will remain inferior to that of focussed imaging sequences. Despite the advantages of fast image acquisition without motion artefacts, they are superseded by the disadvantages that arise from unfocused transmissions. Therefore HFRI should be viewed mainly as a parametric imaging tool. Fruitful middle ground may well be found by using a few slow-acquisition high-quality images and overlaying them with the parametric information from HFRI. Exactly how the wealth of information from HFRI should be translated into visualization that is insightful - and into parameters that are clinically relevant - requires further dialogue between doctor and engineer.

The most pressing remaining problem of US carotid imaging (including HFRI) is the lack of 3D spatial information. While tissue structure and motion are three-dimensional, current imaging technology only allows us to sample these parameters in two-dimensional slices. We treat the images as if all dynamic phenomena occur in this 2D image plane, and disregard out-of-plane motion. Plaques that move transversely to the 2D imaging plane are treated as if the motion were within that plane. Also, the image we obtain of the carotid artery and a plaque within can be completely different if the imaging transducer is moved just a fraction of a millimetre. 3D spatial information is therefore essential for true plaque evaluation using the US technique. Future research in our laboratory will focus on this aspect [5].

The experiments reported in chapters 2, 3 and 4 describe the development of a set of image acquisition and processing techniques that enable the visualization of microscopic tissue motion with unprecedented velocity and spatial resolution. These techniques rely on fast transmission, reception and processing of US signals. The systems that are needed to perform such tasks are now available and sufficiently stable for use in small clinical trials,

for example. These trials should include the scanning of patients who are known to have mild atherosclerotic plaques within their carotid arteries or groups of patients who have high risk of developing atherosclerosis. The findings from such studies may help to foster a more complete understanding of atherosclerotic plaque formation and development and may steer the direction of further research. It may also help to establish a more complete picture of the appearance of high-risk plaques on ultrasound, from which diagnostic parameters can be derived and criteria for use in clinical practice.

Photoacoustic imaging of the carotid: a feasible technology?

PA and US imaging are techniques that provide complementary information, based on acoustic and optical contrast mechanisms. These techniques are easily integrated and when used together provide more information about the tissue of interest than when used alone. The practice of using more than one imaging modality simultaneously has become increasingly popular [115]. Chapter 5 shows that, instead of simply overlaying the images, information derived from one modality can be used to improve image reconstruction for the other modality. The method presented in chapter 5 may well indicate a direction in which the PA and US imaging techniques can be further integrated.

More detail about a tissue of interest can be obtained using PA imaging, which can be used to reveal the biochemical makeup of tissue. However, it remains difficult to obtain truly quantitative optical absorption coefficients with this technique [27]. Not all applications require an exact quantification of tissue properties: often a basic tissue characterization, based on relative spectroscopic differentiation, may be adequate for answering many diagnostic questions. Whether this is the case for PA imaging of the vulnerable plaque remains an open question. Unravelling the detailed lipid composition of arterial plaques will answer important questions regarding plaque vulnerability [149], and spectroscopic PA imaging is uniquely positioned to assess this *in vivo*. Indeed, research into intravascular PA imaging has shown the potential of using PA spectroscopy to detect lipid-rich plaques inside coronary arteries [167, 75, 77].

Chapter 6 provides proof that spectroscopic PA imaging can already reveal information on tissue composition far beyond that obtained with ultrasound. A small lipid plaque inside the artery wall of an *ex vivo* specimen of a common CA was visualized using interstitial illumination and external acoustic detection. This finding was later confirmed by histology. For the purpose of plaque detection inside this supposedly healthy tissue, a new and efficient tissue classification tool was developed that relates the experimental spectral responses to reference spectra. These findings suggest that PA imaging may not only be useful for imaging plaque vulnerability but also for early plaque detection.

Despite its advantages, PA imaging of the CA *in vivo* poses some serious challenges. The most difficult challenge is the amount of light that can be delivered to the CA, since it is a relatively deep target for PA imaging. For endogenous lipid detection in carotid plaques it is advisable to use light in the 1200 nm wavelength range, where lipid shows distinct absorption. The disadvantage of these wavelengths is that they are also highly attenuated by tissues containing water. After 1 cm of water, only 35 % of the initial light is left. Unfortunately, a large proportion of people at risk of developing atherosclerosis have more subcutaneous fat,

resulting in even more absorption of the light that is applied to the skin [41]. To counter this problem, a new idea was tested in which the light to the CA is administered from within the body, thereby circumventing the long optical path from the skin to the CA. By using a small optical probe that can be placed inside the pharynx, the optical path is shortened and light absorption and scattering by the skin is avoided [10].

This idea (known as transmission geometry) was presented and tested in an *ex vivo* setting, as described in chapter 6. In addition to the rigid optical probe applied in chapter 6, a more realistic probe was built using the same 400 μm side-firing optical fibre. This fibre was now fed through a double-wound spring with an outer diameter of 0.8 mm (Boston Scientific), allowing the fibre to be rotated $>90^\circ$. The fibre/spring assembly was inserted into a transparent tube with an outer diameter of 1.2 mm (made from a medically approved polymer Pebax ®7233), allowing the probe to be moved safely up and down the pharynx with minimal friction.

The optical probe depicted in Fig. 7.1 (a) was tested *in vivo* in a healthy volunteer. One of the first results of this initial test can be seen in Fig. 7.1 (b). In this image, the PA signals are shown in red overlay on top of a greyscale US image. For this scan infra-red light of 800 nm was used to target blood absorption in the CA. Although unfortunately no direct signal from the CA was obtained, it was very encouraging to obtain PA signals using interstitial illumination. This experiment confirmed that this probe was easily inserted, well tolerated and could be kept stable during scanning.

As mentioned above, transmission geometry using a small optical fibre probe for light delivery has several advantages. A potential downside however is the high fluence at the tip and the rapid fall-off, due to beam divergence, when the light reaches the CA. The loss in fluence of 1200 nm light through 1.5 cm of tissue for this probe is about 3 orders of magnitude due to tissue scattering and beam divergence. By shaping the optical beam to be more directional some of this loss could be regained.

Photoacoustic signal detection

In conventional US imaging we transmit and receive signals with the same transducer. This means that the echoes from the backscattering tissue match the frequency at which the transducer works optimally. This is not the case for PA imaging. The PA signal that is generated by the tissue has a range of frequencies that depends on parameters such as the size, shape and material of the tissue, as well as the duration of the laser pulse [163, 120, 68, 127]. PA imaging generally uses light excitation with nanosecond pulses. Such short pulses are desirable because maximum energy conversion is achieved when the heating period is shorter than the acoustic travel time through the source (also known as the stress confinement condition). This means that PA signals are inherently broadband (> 100 MHz). The most efficient, reliable and common transducers that convert acoustic pressure into an electric signal are based on piezoelectric crystals [11]. These crystals are resonators, meaning that they are particularly efficient within a limited frequency band that is close to their own resonance. Which frequency should be chosen for PA imaging of the atherosclerotic plaque in the CA remains an open question. In Fig. 7.2 frequencies are shown that can be expected from a lipid-loaded atherosclerotic plaque inside the arterial wall, as a function of lipid pool size. The findings in Fig. 7.2 are based on PA wave-field simulations

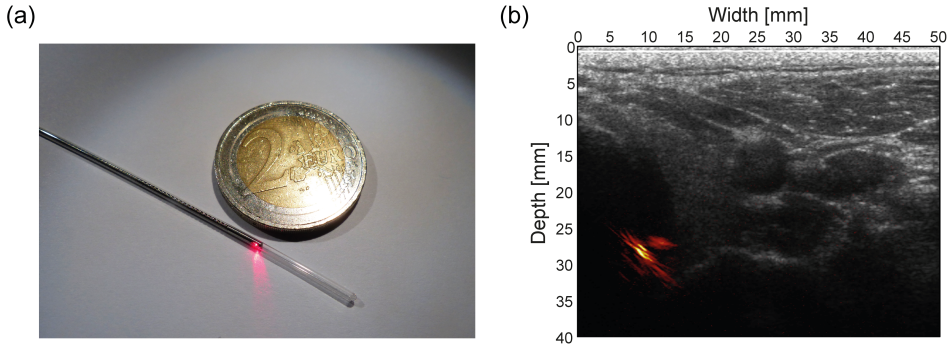


Figure 7.1: **First proof of interstitial illumination of the carotid artery in vivo** (a) Photograph of the first probe prototype that was used to illuminate the carotid artery of a healthy volunteer. (b) Ultrasound image of the carotid artery of the healthy volunteer with red overlay showing the photoacoustic signals that were detected.

that were performed using the freely available Matlab toolbox *k-Wave* for acoustic field simulation that was developed by Cox and Treeby [3, 26, 158]. Here the plaque size was varied according to the model discussed in [6]. The acoustic parameters for the simulations were as follows: a 3D grid sized $1024 \times 2048 \times 16$, spanning an area of $50 \times 100 \times 8$ mm. The grid spacing allowed a maximum acoustic frequency of 15 MHz (finer grid spacing did not provide additional information). The speed of sound ranged between 1480 and 1570 m/s with a frequency-dependent acoustic absorption of 0.5 dB/cm/MHz. Light attenuation was set to 0.7 cm^{-1} . The simulated receivers were placed approximately 35 mm away from the atherosclerotic plaque.

From Fig. 7.2 it is immediately clear that the bulk of photoacoustic energy is confined to the low frequency range (10 kHz – 5 MHz). This range is below the 5-10 MHz band that

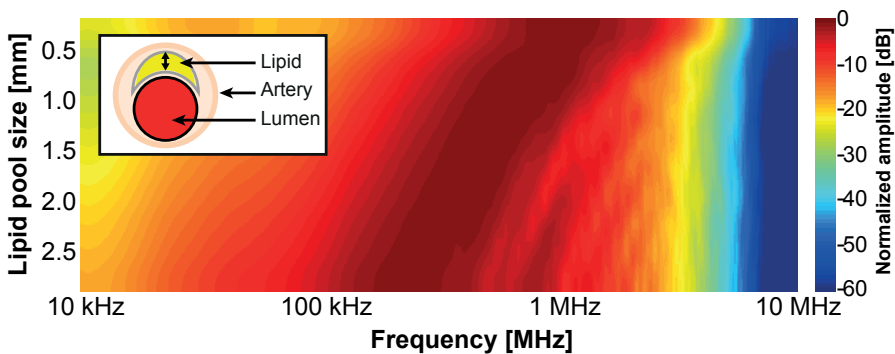


Figure 7.2: **Lipid-loaded plaques produce low-frequency photoacoustic waves** The figure shows the frequency spectra (horizontal axis) of the photoacoustic waves resulting from lipid-loaded atherosclerotic plaques as a function of plaque size (vertical axis). The spectra were obtained with the Matlab toolbox *k-Wave* for PA wave field simulation.

is normally used for US carotid scanning. The dominance of the low frequencies is partly attributed to the acoustic absorption of the higher frequencies but mainly to the size and homogeneity of the simulated plaque.

Chapter 5 shows that PA signals emerging from structures such as the CA can be highly directional. The linear arrays that are commonly used for US carotid imaging are not suitable for detecting the highly directional signals that originate from the sides of the CA. This phenomenon is referred to as the limited view problem. It is a problem that has been recognized by the PA research community and that has prompted the development of specialized concave transducers [151, 34, 30]. A concave transducer has an aperture that is larger than normal and it is automatically focused as a result of its geometry, providing a distinctive advantage over linear transducers. Not only does its concave transducer adequately sample a much larger fraction of the emitted wave front - because it has a larger aperture - but also the directional sensitivity of its elements is better matched with the local emitted wave vectors.

Lipid-loaded carotid plaques can be imaged using endogenous contrast as was shown in chapter 6. Using spectroscopic information connective arterial tissue was also successfully identified. However, the optical absorption of tissues such as collagen and calcium is weak and lacks defined spectral features, which makes imaging such tissues at great depth difficult. Recent advances in the development of exogenous contrast agents for PA imaging - such as plasmonic nanoparticles - are promising and it is possible that such techniques will be used to image deep targets inside the body [106]. These contrast agents can be spectrally tuned and labelled to provide contrast for specific cells or tissues [168].

Most of the challenges described above are of technological nature and can be solved with dedicated development efforts. Such research should also investigate whether or not a probe placed inside the pharynx can safely deliver sufficient light for PA imaging. Although the in vivo experiments were limited by the available laser power, and not by safety concerns, it is clear that there is a limit. In practice, damage as a result of nanosecond laser pulses is mainly thermal [4], which means that low pulse rate lasers (< 100 Hz) can be applied with significant pulse energy before tissue damage occurs. Nevertheless, the option for external light delivery should not be discarded too easily. The importance of detecting early plaques and vulnerable plaques in vivo warrants exploration of all possible avenues.

There are many open questions regarding our understanding of the development of atherosclerosis in the CA. Current screening strategies for patients at risk of stroke are inadequate, but it is unclear how we can do better. A complete understanding of CA atherosclerosis requires imaging of all stages of the disease, from early formation to the verge of rupture, and this information cannot be obtained without in vivo imaging. The techniques developed and presented in this thesis are tailored towards non-invasive imaging of CA arteriosclerotic plaques. Some of the techniques can be directly applied in small clinical studies. Others, such as photoacoustic imaging of the carotid artery, require further research and technological development. I hope that these techniques may ultimately contribute to better understanding, detection and treatment of CA atherosclerosis in the CA.

Not in the very near future but perhaps soon after, we may face a daily practice where

the techniques that were discussed in this thesis are the main diagnostic tools used to scan people for carotid atherosclerosis. In this scenario, a person with a high chance of developing atherosclerosis goes to their doctor for 3D HFRI scans of both CAs. The HFRI scan is used to generate a risk profile and a suspicious plaque is found. The person is then examined further using PA carotid imaging: a small dose of lidocaine is given before an optical probe is inserted through the person's nose into the pharynx, where it illuminates the CA. Spectral analysis shows that the plaque contains elevated levels of cholesterol linoleate. Based on these findings, the practitioner decides to prescribe a recently developed statin that is known to stabilize these specific plaques and asks the newly identified patient to return after a year or two, confident that she is safe from cerebrovascular events, with tailored medication that causes the plaque to regress and stabilize.

Conclusions

- Fast image reconstruction required for high frame-rate imaging can be fast and accurately computed using a non-uniform fast Fourier transform (Chapter 2).
- The natural deformations of the human carotid artery wall include displacements in sub-micrometer dimensions on a sub-millisecond time scale. These tissue dynamics can be visualized in unprecedented detail using high frame-rate imaging (Chapter 3).
- Accurate assessment of rapid tissue motion requires high frame-rate imaging and two dimensional displacement estimation with sub-micrometer resolution. This two-dimensional displacement vector can be measured in-vivo using signal delays obtained with high frame-rate plane wave imaging prior image reconstruction (Chapter 4).
- Photoacoustic image reconstruction can be improved using information derived from a co-registered ultrasound image (Chapter 5).
- Photoacoustic spectroscopy using internal illumination can reveal lipid loaded plaques inside a diseased post-mortem carotid artery (Chapter 6).

References

- [1] <http://www.cirsinc.com/products/modality/67/multi-purpose-multi-tissue-ultrasound-phantom/?de-tails=specs>. 25 june 2012.
- [2] <http://www.eecs.umich.edu/~fessler/code/index.html>. 25 june 2012.
- [3] <http://www.k-wave.org/>.
- [4] <http://www.lia.org/publications/ansi/z136-3/>.
- [5] Stw-project: 3d plane-wave ultrasound matrix transducer for carotid artery diagnosis (puma).
- [6] Ali C Akyildiz, Lambert Speelman, Harald van Brummelen, Miguel A Gutiérrez, Renu Virmani, Aad van der Lugt, AF Van Der Steen, Jolanda J Wentzel, and FJ Gijzen. Effects of intima stiffness and plaque morphology on peak cap stress. *Biomed Eng Online*, 10(1):1–13, 2011.
- [7] T.J. Allen and P.C. Beard. Photoacoustic characterisation of vascular tissue at NIR wavelengths. In *Proc. of SPIE Vol*, volume 7177, pages 71770A–1, 2009.
- [8] Roland Asmar, Athanase Benetos, Jirar Topouchian, Pierre Laurent, Bruno Pannier, Anne-Marie Brisac, Ralph Target, and Bernard I Levy. Assessment of arterial distensibility by automatic pulse wave velocity measurement validation and clinical application studies. *Hypertension*, 26(3):485–490, 1995.
- [9] Henry JM Barnett, D Wayne Taylor, Michael Eliasziw, Allan J Fox, Gary G Ferguson, R Brian Haynes, Richard N Rankin, G Patrick Clagett, Vladimir C Hachinski, David L Sackett, et al. Benefit of carotid endarterectomy in patients with symptomatic moderate or severe stenosis. *New England Journal of Medicine*, 339(20):1415–1425, 1998.
- [10] A.N. Bashkatov, E.A. Genina, V.I. Kochubey, and V.V. Tuchin. Optical properties of human skin, subcutaneous and mucous tissues in the wavelength range from 400 to 2000 nm. *Journal of Physics D: Applied Physics*, 38(15):2543–2555, 2005.
- [11] P. Beard. Biomedical photoacoustic imaging. *Interface Focus*, 1(4):602–631, 2011.
- [12] M. Benthin, P. Dahl, R. Ruzicka, and K. Lindström. Calculation of pulse-wave velocity using cross correlation-effects of reflexes in the arterial tree. *Ultrasound in Medicine & Biology*, 17(5):461–469, 1991.
- [13] J. Bercoff, M. Tanter, and M. Fink. Supersonic shear imaging: a new technique for soft tissue elasticity mapping. *Ultrasonics, Ferroelectrics and Frequency Control, IEEE Transactions on*, 51(4):396–409, 2004.
- [14] G. Beylkin. On the fast Fourier transform of functions with singularities. *Applied and Computational Harmonic Analysis*, 2(4):363–381, 1995.
- [15] Birger Brekke, Lars CL Nilsen, Joakim Lund, Hans Torp, Tore Bjastad, Brage H Amundsen, Asbjorn Stoylen, and Svein A Aase. Ultra-high frame rate tissue doppler imaging. *Ultrasound in Medicine & Biology*, 40(1):222–231, 2014.
- [16] M.M. Bronstein, A.M. Bronstein, M. Zibulevsky, and H. Azhari. Reconstruction in diffraction ultrasound tomography using nonuniform fft. *Medical Imaging, IEEE Transactions on*, 21(11):1395–1401, 2002.
- [17] J. Cai, T.S. Hatsukami, M.S. Ferguson, W.S. Kerwin, T. Saam, B. Chu, N. Takaya, N.L. Polissar, and C. Yuan. In vivo quantitative measurement of intact fibrous cap and lipid-rich necrotic core size in atherosclerotic carotid plaque. *Circulation*, 112(22):3437–3444, 2005.
- [18] Sandra Carr, Andrew Farb, William H Pearce, Renu Virmani, and James ST Yao. Atherosclerotic plaque rupture in symptomatic carotid artery stenosis. *Journal of Vascular Surgery*, 23(5):755–766, 1996.
- [19] George C Cheng, Howard M Loree, Roger D Kamm, Michael C Fishbein, and Richard T Lee. Distribution of circumferential stress in ruptured and stable atherosclerotic lesions. a structural analysis with histopathological correlation. *Circulation*, 87(4):1179–1187, 1993.
- [20] J. Cheng and J. Lu. Extended high-frame rate imaging method with limited-diffraction beams. *Ultrasonics, Ferroelectrics and Frequency Control, IEEE Transactions on*, 53(5):880–899, 2006.
- [21] J.R. Cook, R.R. Bouchard, and S.Y. Emelianov. Tissue-mimicking phantoms for photoacoustic and ultrasonic imaging. *Biomedical Optics Express*, 2(11):3193–3206, 2011.
- [22] M. Couade, M. Pernot, E. Messas, J. Emmerich, A. Hagège, M. Fink, and M. Tanter. Ultrafast imaging of the arterial pulse wave. *IRBM*, 2011.
- [23] M. Couade, M. Pernot, C. Prada, E. Messas, J. Emmerich, P. Bruneval, A. Criton, M. Fink, and M. Tanter. Quantitative assessment of arterial wall biomechanical properties using shear wave imaging. *Ultrasound in Medicine & Biology*, 36(10):1662–1676, 2010.
- [24] Ben Cox, Jan G Laufer, Simon R Arridge, and Paul C Beard. Quantitative spectroscopic photoacoustic imaging: a review. *Journal of Biomedical Optics*, 17(6):0612021–0612022, 2012.

- [25] B.T. Cox and P.C. Beard. Fast calculation of pulsed photoacoustic fields in fluids using k-space methods. *The Journal of the Acoustical Society of America*, 117:3616–3627, 2005.
- [26] B.T. Cox, S. Kara, S.R. Arridge, and P.C. Beard. k-space propagation models for acoustically heterogeneous media: Application to biomedical photoacoustics. *The Journal of the Acoustical Society of America*, 121:3453–3464, 2007.
- [27] BT Cox, JG Laufer, and PC Beard. The challenges for quantitative photoacoustic imaging. In *SPIE BiOS: Biomedical Optics*, page 717713. International Society for Optics and Photonics, 2009.
- [28] C.L. de Korte, M.J. Siervogel, F. Mastik, C. Strijder, J.A. Schaar, E. Velema, G. Pasterkamp, PW Serruys, and A.F.W. van der Steen. Identification of atherosclerotic plaque components with intravascular ultrasound elastography in vivo a yucatan pig study. *Circulation*, 105(14):1627–1630, 2002.
- [29] CL De Korte, AFW Van der Steen, BHJ Dijkman, and CT Lancée. Performance of time delay estimation methods for small time shifts in ultrasonic signals. *Ultrasonics*, 35(4):263–274, 1997.
- [30] Xosé Luís Deán-Ben and Daniel Razansky. Functional optoacoustic human angiography with handheld video rate three dimensional scanner. *Photoacoustics*, 1(3):68–73, 2013.
- [31] B Delannoy, R Torguet, C Bruneel, E Bridoux, JM Rouvaen, and H Lasota. Acoustical image reconstruction in parallel-processing analog electronic systems. *Journal of Applied Physics*, 50(5):3153–3159, 1979.
- [32] J. D’Hooge, A. Heimdal, F. Jamal, T. Kukulski, B. Bijnens, F. Rademakers, L. Hatle, P. Suetens, and GR. Sutherland. Regional strain and strain rate measurements by cardiac ultrasound: principles, implementation and limitations. *European Journal of Echocardiography*, 1(3):154–170, 2000.
- [33] G.J. Diebold, T. Sun, and M.I. Khan. Photoacoustic monopole radiation in one, two, and three dimensions. *Physical Review Letters*, 67(24):3384–3387, 1991.
- [34] Alexander Dima and Vasilis Ntziachristos. Non-invasive carotid imaging using optoacoustic tomography. *Optics Express*, 20(22):25044–25057, 2012.
- [35] B Dunmire, KW Beach, M Plett, DE Strandness Jr, et al. Cross-beam vector doppler ultrasound for angle-independent velocity measurements. *Ultrasound in Medicine & Biology*, 26(8):1213–1235, 2000.
- [36] A. Dutt and M.D. Rokhlin. Fast Fourier transforms for nonequidistant data. *SIAM Journal on Scientific Computing*, 17(6):1368–1393, 1993.
- [37] IK Ekroll, A Swillens, P Segers, T Dahl, H Torp, and L Lovstakken. Simultaneous quantification of flow and tissue velocities based on multi-angle plane wave imaging. *Ultrasonics, Ferroelectrics and Frequency Control, IEEE Transactions on*, 60(4):727–738, 2013.
- [38] S.Y. Emelianov, S.R. Aglyamov, A.B. Karpiouk, S. Mallidi, S. Park, S. Sethuraman, J. Shah, R.W. Smalling, J.M. Rubin, and W.G. Scott. Synergy and applications of combined ultrasound, elasticity, and photoacoustic imaging. In *Proceedings of the 2006 IEEE International Ultrasonics Symposium*, volume 10, pages 405–415, 2006.
- [39] A. Eriksson, E. Greiff, T. Loupas, M. Persson, and P. Pesque. Arterial pulse wave velocity with tissue doppler imaging. *Ultrasound in Medicine & Biology*, 28(5):571–580, 2002.
- [40] Erling Falk, Prediman K Shah, and Valentin Fuster. Coronary plaque disruption. *Circulation*, 92(3):657–671, 1995.
- [41] Giamila Fantuzzi and Theodore Mazzone. Adipose tissue and atherosclerosis exploring the connection. *Arteriosclerosis, Thrombosis, and Vascular Biology*, 27(5):996–1003, 2007.
- [42] ZA Fayad and V Fuster. Clinical imaging of the high-risk or vulnerable atherosclerotic plaque. *Circulation Research*, 89(4):305–316, 2001.
- [43] CV Felton, D Crook, MJ Davies, and MF Oliver. Relation of plaque lipid composition and morphology to the stability of human aortic plaques. *Arteriosclerosis, thrombosis, and vascular biology*, 17(7):1337–1345, 1997.
- [44] Gary G Ferguson, Michael Eliasziw, Hugh WK Barr, G Patrick Clagett, Robert W Barnes, M Christopher Wallace, D Wayne Taylor, R Brian Haynes, Jane W Finan, Vladimir C Hachinski, et al. The north american symptomatic carotid endarterectomy trial surgical results in 1415 patients. *Stroke*, 30(9):1751–1758, 1999.
- [45] J.A. Fessler and B.P. Sutton. Nonuniform fast Fourier transforms using min-max interpolation. *Signal Processing, IEEE Transactions on*, 51(2):560–574, 2003.
- [46] Alope V Finn, Masataka Nakano, Jagat Narula, Frank D Kolodgie, and Renu Virmani. Concept of vulnerable/unstable plaque. *Arteriosclerosis, Thrombosis, and Vascular Biology*, 30(7):1282–1292, 2010.
- [47] SW Flax and Matthew O’Donnell. Phase-aberration correction using signals from point reflectors and diffuse scatterers: Basic principles. *Ultrasonics, Ferroelectrics and Frequency Control, IEEE Transactions on*, 35(6):758–767, 1988.
- [48] Y. Fung. *Biomechanics: Mechanical Properties of Living Tissues*. New York: Springer, 1993.
- [49] Valentin Fuster, Pedro R Moreno, Zahi A Fayad, Roberto Corti, and Juan J Badimon. Atherothrombosis and high-risk plaquepart i: evolving concepts. *Journal of the American College of Cardiology*, 46(6):937–954, 2005.
- [50] T Christian Gasser, Ray W Ogden, and Gerhard A Holzapfel. Hyperelastic modelling of arterial layers with distributed collagen fibre orientations. *Journal of the royal society interface*, 3(6):15–35, 2006.
- [51] Spyretta Golemati, Antonio Sassano, M John Lever, Anil A Bharath, Surinder Dhanjil, and Andrew N Nico-

- laides. Carotid artery wall motion estimated from b-mode ultrasound using region tracking and block matching. *Ultrasound in Medicine & Biology*, 29(3):387–399, 2003.
- [52] L. Greengard and J.Y. Lee. Accelerating the nonuniform fast Fourier transform. *SIAM review*, 46(3):443–454, 2004.
- [53] Marie-Louise M Grønholdt. Ultrasound and lipoproteins as predictors of lipid-rich, rupture-prone plaques in the carotid artery. *Arteriosclerosis, Thrombosis, and Vascular Biology*, 19(1):2–13, 1999.
- [54] Marie-Louise M Grønholdt, Borge G Nordestgaard, Torben V Schroeder, Sissel Vorstrup, and Henrik Sillesen. Ultrasonic echolucent carotid plaques predict future strokes. *Circulation*, 104(1):68–73, 2001.
- [55] Pierre Gueth, Philippe Delachartre, and Hervé Liebgott. Motion estimation using prebeamformed ultrasound signals. In *Ultrasonics Symposium (IUS), 2010 IEEE*, pages 2004–2007. IEEE, 2010.
- [56] Zijian Guo, Li Li, and Lihong V Wang. On the speckle-free nature of photoacoustic tomography. *Medical Physics*, 36(9):4084–4088, 2009.
- [57] M. Haltmeier, O. Scherzer, and G. Zangerl. A reconstruction algorithm for photoacoustic imaging based on the nonuniform fft. *Medical Imaging, IEEE Transactions on*, 28(11):1727–1735, 2009.
- [58] Craig J Hartley, Harvey Litowitz, Raphael S Rabinovitz, W-X Zhu, Jacques E Chelly, Lloyd H Michael, and Roberto Bolli. An ultrasonic method for measuring tissue displacement: Technical details and validation for measuring myocardial thickening. *Biomedical Engineering, IEEE Transactions on*, 38(8):735–747, 1991.
- [59] Hideyuki Hasegawa, Kazue Hongo, and Hiroshi Kanai. Measurement of regional pulse wave velocity using very high frame rate ultrasound. *Journal of Medical Ultrasonics*, 40(2):91–98, 2013.
- [60] Hideyuki Hasegawa and Hiroshi Kanai. Simultaneous imaging of artery-wall strain and blood flow by high frame rate acquisition of rf signals. *Ultrasonics, Ferroelectrics and Frequency Control, IEEE Transactions on*, 55(12):2626–2639, 2008.
- [61] A. Heimdal, A. Støylen, H. Torp, and T. Skjæ rpe. Real-time strain rate imaging of the left ventricle by ultrasound. *Journal of the American Society of Echocardiography*, 11(11):1013–1019, 1998.
- [62] Willem E Hellings, Wouter Peeters, Frans L Moll, Sebastiaan RD Piers, Jessica van Setten, Peter J Van der Spek, Jean-Paul PM de Vries, Kees A Seldenrijk, Peter C De Bruin, Aryan Vink, et al. Composition of carotid atherosclerotic plaque is associated with cardiovascular outcome a prognostic study. *Circulation*, 121(17):1941–1950, 2010.
- [63] E. Hermeling, K.D. Reesink, L.M. Kornmann, R.S. Reneman, and A.P.G. Hoeks. The dirotic notch as alternative time-reference point to measure local pulse wave velocity in the carotid artery by means of ultrasonography. *Journal of Hypertension*, 27(10):2028–2035, 2009.
- [64] Evelien Hermeling, Koen D Reesink, Robert S Reneman, and Arnold PG Hoeks. Measurement of local pulse wave velocity: effects of signal processing on precision. *Ultrasound in Medicine & Biology*, 33(5):774–781, 2007.
- [65] Evelien Hermeling, Koen D Reesink, Robert S Reneman, and Arnold PG Hoeks. Confluence of incident and reflected waves interferes with systolic foot detection of the carotid artery distension waveform. *Journal of Hypertension*, 26(12):2374–2380, 2008.
- [66] Evelien Hermeling, Robert S Reneman, Arnold PG Hoeks, and Koen D Reesink. Advances in arterial stiffness assessment. *Artery Research*, 5(4):130–136, 2011.
- [67] APG Hoeks, PJ Brands, FAM Smets, and RS Reneman. Assessment of the distensibility of superficial arteries. *Ultrasound in Medicine & Biology*, 16(2):121–128, 1990.
- [68] C.G.A. Hoelen and F.F.M. de Mul. Image reconstruction for photoacoustic scanning of tissue structures. *Applied Optics*, 39(31):5872–5883, 2000.
- [69] DW Holdsworth, CJD Norley, R. Frayne, DA Steinman, and BK Rutt. Characterization of common carotid artery blood-flow waveforms in normal human subjects. *Physiological Measurement*, 20(3):219, 1999.
- [70] Iben Kraglund Holfort, Fredrik Gran, and Jorgen Arendt Jensen. Broadband minimum variance beamforming for ultrasound imaging. *Ultrasonics, Ferroelectrics and Frequency Control, IEEE Transactions on*, 56(2):314–325, 2009.
- [71] Gerhard A Holzapfel, Gerhard Sommer, and Peter Regitnig. Anisotropic mechanical properties of tissue components in human atherosclerotic plaques. *Journal of Biomechanical Engineering*, 126(5):657–665, 2004.
- [72] Y. Inaba, J.A. Chen, and S.R. Bergmann. Carotid plaque, compared with carotid intima-media thickness, more accurately predicts coronary artery disease events: a meta-analysis. *Atherosclerosis*, 220(1):128–133, 2012.
- [73] M Jaeger, S Preisser, M Kitz, D Ferrara, S Senegas, D Schweizer, and M Frenz. Improved contrast deep optoacoustic imaging using displacement-compensated averaging: breast tumour phantom studies. *Physics in Medicine and Biology*, 56(18):5889–5901, 2011.
- [74] Michael Jaeger, Lea Siegenthaler, Michael Kitz, and Martin Frenz. Reduction of background in optoacoustic image sequences obtained under tissue deformation. *Journal of Biomedical Optics*, 14(5):054011, 2009.
- [75] K. Jansen, A.F.W. Van der Steen, H.M.M. van Beusekom, J.W. Oosterhuis, and G. van Soest. Intravascular photoacoustic imaging of human coronary atherosclerosis. *Optics Letters*, 36(5):597–599, 2011.
- [76] Krista Jansen, Antonius FW van der Steen, Min Wu, Heleen MM van Beusekom, Geert Springeling, Xiang Li, Qifa Zhou, K Kirk Shung, Dominique PV de Kleijn, and Gijs van Soest. Spectroscopic intravascular

- photoacoustic imaging of lipids in atherosclerosis. *Journal of Biomedical Optics*, 19(2):026006–026006, 2014.
- [77] Krista Jansen, Gijs van Soest, and Antonius FW van der Steen. Intravascular photoacoustic imaging: A new tool for vulnerable plaque identification. *Ultrasound in Medicine & Biology*, 2014.
- [78] Krista Jansen, Min Wu, Antonius FW van der Steen, and Gijs van Soest. Lipid detection in atherosclerotic human coronaries by spectroscopic intravascular photoacoustic imaging. *Optics Express*, 21(18):21472–21484, 2013.
- [79] Jørgen Arendt Jensen and Peter Munk. A new method for estimation of velocity vectors. *Ultrasonics, Ferroelectrics and Frequency Control, IEEE Transactions on*, 45(3):837–851, 1998.
- [80] X. Jin and L.V. Wang. Thermoacoustic tomography with correction for acoustic speed variations. *Physics in Medicine and Biology*, 51(24):6437–6448, 2006.
- [81] H. Kanai, A. Umezawa, and Y. Koiwa. Transcutaneous measurement of frequency dispersion in the regional pulse wave velocity. In *Ultrasonics Symposium, 2000 IEEE*, volume 2, pages 1281–1284. IEEE, 2000.
- [82] Hiroshi Kanai. Propagation of vibration caused by electrical excitation in the normal human heart. *Ultrasound in Medicine & Biology*, 35(6):936–948, 2009.
- [83] Chihiro Kasai, Koroku Namekawa, Akira Koyano, and Ryozo Omoto. Real-time two-dimensional blood flow imaging using an autocorrelation technique. *IEEE Trans. Sonics Ultrason*, 32(3):458–464, 1985.
- [84] J. Keiner, S. Kunis, and D. Potts. Using NFFT 3—a software library for various nonequispaced fast Fourier transforms. *ACM Transactions on Mathematical Software (TOMS)*, 36(4):19, 2009.
- [85] R Kelly, C Hayward, A Avolio, and M O'Rourke. Noninvasive determination of age-related changes in the human arterial pulse. *Circulation*, 80(6):1652–1659, 1989.
- [86] A. Kharine, S. Manohar, R. Seeton, R.G.M. Kolkman, R.A. Bolt, W. Steenbergen, and F.F.M. Mul. Poly (vinyl alcohol) gels for use as tissue phantoms in photoacoustic mammography. *Physics in Medicine and Biology*, 48:357–370, 2003.
- [87] C. Kim, T.N. Erpelding, L. Jankovic, M.D. Pashley, and L.V. Wang. Deeply penetrating in vivo photoacoustic imaging using a clinical ultrasound array system. *Biomedical Optics Express*, 1(1):278–284, 2010.
- [88] Seungsoo Kim, Yun-Sheng Chen, Geoffrey P Luke, and Stanislav Y Emelianov. In vivo three-dimensional spectroscopic photoacoustic imaging for monitoring nanoparticle delivery. *Biomedical Optics Express*, 2(9):2540–2550, 2011.
- [89] T. Koivistoinen, T. Kööbi, A. Jula, N. Hutri-Kähönen, O.T. Raitakari, S. Majahalmel, K. Kukkonen-Harjula, T. Lehtimäki, A. Reunanen, J. Viikari, V. Turjanmaa, Nieminen T, and M Kähönen. Pulse wave velocity reference values in healthy adults aged 26–75 years. *Clinical Physiology and Functional Imaging*, 27(3):191–196, 2007.
- [90] DJ Korteweg. Ueber die fortpflanzungsgeschwindigkeit des schalles in elastischen röhren. *Annalen der Physik*, 241(12):525–542, 1878.
- [91] Pieter Kruizinga, Frits Mastik, Nico de Jong, AFW van der Steen, and G van Soest. Plane-wave ultrasound beamforming using a nonuniform fast fourier transform. *Ultrasonics, Ferroelectrics and Frequency Control, IEEE Transactions on*, 59(12):2684–2691, 2012.
- [92] Pieter Kruizinga, Frits Mastik, Nico de Jong, Anton FW van der Steen, and Gijs van Soest. High frame rate ultrasound imaging of human carotid artery dynamics. In *Ultrasonics Symposium (IUS), 2012 IEEE International*, pages 1177–1180. IEEE, 2012.
- [93] Pieter Kruizinga, Frits Mastik, Stijn CH van den Oord, Arend FL Schinkel, Johannes G Bosch, Nico de Jong, Gijs van Soest, and Anton FW van der Steen. High-definition imaging of carotid artery wall dynamics. *Ultrasound in Medicine & Biology*, 40(10):2392–2403, 2014.
- [94] RM Kwee, RJ Van Oostenbrugge, L Hofstra, GJ Teule, JMA van Engelsehoven, WH Mess, and ME Kooi. Identifying vulnerable carotid plaques by noninvasive imaging. *Neurology*, 70(24 Part 2):2401–2409, 2008.
- [95] Pierre Lantelme, Christine Mestre, Michel Lievre, Alain Gressard, and Hugues Milon. Heart rate an important confounder of pulse wave velocity assessment. *Hypertension*, 39(6):1083–1087, 2002.
- [96] S. Laurent, J. Cockcroft, L. Van Bortel, P. Boutouyrie, C. Giannattasio, D. Hayoz, B. Pannier, C. Vlachopoulos, I. Wilkinson, and H. Struijker-Boudier. Expert consensus document on arterial stiffness: methodological issues and clinical applications. *European Heart Journal*, 27(21):2588–2605, 2006.
- [97] Peter Libby and Daniel I Simon. Inflammation and thrombosis the clot thickens. *Circulation*, 103(13):1718–1720, 2001.
- [98] QH Liu and N. Nguyen. An accurate algorithm for nonuniform fast Fourier transforms (NUFFT's). *Microwave and Guided Wave Letters, IEEE*, 8(1):18–20, 1998.
- [99] Donald Lloyd-Jones, Robert J Adams, Todd M Brown, Mercedes Carnethon, Shifan Dai, MD Giovanni De Simone, T Bruce Ferguson, Earl Ford, Karen Furie, Cathleen Gillespie, et al. Heart disease and stroke statistics-2010 update A report from the American Heart Association. *Circulation*, 121(7):46–215, 2010.
- [100] M.W. Lorenz, H.S. Markus, M.L. Bots, M. Rosvall, and M. Sitzer. Prediction of clinical cardiovascular events with carotid intima-media thickness a systematic review and meta-analysis. *Circulation*, 115(4):459–467, 2007.
- [101] J. Lu. Effects of data density of echo Fourier domain on quality of high frame rate imaging. In *Proceedings IEEE*

- Ultrasonics Symposium, 2008*, pages 974–977.
- [102] J. Lu. 2d and 3d high frame rate imaging with limited diffraction beams. *Ultrasonics, Ferroelectrics and Frequency Control, IEEE Transactions on*, 44(4):839–856, 1997.
- [103] J. Lu. Experimental study of high frame rate imaging with limited diffraction beams. *Ultrasonics, Ferroelectrics and Frequency Control, IEEE Transactions on*, 45(1):84–97, 1998.
- [104] J. Lu and S.J. Kwon. Simplification of high frame rate imaging system with coordinate rotation. *Ultrasonics, Ferroelectrics and Frequency Control, IEEE Transactions on*, pages 33–36, 2007.
- [105] Mark A Lubinski, Stanislav Y Emelianov, and Matthew O'Donnell. Speckle tracking methods for ultrasonic elasticity imaging using short-time correlation. *Ultrasonics, Ferroelectrics and Frequency Control, IEEE Transactions on*, 46(1):82–96, 1999.
- [106] Geoffrey P Luke, Doug Yeager, and Stanislav Y Emelianov. Biomedical applications of photoacoustic imaging with exogenous contrast agents. *Annals of biomedical engineering*, 40(2):422–437, 2012.
- [107] J. Luo, RX Li, and EE Konofagou. Pulse wave imaging of the human carotid artery: an in vivo feasibility study. *Ultrasonics, Ferroelectrics and Frequency Control, IEEE Transactions on*, 59(1):174–181, 2012.
- [108] Jianwen Luo, Kui Ying, Ping He, and Jing Bai. Properties of savitzky–golay digital differentiators. *Digital Signal Processing*, 15(2):122–136, 2005.
- [109] Aldons J. Lusis. Atherosclerosis. *Nature*, 407(6801):233–241, 2000.
- [110] E. Macé, G. Montaldo, I. Cohen, M. Baulac, M. Fink, and M. Tanter. Functional ultrasound imaging of the brain. *Nature Methods*, 8(8):662–664, 2011.
- [111] S. Manohar, R.G.H. Willemlink, F. van der Heijden, C.H. Slump, and T.G. van Leeuwen. Concomitant speed-of-sound tomography in photoacoustic imaging. *Applied Physics Letters*, 91:131911, 2007.
- [112] Pascal Maurice, Sébastien Blaise, Stéphanie Gayral, Laurent Debelle, Muriel Laffargue, William Hornebeck, and Laurent Duca. Elastin fragmentation and atherosclerosis progression: The elastokine concept. *Trends in cardiovascular medicine*, 23(6):211–221, 2013.
- [113] G. Montaldo, M. Tanter, J. Bercoff, N. Benech, and M. Fink. Coherent plane-wave compounding for very high frame rate ultrasonography and transient elastography. *Ultrasonics, Ferroelectrics and Frequency Control, IEEE Transactions on*, 56(3):489–506, 2009.
- [114] Leonardo G Montilla, Ragnar Olafsson, Daniel R Bauer, and Russell S Witte. Real-time photoacoustic and ultrasound imaging: a simple solution for clinical ultrasound systems with linear arrays. *Physics in medicine and biology*, 58(1):N1, 2013.
- [115] Michael Moseley and Geoffrey Donnan. Multimodality imaging introduction. *Stroke*, 35(11 suppl 1):2632–2634, 2004.
- [116] Morteza Naghavi, Peter Libby, Erling Falk, S Ward Casscells, Silvio Litovsky, John Rumberger, Juan Jose Badimon, Christodoulos Stefanadis, Pedro Moreno, Gerard Pasterkamp, et al. From vulnerable plaque to vulnerable patient a call for new definitions and risk assessment strategies: part i. *Circulation*, 108(14):1664–1672, 2003.
- [117] N. Nighthoghsian, L. Drexler, and P. Douek. The vulnerable carotid artery plaque: current imaging methods and new perspectives. *Stroke*, 36(12):2764, 2005.
- [118] J Alison Noble and Djamel Boukerroui. Ultrasound image segmentation: a survey. *Medical Imaging, IEEE Transactions on*, 25(8):987–1010, 2006.
- [119] YZ O'Connor and J.A. Fessler. Fourier-based forward and back-projectors in iterative fan-beam tomographic image reconstruction. *Medical Imaging, IEEE Transactions on*, 25(5):582–589, 2006.
- [120] A.A. Oraevsky, S.L. Jacques, and F.K. Tittel. Measurement of tissue optical properties by time-resolved detection of laser-induced transient stress. *Applied Optics*, 36(1):402–415, 1997.
- [121] M.F. O'Rourke, J.A. Staessen, C. Vlachopoulos, D. Duprez, and Gérard E Plante. Clinical applications of arterial stiffness: definitions and reference values. *American Journal of Hypertension*, 15(5):426–444, 2002.
- [122] Tanmayi Oruganti, Jan G Laufer, and Bradley E Treeby. Vessel filtering of photoacoustic images. In *SPIE BiOS*, page 85811. International Society for Optics and Photonics, 2013.
- [123] G Paltauf, R Nuster, M Haltmeier, and P Burgholzer. Experimental evaluation of reconstruction algorithms for limited view photoacoustic tomography with line detectors. *Inverse Problems*, 23(6):S81–S94, 2007.
- [124] S. Pan and A. Kak. A computational study of reconstruction algorithms for diffraction tomography: interpolation versus filtered-backpropagation. *Acoustics, Speech and Signal Processing, IEEE Transactions on*, 31(5):1262–1275, 1983.
- [125] Kosmas I Paraskevas, Dimitri P Mikhailidis, and Frank J Veith. Comparison of the five 2011 guidelines for the treatment of carotid stenosis. *Journal of vascular surgery*, 55(5):1504–1508, 2012.
- [126] Thomas A Pearson, Steven N Blair, Stephen R Daniels, Robert H Eckel, Joan M Fair, Stephen P Fortmann, Barry A Franklin, Larry B Goldstein, Philip Greenland, Scott M Grundy, et al. Aha guidelines for primary prevention of cardiovascular disease and stroke: 2002 update consensus panel guide to comprehensive risk reduction for adult patients without coronary or other atherosclerotic vascular diseases. *Circulation*, 106(3):388–391, 2002.

- [127] Pieter. Contrast enhancement in photoacoustic imaging. Master's thesis, Delft University of Technology, 2010.
- [128] D. Potts, G. Steidl, and M. Tasche. *Fast Fourier transforms for nonequispaced data: A tutorial*. Citeseer, 2001.
- [129] Koen D Reesink, Evelien Hermeling, M Christianne Hoeberigs, Robert S Reneman, and Arnold PG Hoeks. Carotid artery pulse wave time characteristics to quantify ventriculoarterial responses to orthostatic challenge. *Journal of Applied Physiology*, 102(6):2128–2134, 2007.
- [130] Robert S Reneman, Jan M Meinders, and Arnold PG Hoeks. Non-invasive ultrasound in arterial wall dynamics in humans: what have we learned and what remains to be solved. *European Heart Journal*, 26(10):960–966, 2005.
- [131] Javier Sanz and Zahi A Fayad. Imaging of atherosclerotic cardiovascular disease. *Nature*, 451(7181):953–957, 2008.
- [132] G.E. Sarty, R. Bennett, and R.W. Cox. Direct reconstruction of non-cartesian k-space data using a nonuniform fast Fourier transform. *Magnetic Resonance in Medicine*, 45(5):908–915, 2001.
- [133] Abraham Savitzky and Marcel JE Golay. Smoothing and differentiation of data by simplified least squares procedures. *Analytical chemistry*, 36(8):1627–1639, 1964.
- [134] J.A. Schaar, C.L. de Korte, F. Mastik, C. Strijder, G. Pasterkamp, E. Boersma, P.W. Serruys, and A.F.W. van der Steen. Characterizing vulnerable plaque features with intravascular elastography. *Circulation*, 108(21):2636–2641, 2003.
- [135] J.A. Schaar, J.E. Muller, E. Falk, R. Virmani, V. Fuster, P.W. Serruys, A. Colombo, C. Stefanadis, C.S. Ward, P.R. Moreno, et al. Terminology for high-risk and vulnerable coronary artery plaques. report of a meeting on the vulnerable plaque, june 17 and 18, 2003, santorini, greece. *European Heart Journal*, 25(12):1077, 2004.
- [136] Arno Schmidt-Trucksäss, Dominik Grathwohl, Andreas Schmid, Raffael Boragk, Christine Upmeyer, Joseph Keul, and Martin Huonker. Assessment of carotid wall motion and stiffness with tissue doppler imaging. *Ultrasound in Medicine & Biology*, 24(5):639–646, 1998.
- [137] R. Schulze, G. Zangerl, M. Holotta, D. Meyer, F. Handle, R. Nuster, G. Paltauf, and O. Scherzer. On the use of frequency-domain reconstruction algorithms for photoacoustic imaging. *Journal of Biomedical Optics*, 16(8):086002, 2011.
- [138] Patrick Segers, Jan Kips, Bram Trachet, Abigail Swillens, Sebastian Vermeersch, Dries Mahieu, Ernst Rietzschel, Marc De Buyzere, and Luc Van Bortel. Limitations and pitfalls of non-invasive measurement of arterial pressure wave reflections and pulse wave velocity. *Artery Research*, 3(2):79–88, 2009.
- [139] S. Sethuraman, J.H. Amirian, S.H. Litovsky, R.W. Smalling, and S.Y. Emelianov. Spectroscopic intravascular photoacoustic imaging to differentiate atherosclerotic plaques. *Optics Express*, 16(5):3362–3367, 2008.
- [140] Robert E Shadwick. Mechanical design in arteries. *Journal of Experimental Biology*, 202(23):3305–3313, 1999.
- [141] Prediman K Shah. Mechanisms of plaque vulnerability and rupture. *Journal of the American College of Cardiology*, 41(4s1):S15–S22, 2003.
- [142] Prediman K Shah. Screening asymptomatic subjects for subclinical atherosclerosis: can we, does it matter, and should we? *Journal of the American College of Cardiology*, 56(2):98–105, 2010.
- [143] D. Shahmirzadi and E.E. Konofagou. Detection of aortic wall inclusions using regional pulse wave propagation and velocity *in silico*. *Artery Research*, 2012.
- [144] David P Shattuck, Marc D Weinschenker, Stephen W Smith, and Olaf T von Ramm. Explososcan: A parallel processing technique for high speed ultrasound imaging with linear phased arrays. *The Journal of the Acoustical Society of America*, 75(4):1273–1282, 1984.
- [145] Boris V Shekhonin, Sergey P Domogatsky, Vladimir R Muzykantov, Grigory L Idelson, and Vadim S Rukosuev. Distribution of type i, iii, iv and v collagen in normal and atherosclerotic human arterial wall: immunomorphological characteristics. *Collagen and related research*, 5(4):355–368, 1985.
- [146] Tetsuo Shoji, Kiyoshi Maekawa, Masanori Emoto, Senji Okuno, Tomoyuki Yamakawa, Eiji Ishimura, Masaaki Inaba, and Yoshiki Nishizawa. Arterial stiffness predicts cardiovascular death independent of arterial thickness in a cohort of hemodialysis patients. *Atherosclerosis*, 210(1):145–149, 2010.
- [147] CJ Slager, JJ Wentzel, FJH Gijssen, JCH Schuurbiers, AC van Der Wal, AFW Van der Steen, and PW Serruys. The role of shear stress in the generation of rupture-prone vulnerable plaques. *Nature clinical practice cardiovascular medicine*, 2(8):401–407, 2005.
- [148] G.L. Sorensen, J.B. Jensen, J. Udesen, I.K. Holfort, and J.A. Jensen. Pulse wave velocity in the carotid artery. In *Ultrasonics Symposium, 2008. IUS 2008*. IEEE, pages 1386–1389. IEEE, 2008.
- [149] Christin Stegemann, Ignat Drozdov, Joseph Shalhoub, Julia Humphries, Christophe Ladroue, Athanasios Dindangelos, Mark Baumert, Mark Allen, Alun H Davies, Claudia Monaco, et al. Comparative lipidomics profiling of human atherosclerotic plaques. *Circulation: Cardiovascular Genetics*, 4(3):232–242, 2011.
- [150] G. Steidl. A note on fast Fourier transforms for nonequispaced grids. *Advances in computational mathematics*, 9(3):337–352, 1998.
- [151] Richard Su, Sergey A Ermilov, Anton V Liopo, and Alexander A Oraevsky. Three-dimensional optoacoustic imaging as a new noninvasive technique to study long-term biodistribution of optical contrast agents in small animal models. *Journal of Biomedical Optics*, 17(10):1015061–1015067, 2012.

- [152] B.P. Sutton, D.C. Noll, and J.A. Fessler. Fast, iterative image reconstruction for mri in the presence of field inhomogeneities. *Medical Imaging, IEEE Transactions on*, 22(2):178–188, 2003.
- [153] Mickaël Tanter, Jeremy Bercoff, Laurent Sandrin, and Mathias Fink. Ultrafast compound imaging for 2-d motion vector estimation: application to transient elastography. *Ultrasonics, Ferroelectrics and Frequency Control, IEEE Transactions on*, 49(10):1363–1374, 2002.
- [154] Mickael Tanter and Mathias Fink. Ultrafast imaging in biomedical ultrasound. *Ultrasonics, Ferroelectrics and Frequency Control, IEEE Transactions on*, 61(1):102–119, 2014.
- [155] Charles A Taylor and JD Humphrey. Open problems in computational vascular biomechanics: hemodynamics and arterial wall mechanics. *Computer methods in applied mechanics and engineering*, 198(45):3514–3523, 2009.
- [156] Carolus JPM Teirlinck, Robert A Bezemer, Christian Kollmann, Jaap Lubbers, Peter R Hoskins, Peter Fish, Knud-Erik Fredfeldt, and Ulrich G Schaarschmidt. Development of an example flow test object and comparison of five of these test objects, constructed in various laboratories. *Ultrasonics*, 36(1):653–660, 1998.
- [157] Piero Tortoli, Tiziano Morganti, Giacomo Bambi, Carlo Palombo, and Kumar V Ramnarine. Noninvasive simultaneous assessment of wall shear rate and wall distension in carotid arteries. *Ultrasound in Medicine & Biology*, 32(11):1661–1670, 2006.
- [158] B.E. Treeby and BT Cox. k-wave: Matlab toolbox for the simulation and reconstruction of photoacoustic wave fields. *Journal of Biomedical Optics*, 15(2):021314, 2010.
- [159] F. Triposkiadis, G. Sifafidis, J. Kostoulas, J. Skoularigis, E. Zintzaras, and I. Fezoulidis. Carotid plaque composition in stable and unstable coronary artery disease. *The American Heart Journal*, 150(4):782–789, 2005.
- [160] Ivan KH Tsang, Billy YS Yiu, and Alfred CH Yu. A least-squares vector flow estimator for synthetic aperture imaging. In *Ultrasonics Symposium (IUS), 2009 IEEE International*, pages 1387–1390. IEEE, 2009.
- [161] Jesper Udesen, Fredrik Gran, K Hansen, Jørgen Arendt Jensen, Carsten Thomsen, and Michael Bachmann Nielsen. High frame-rate blood vector velocity imaging using plane waves: simulations and preliminary experiments. *Ultrasonics, Ferroelectrics and Frequency Control, IEEE Transactions on*, 55(8):1729–1743, 2008.
- [162] N.M. van Popele, D.E. Grobbee, M.L. Bots, R. Asmar, J. Topouchian, R.S. Reneman, A.P.G. Hoeks, D.A.M. van der Kuip, A. Hofman, and J.C.M. Witteman. Association between arterial stiffness and atherosclerosis: the rotterdam study. *Stroke*, 32(2):454–460, 2001.
- [163] A.A.Karabutov V.E. Gusev. *Laser Optoacoustics*. American Institute of Physics, 1993.
- [164] Renu Virmani, Frank D Kolodgie, Allen P Burke, Andrew Farb, and Stephen M Schwartz. Lessons from sudden coronary death a comprehensive morphological classification scheme for atherosclerotic lesions. *Arteriosclerosis, thrombosis, and vascular biology*, 20(5):1262–1275, 2000.
- [165] William F Walker and Gregg E Trahey. A fundamental limit on the performance of correlation based phase correction and flow estimation techniques. *Ultrasonics, Ferroelectrics and Frequency Control, IEEE Transactions on*, 41(5):644–654, 1994.
- [166] William F Walker and Gregg E Trahey. A fundamental limit on delay estimation using partially correlated speckle signals. *Ultrasonics, Ferroelectrics and Frequency Control, IEEE Transactions on*, 42(2):301–308, 1995.
- [167] Bo Wang, Jimmy L Su, James Amirian, Silvio H Litovsky, Richard Smalling, and Stanislav Emelianov. Detection of lipid in atherosclerotic vessels using ultrasound-guided spectroscopic intravascular photoacoustic imaging. *Optics Express*, 18(5):4889–4897, 2010.
- [168] Bo Wang, Evgeniya Yantsen, Timothy Larson, Andrei B Karpouk, Shiram Sethuraman, Jimmy L Su, Konstantin Sokolov, and Stanislav Y Emelianov. Plasmonic intravascular photoacoustic imaging for detection of macrophages in atherosclerotic plaques. *Nano Letters*, 9(6):2212–2217, 2008.
- [169] Shun-Li Wang, Meng-Lin Li, and Pai-Chi Li. Estimating the blood velocity vector using aperture domain data. *Ultrasonics, Ferroelectrics and Frequency Control, IEEE Transactions on*, 54(1):70–78, 2007.
- [170] Shun-Li Wang and Pai-Chi Li. Mvdr-based coherence weighting for high-frame-rate adaptive imaging. *Ultrasonics, Ferroelectrics and Frequency Control, IEEE Transactions on*, 56(10):2097–2110, 2009.
- [171] LS Wilson and DE Robinson. Ultrasonic measurement of small displacements and deformations of tissue. *Ultrasonic imaging*, 4(1):71–82, 1982.
- [172] Peter WF Wilson, Ralph B, D’Agostino, Daniel Levy, Albert M Belanger, Halit Silbershatz, and William B Kannel. Prediction of coronary heart disease using risk factor categories. *Circulation*, 97(18):1837–1847, 1998.
- [173] M. Xu and L.V. Wang. Photoacoustic imaging in biomedicine. *Review of Scientific Instruments*, 77:041101, 2006.
- [174] Y. Xu, D. Feng, and L.V. Wang. Exact frequency-domain reconstruction for thermoacoustic tomography. i. planar geometry. *Medical Imaging, IEEE Transactions on*, 21(7):823–828, 2002.
- [175] Yuan Xu, Lihong V Wang, Gaik Ambartsoumian, and Peter Kuchment. Reconstructions in limited-view thermoacoustic tomography. *Medical Physics*, 31:724, 2004.
- [176] Guillaume Zahnd, Maciej Orkisz, André Sérusclat, Philippe Moulin, and Didier Vray. Evaluation of a kalman-based block matching method to assess the bi-dimensional motion of the carotid artery wall in b-mode ultrasound sequences. *Medical Image Analysis*, 17(5):573–585, 2013.
- [177] D. Zhang, J. Tao, and H. Zheng. A novel gridding algorithm using NUFFT with applications to ultrasound

diffraction tomography. *Bioinformatics and Biomedical Engineering, ICBBE 2008*, pages 2473–2476, 2008.

- [178] H. Zhang, S. Fan, Q. Zhou, D. Lu, and D. Ta. Diffraction ultrasonic lamb wave tomography using nonuniform FFT. *Ultrasonics, Ferroelectrics and Frequency Control, IEEE Transactions on*, pages 918–921, 2006.
- [179] K. Zhang and J.U. Kang. Graphics processing unit accelerated non-uniform fast Fourier transform for ultrahigh-speed, real-time Fourier-domain oct. *Optics Express*, 18(22):23472–23487, 2010.

Summary

The carotid arteries supply the brain with oxygenated blood. These arteries can be affected by a disease called atherosclerosis. During the progression of this disease, plaques grow inside the artery wall. When these plaques rupture and the plaque content is exposed to the blood stream, cerebral events such as stroke may follow. This thesis is about the development of new imaging techniques that can be used to visualize the carotid arteries and possible plaques within.

The work of this thesis is divided into two parts. Part I deals with high-frame-rate ultrasound imaging as a means for revealing the mechanical properties of arterial plaques. In this technique we transmit one ultrasound wave and receive a set of echoes which tell us two things: the time period between transmitting the wave and receiving the echoes tells us where the tissue is located; and the strength of the echo gives us information about the density of the tissue. In this way, the technique allows us to visualize in unprecedented detail the motion of the arteries as they respond to pressure changes throughout the cardiac cycle.

High-frame-rate ultrasound is discussed in more detail in chapter two, where we present a new image reconstruction method for this technique. For this reconstruction method we adapted an algorithm known as non-uniform fast Fourier transform. This algorithm allows us to improve the overall reconstruction, not only in terms of speed - a necessary condition considering the large amount of data - but also in terms of quality. In chapter three we present the application of this imaging technique to visualize carotid arterial wall motion in healthy volunteers and two patients. Our measurements of arterial pulse waves along the arterial wall demonstrated that wave propagation is different around plaques.

While the direction of arterial motion that we measured in chapter three was mainly towards-and-away from the ultrasonic transducer, when the carotid artery is imaged in transverse view we also need to measure motion in the left-and-right direction. In chapter four we therefore present a new motion estimation technique with which we can measure motion in all directions. For this method we looked at small signal delays that can be measured across the electric elements contained in an ultrasonic transducer before we apply image reconstruction. This approach allows us to measure ultra-small displacements (less than a millionth of a meter) over a very short period of time (less than a thousandth of a second). We successfully tested this method on synthetic models of human tissue and on a carotid artery of a healthy volunteer. The ultrasound imaging technique enables us to not only show tissue motion but also to derive from it parameters about tissue integrity and stability.

Part II deals with a technique called photoacoustic imaging as a means for revealing the biochemical makeup of arterial plaques. For this technique, we use a short light pulse to excite tissue that - after absorption - produces a short acoustic wave. Once more, the waves produced with this technique tell us several things: the time period between light delivery and acoustic detection tells us where the tissue is located; the frequency of

the signal provides information about the size of the absorbing tissue structure; and the amplitude of the acoustic signal provides information about the optical absorption strength, which is directly related to the tissue's biochemical makeup. In chapter five we present a method that improves the reconstruction of photoacoustic images using information that is present in ultrasound images. By simulating the expected photoacoustic signals that emerge from the sources identified in the ultrasound image, and then subtracting the simulated signals from the real signals, we can successfully reveal the weaker photoacoustic signals.

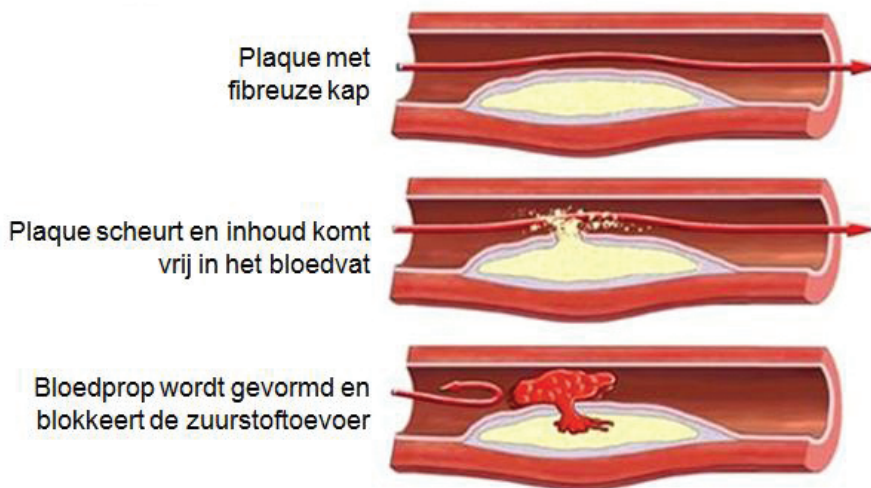
In chapter six we present a method for photoacoustic imaging of the carotid artery. Here we propose delivering the needed light to the carotid artery using a small optical probe that can be placed inside the throat. The resulting acoustic signals can then be recorded with a transducer placed at the neck. We tested this imaging method on an *ex vivo* specimen of a diseased carotid artery that was embedded in a tissue phantom mimicking the neck. Using light of different wavelengths and a newly developed tissue classification tool we were able to reveal a small plaque that was located inside the arterial wall and filled with lipids associated with atherosclerosis. These findings were later confirmed by histology. In the final chapter, we discuss the overall findings and future continuation of this research. In particular, we discuss the challenges faced with regard to photoacoustic imaging of the carotid artery *in vivo* and suggest possible solutions with regard to its implementation.

The techniques presented in this thesis are tailored towards non-invasive imaging of the carotid artery and imaging of plaques within these arteries in particular. While some of the techniques can be directly applied in small clinical studies, others - such as photoacoustic imaging of the carotid artery - require further research and technological development. We hope that these techniques may ultimately contribute to better understanding and treatment of carotid atherosclerosis.

Samenvatting

De halsslagaders voorzien de hersenen van zuurstofrijk bloed. Wanneer een halsslagader vanwege een ziekte, zoals aderverkalking, niet meer goed functioneert, kan dit desastreuze gevolgen voor de hersenen hebben. Dit proefschrift gaat over het verbeteren van bestaande en het ontwikkelen van nieuwe beeldtechnieken waarmee de halsslagader kan worden afgebeeld. We hopen dat deze technieken de artsen kunnen helpen in het stellen van een betere diagnose en bij de behandeling van ziektes zoals aderverkalking.

In het onderzoek waar dit proefschrift over gaat wilden we met name de vaatwand van de halsslagader zo goed mogelijk in beeld brengen. Aderverkalking zorgt namelijk voor een plaatselijke ophoping, ook wel plaque genoemd, van allerlei slechte stoffen en moleculen in de vaatwand van de aderen. Wanneer een dergelijke plaque openbreekt en de inhoud in de bloedbaan terecht komt, kan als gevolg hiervan onmiddellijk een herseninfarct ontstaan. De kans dat een plaque openbreekt heeft te maken met hoe sterk deze plaque is en welke stoffen zich binnen de plaque hebben opgehoopt. Daarom willen we juist deze twee aspecten, sterkte en samenstelling van de plaque, afbeelden.



Figuur 7.3: Door aderverkalking ontstaan er plaques aan de binnenkant van de vaatwand. Wanneer deze breken kan het nieuw gevormde bloedstolsel de bloedvoorziening naar andere organen zoals de hersenen stoppen. Dit heet een infarct. bron: <http://www.cholesterolvoorlichting.nl/>

Het eerste deel van dit proefschrift gaat over het afbeelden van de halsslagader door middel van echografie. Door het uitzenden van een korte ultrasonie (een frequentie boven de gehoorrens) puls en het vervolgens ontvangen van de echo's kunnen we een afbeelding van de omgeving maken. Hoe lang de echo's er over doen om heen en weer te gaan vertelt

ons hoe diep het reflecterende materiaal zit. De sterkte van de echo's vertelt ons hoe dicht (stevig) het reflecterende materiaal is. Bij iemand met een dikke nek zullen de echo's er dus langer over doen voordat ze de achterkant van de halsslagader hebben bereikt dan bij iemand met een smalle nek. Zo zullen ook de echo's van een stukje verkalkt weefsel veel sterker zijn dan de echo's die terugkomen van een zacht stukje weefsel.

Om een mooi echografisch plaatje te maken heb je heel wat van deze puls-en-echo metingen nodig. Helaas is dit proces vaak te langzaam om ook nog naar kortdurende bewegingen van het weefsel te kijken. Als het volgende plaatje aan de beurt komt, is soms de beweging al weer voorbij. In de laatste jaren is er daarom een techniek ontwikkeld waarbij er maar één puls-en-echo meting nodig is voor één plaatje. Deze techniek heet in het Engels high-frame-rate imaging. De plaatjes die deze techniek met zich mee brengt zijn minder mooi dan de gewone plaatjes, maar ze kunnen wel heel snel achter elkaar gemaakt worden, waardoor er geen beweging meer gemist hoeft te worden. Nou is er aangetoond dat wanneer je kan laten zien hoe weefsel ten opzichte van elkaar beweegt je een inschatting kan maken over de stevigheid en sterkte van het weefsel. Dit maakt deze techniek relevant voor ons onderzoek naar aderverkalking. Daarom hebben wij deze techniek verder ontwikkeld en toegepast op het afbeelden van de halsslagader.

In het eerste deel van dit proefschrift kijken we dus naar hoe high-frame-rate imaging gebruikt kan worden om bewegingen in de wand van de halsslagader vast te leggen. In het tweede hoofdstuk wordt beschreven hoe we op een snelle en precieze manier uit al die echo's, plaatjes kunnen reconstrueren. De reconstructie snelheid is van belang omdat de high-frame-rate techniek in een korte tijd heel veel echo's opneemt en we de resultaten snel willen kunnen zien. In hoofdstuk drie hebben we deze reconstructie techniek toegepast voor het meten van bewegingen in de halsslagader van een groep gezonde mensen en twee patiënten met aderverkalking. Hier tonen we, dat we heel precies kunnen afbeelden hoe een drukgolf over de vaatwand van beneden naar boven loopt. We zagen dat deze drukgolf anders verloopt bij mensen met plaques in de halsslagaders.

De tegemoetkomende-en-afgaande bewegingsrichting die we in hoofdstuk drie hebben gemeten kunnen relatief makkelijk gemeten worden. Veel moeilijker is het om een links-en-rechts bewegingsrichting te meten. Dit probleem hebben we opgelost in hoofdstuk vier. Door slim gebruik te maken van de informatie die in de echo's verscholen zit voordat we een plaatje reconstrueren kunnen we deze links-en-rechts bewegingen al meten. De nieuwe methode hebben we uitvoerig onderzocht met behulp van experimenten waarin we verschillende materialen, verschillende kanten op lieten bewegen. In al de gevallen konden we de verplaatsingen nauwkeurig genoeg meten. Ook hebben we deze methode uiteindelijk uitgeprobeerd op plaatjes van de halsslagader van een gezonde vrijwilliger. Hierbij bleek dat we nu voor het eerst alle bewegingsrichtingen met de gewenste nauwkeurigheid kunnen meten. We hopen dat we nu ook beter in kaart kunnen brengen hoe plaques bewegen en van daaruit kunnen beoordelen hoe sterk of hoe stabiel de plaques zijn.

In het tweede deel van dit proefschrift kijken we naar een nieuwe techniek die nog niet echt in de kliniek wordt toegepast. Deze techniek heet fotoakoestiek. In plaats van het sturen van een korte ultrasonische puls waarvan we de echo's daarna weer opvangen, gebruiken we nu een heel kort durende lichtpuls. Wanneer deze lichtpuls in aanraking komt met

absorberend weefsel zal het weefsel heel even opwarmen. Omdat dit weefsel iets warmer wordt dan het omliggende weefsel ontstaat er een klein drukgolfje dat veel lijkt op het ultrasonische golfje dat we voor echografie gebruiken. Dit drukgolfje kunnen we dan ook met dezelfde detectors opnemen die we ook in de echografie techniek gebruiken. Hoe lang dit golfje er over doet om bij onze detector uit te komen vertelt ons, net zoals bij echografie, hoe diep dit absorberend weefsel zit. De sterkte van het drukgolfje vertelt ons hoeveel van het licht geabsorbeerd is. Anders dan met echografie, waarin we vooral verschil zien tussen weefsels op basis van de dichtheid, zien we nu verschil tussen weefsels op basis van de absorberende eigenschappen. En deze eigenschappen zijn verschillend per weefsel type. Deze beeld techniek willen we daarom gebruiken om te kijken of we de samenstelling van plaques kunnen afbeelden.

In hoofdstuk vijf van dit proefschrift hebben we eerst gekeken naar hoe we deze twee technieken (echografie en fotoakoestiek) kunnen combineren. Het meest voor de hand liggend zou zijn om gewoon twee verschillende plaatjes te maken en die dan allebei aan de dokter te laten zien. Maar omdat beide beeldtechnieken worden gebruikt om dezelfde halsslagader af te beelden zouden we ook kunnen kijken of we het ene plaatje kunnen gebruiken om het andere beter te maken. Met dit idee hebben we een methode ontwikkeld waarin we het echo plaatje gebruiken om een voorspelling te doen over wat we met fotoakoestiek zullen zien. Deze voorspelling doen we door middel van snelle computer simulaties. Door nu deze voorspelde drukgolfjes van de echte gemeten drukgolfjes af te trekken kunnen we ineens de hele kleine, diepverscholen drukgolfjes zien. Door deze verscholen drukgolfjes af te beelden kunnen we nu laten zien wat er in de vaatwand zit in plaats van het laten zien van voornamelijk drukgolfjes die van de vaatwand zelf komen.

Omdat de licht absorberende eigenschappen uniek zijn voor elk weefseltype, kunnen we kijken of we deze verschillende typen ook uit elkaar kunnen halen. Hiervoor gebruiken we verschillende kleuren licht. Omdat weefsel type A een sterk golfje afgeeft bij een rode kleur maar niet bij een blauwe kleur licht kunnen we met behulp van deze twee kleuren weefsel A detecteren. Voor de plaques in zieke halsslagaders zijn we vooral geïnteresseerd in de ophoping van vet. Dit vet zorgt er onder andere voor dat de plaque gemakkelijk kan openbreken. We weten ook dat dit soort vet bij een specifieke infrarode kleur een sterk signaal afgeeft. Het nadeel van deze kleur licht is dat ze ook sterk wordt geabsorbeerd door ander weefsel. Als we dus deze kleur licht willen gebruiken om door de nek de halsslagader te beschijnen hebben we een probleem, zeker bij mensen die een dikke nek hebben. Om dit probleem op te lossen hebben we bedacht om de halsslagader vanuit de keelholte te beschijnen. Hier hebben we minder last van lichtabsorptie en de afstand tot de halsslagader is ook nog eens korter.

De resultaten van een eerste proef waarin we dit idee hebben getest is te vinden in hoofdstuk zes. Hier hebben we een halsslagader van een overleden persoon afgebeeld met fotoakoestiek. We hebben de optische eigenschappen van de nek nagebootst en een klein optische instrument gemaakt om de halsslagader mee te belichten. De resultaten van dit onderzoek zijn veelbelovend. We konden namelijk het begin van een vet achtige plaque in de wand van de halsslagader waarnemen. Dit was niet te zien met echografie maar wel met fotoakoestiek. Dit is de eerste keer dat dit voor de halsslagader is gelukt. Na dit experiment hebben we het bestaan van deze vet ophoping ook door middel van microscopie aangetoond.

Deze techniek is nog niet zo ver dat het direct in de kliniek kan worden toegepast. Wel laten we in het laatste hoofdstuk van dit proefschrift zien dat we met een nieuw flexibel optisch instrument al een eerste poging hebben ondernomen om bij een gezonde vrijwilliger te kijken of we fotoakoestische drukgolfjes van de halsslagader konden detecteren. Al met al hopen we dat het onderzoek dat in dit proefschrift staat beschreven kan bijdragen aan een beter begrip van de halsslagader en ziekten zoals aderverkalking. Sommige van de beschreven technieken zouden al direct in een academische klinische setting kunnen worden toegepast. Andere, zoals het gebruik van fotoakoestiek van de halsslagader heeft nog onderzoek nodig. Ook kunnen veel van de technieken en methoden die in dit onderzoek zijn ontwikkeld voor andere toepassingen worden gebruikt.

Publications

Journal Papers

- **Pieter Kruizinga**, Frits Mastik, Nico de Jong, Antonius F.W. van der Steen, and Gijs van Soest, Plane-wave ultrasound beamforming using a nonuniform fast Fourier transform, *Ultrasonics, Ferroelectrics and Frequency Control, IEEE Transactions on* 59, no. 12 (2012).
- **Pieter Kruizinga**, Frits Mastik, Dion Koeze, Nico de Jong, Anton F.W. van der Steen, and Gijs van Soest. Ultrasound-guided photoacoustic image reconstruction: image completion and boundary suppression, *Journal of Biomedical Optics* 18, no. 9 (2013).
- **Pieter Kruizinga**, Frits Mastik, Stijn C.H. van den Oord, Arend F.L. Schinkel, Johannes G. Bosch, Nico de Jong, Gijs van Soest and Anton F.W. van der Steen, High-definition imaging of carotid artery wall dynamics, *Ultrasound in Biology & Medicine* 40, no. 10 (2014).
- **Pieter Kruizinga**, Antonius F.W. van der Steen, Nico de Jong, Geert Springeling, Jan Lukas Robertus, Aad van der Lugt and Gijs van Soest, Photoacoustic imaging of carotid artery atherosclerosis, *Journal of Biomedical Optics* 19 no. 11 (2014).
- **Pieter Kruizinga**, Frits Mastik, Johannes G. Bosch, Nico de Jong, Anton F.W. van der Steen and Gijs van Soest, Measuring ultra-small displacement vectors using High Frame Rate Ultrasound Imaging, *Ultrasonics, Ferroelectrics and Frequency Control, IEEE Transactions on* **in review**.
- Yun-Sheng Chen, Wolfgang Frey, Seungsoo Kim, **Pieter Kruizinga**, Kimberly Homan, and Stanislav Emelianov, Silica-coated gold nanorods as photoacoustic signal nanoamplifiers, *Nano Letters* 11, no. 2 (2011).
- Yun-Sheng Chen, Wolfgang Frey, Seungsoo Kim, Kimberly Homan, **Pieter Kruizinga**, Konstantin Sokolov, and Stanislav Emelianov, Enhanced thermal stability of silica-coated gold nanorods for photoacoustic imaging and image-guided therapy, *Optics Express* 18, no. 9 (2010).
- Mohammad Mehrmohammadi, Tae-Hyun Shin, Min Qu, **Pieter Kruizinga**, Ryan L. Truby, Jae-Hyun Lee, Jinwoo Cheon, and Stanislav Y. Emelianov, In vivo pulsed magneto-motive ultrasound imaging using high-performance magnetoactive contrast nanoagents, *Nanoscale* 5, no. 22 (2013).

Conference Proceedings, Abstracts, Posters and Talks

- Erika J.Cooley, **Pieter Kruizinga**, Darren W. Branch, and Stanislav Emelianov, Evaluation of arsenazo iii as a contrast agent for photoacoustic detection of micromolar calcium transients, *International Society for Optics and Photonics*, 2010.
- Yun-Sheng Chen, **Pieter Kruizinga**, Pratixa P. Joshi, Seungsoo Kim, Kimberly Homan, Konstantin Sokolov, Wolfgang Frey, and Stanislav Emelianov, On stability of molecular therapeutic agents for noninvasive photoacoustic and ultrasound image-guided photothermal therapy, *International Society for Optics and Photonics*, 2010.
- **Pieter Kruizinga**, Seungsoo Kim, Salavat Aglyamov, Gijs van Soest, Anton F.W. van der Steen and Stanislav Emelianov, Signal content windowing for SNR improvement in photoacoustic imaging, *SPIE/O.S.A European Conferences on Biomedical Optics (ECBO)*, 8090-19 2011.
- **Pieter Kruizinga**, Frits Mastik, Nico de Jong, Anton F.W. van der Steen, and Gijs van Soest, Ultrasound guided photoacoustic image reconstruction, *Optics in Cardiology* 2012.

- **Pieter Kruizinga** Frits Mastik, Nico de Jong, Antonius F.W. van der Steen and Gijs van Soest, Assessing artery wall dynamics with high frame rate ultrasound imaging and three dimensional phase analysis, 11th *International Conference on the Ultrasonic Measurements and Imaging of Tissue Elasticity* 2012.
- **Pieter Kruizinga**, Frits Mastik, Nico De Jong, Anton F.W. van der Steen and Gijs van Soest, *Ultrasound-guided photoacoustic image reconstruction*, International Society for Optics and Photonics, 2012.
- **Pieter Kruizinga**, Frits Mastik, Nico de Jong, Anton F.W. van der Steen, and Gijs van Soest, High frame rate ultrasound imaging of human carotid artery dynamics, *IEEE International Ultrasonics Symposium (IUS)* 2012.
- **Pieter Kruizinga**, Ben Cox, Nico de Jong, Paul Beard, Anton F.W. van der Steen, and Gijs van Soest, Plane wave ultrasound imaging with a broadband photoacoustic source, *IEEE International Ultrasonics Symposium (IUS)* 2012.
- **Pieter Kruizinga**, Frits Mastik, Nico De Jong, Anton F.W. van der Steen and Gijs van Soest, Photoacoustic imaging of the human carotid artery: simulations, phantom studies and practical considerations, *International Society for Optics and Photonics*, 2013.
- **Pieter Kruizinga**, Frits Mastik, Geert Springeling, Nico de Jong, Anton F.W. van der Steen, and Gijs van Soest, Parameter study for photoacoustic imaging of the human carotid artery, *Optics in Cardiology* 2013.
- **Pieter Kruizinga**, Judy Zouaoui, Geert Springeling, Jan Lukas Robertus, Aad van der Lugt, Anton F.W. van der Steen and Gijs van Soest, Photoacoustic imaging of the carotid artery plaque, *International Society for Optics and Photonics*, 2014.
- **Pieter Kruizinga**, Photoacoustics and High Frame Rate imaging of the carotid, 12th *Vulnerable Patient Meeting* 2014.
- **Pieter Kruizinga**, Frits Mastik, Johannes G. Bosch, Nico de Jong, Gijs van Soest and Anton F.W. van der Steen, High Frame Rate Ultrasound Displacement Vector Imaging, *IEEE International Ultrasonics Symposium (IUS)* 2014.
- **Pieter Kruizinga**, Geert Springeling, Jan Lukas Robertus, Aad van der Lugt, Nico de Jong, Antonius F.W. van der Steen and Gijs van Soest, Photoacoustic imaging of the carotid artery, *IEEE International Ultrasonics Symposium (IUS)* 2014.
- **Pieter Kruizinga** Frits Mastik, Nico de Jong, Johannes G. Bosch, Gijs van Soest and Antonius F.W. van der Steen, Accurate measurements of tissue displacement in two dimensions using high frame rate ultrasound imaging, 13th *International Conference on the Ultrasonic Measurements and Imaging of Tissue Elasticity* 2014.

Dankwoord - Acknowledgements

Deze laatste bladzijden verwoorden mijn liefde en dankbaarheid voor een groep mensen zonder wie dit proefschrift niet was geschreven. Dat zegt niets over het onderzoek, want dat had best door iemand anders kunnen worden uitgevoerd. Alleen had ik het niet zonder onderstaande mensen kunnen doen.

Ton, het zou onzinnig zijn om dit dankwoord niet met jou te beginnen. Dankzij jou heb ik zo enorm veel kansen gekregen. Vanaf het moment dat ik als groentje op jouw lab kwam stage lopen tot nu, zo veel jaar later met mijn proefschrift op jouw overvolle tafel, heb jij gezorgd dat er niets ontbrak, grote dank daarvoor. Ik waardeer de open en gelijkwaardige manier waarop jij met jouw mensen omgaat. Ik ben blij dat ik daar één van ben.

Gijs, met aan zekerheid grenzende waarschijnlijkheid kan ik zeggen dat er weinig woorden uit dit proefschrift niet door jou gelezen zijn. Als dat iets laat zien, is het wel jouw betrokkenheid bij mijn werk en je energie en bereidwilligheid om aldoor weer door mijn bagger heen te werken. Ik heb zo ontzettend veel van jou geleerd. Ik bewonder jouw analytisch vermogen, jouw drang om dingen te begrijpen, en je onovertroffen brede kennis van dingen. Gijs, het delen van dezelfde kamer en de gezamenlijke werkreizen waren aspecten van mijn werk waar ik enorm van heb genoten. Ik ben blij dat ik jouw student mocht zijn. Wat mij blijer maakt is dat ik er een collega en vriend bij heb gekregen!

Frits, het zal de buitenwacht niet zijn ontgaan dat jij op bijna alle artikelen als tweede auteur vermeld staat. Het was, en is, een plezier om met jou samen te werken. We hebben mooie dingen gedaan en nieuwe inzichten verkregen. Heerlijk is het om samen met jou en een leeg Matlab scherm of leeg whiteboard een nieuwe gedachte van de grond af op te bouwen. Om daarbij te doen alsof de tekstboek theorie irrelevant is, vergroot alleen nog maar de feestvreugde. Je bent een creatieve denker en ik ben blij dat wij een state hebben gevonden die werkt, en die naar ik weet gaat zorgen voor leuke en nieuwe ontdekkingen.

Nico, bij het schrijven van deze zin zit ik achterin de zaal tijdens het 20^{ste} contrast symposium door jou georganiseerd. Het is inspirerend om te zien hoe na al die jaren jij nog steeds ongehinderd geïnteresseerd bent alsof het je eerste jaar van je eigen promotie is. Dat jij nog steeds Matlab op je computer hebt en weet hoe je een akoestische opstelling opbouwt is even zo inspirerend. Hans, jouw enthousiasme voor de wetenschap en het tackelen van nieuwe problemen waardeer ik enorm. Het is fijn om met jou samen te werken. Ik vertrouw erop dat we die samenwerking in toekomstig werk kunnen cashen. Mieke, Gracia en Rita, het is geen geheim dat zonder jullie geen van de 40 + technuten ook maar één formulier op tijd kan inleveren. Dank voor alles. Robert, te weten dat jij ook mee doet op het lab en zonder mopperen na zessen doorwerkt, is één van de redenen dat ik elke keer weer gerust experimenten kon gaan doen. Geert, dank dat jij een folder op jouw computer hebt staan getiteld "Pieter - vrijdagmiddag". Zonder jouw technische bijdrage en de bereidheid om op vrijdagochtend te zorgen dat ik 's vrijdagmiddags een experiment kon doen was dit boekje niet geschreven.

Charles en Jan, inzicht komt met de jaren zeggen ze. Ik ben blij dat jullie dat nog steeds met ons willen delen. Varya, It great to know you. It is even better to have you as a crazy and brilliant colleague. Rik, fijn dat jij weer terug op ons lab bent. Hans, Gerard, Alex, Zeynettin, Jacopo, Deep, Tom vR, Klazina, Tom K, Ying and Ilya it feels a bit crude to group people together and saying thanks but I have to control the printing costs you know. Thanks for being good colleagues and making the 23rd floor feel like home. Stijn, Arend en Aad hartelijk

dank voor jullie klinische bijdrage in mijn werk. Deze samenwerkingen zijn wat mij betreft uniek in de wereld en ik hoop dat we die nog meer gaan benutten.

Tianshi, Muthu, Min, Jovanna and Sophinese I'm sorry that I left the coziness of the laser lab but it still feels good to drop by every now and then. Frank jongen, elke keer als ik jou zie ben ik blij dat jij mijn collega bent. Jolanda, Lambert, Kim vdH, Merih, Hans, Jelle, Harm, Kim vG en al die lieve mensen die met zo veel passie het biomechanische proberen te modeleren mijn hartelijke dank voor de gezelligheid op de 23^{ste}. Krista, het was heerlijk om jouw collega te zijn. Jouw levenslust werkt aanstekelijk, nog steeds. The old crew, David, Telli and Guillaume I still think that all of you should come back and pretend you never left. It feels like a privilege that we are still in contact.

Stas, many thanks for the opportunity you gave me to study in your awesome lab. It feels special that you are part of the committee to judge this minor work, hope you like it. Mohammad, see you in Isfahan. Chris, ik ben blij dat ik jou heb ontmoet. Naast de conferenties maakt het de promotiecommissies nog een stukje leuker. Op de weg van leerling naar wetenschapper staan leraren aan de kant die soms de route aangeven. In mijn geval waren dat a.o. Herman Stoppels, Ton van Leeuwen, Wiebe Kruijer, Piet Dijkstra, Cees Otto, Srirang Manohar en Henk Geertsema. Dank hiervoor.

Aan al mijn vrienden die ervoor zorgen dat er een relevantere wereld bestaat naast de wetenschappelijke, dank. Marjolein, Corianne en Evelien. Het is gelukt! We zijn weer op hetzelfde niveau. Jammer dat onze meidenavondjes steeds spaarzamer worden, toch heb ik nog goede hoop dat er nieuwe gaan komen, waar ook ter wereld. Paul, door onze gesprekken leer ik, ondanks de onontkoombare herhaling, jou steeds beter kennen. Dank je voor je onvoorwaardelijke vriendschap. Gerjan, wat zijn we al lang bevriend en wat fijn dat jij als paranimf naast mij wilt staan op deze dag. Grappig hoe ons leven verloopt, heel verschillend en toch hetzelfde. Joost, wat bewonder ik jouw passie waarmee jij het leven ongeduldig tot je neemt. Het is onmogelijk om je bij te houden. Gelukkig blijkt bij elk spaarzaam biertje dat wij samen drinken dat er wezenlijk niks veranderd is.

Lieve pap en mam. Dank voor jullie opvoeding en de waarden die jullie daarin hebben overgedragen. Dank ook voor de kansen die jullie mij hebben gegeven. Dat dit boekje er nu ligt is een direct resultaat van alle lego waar ik mee mocht spelen en alle apparaten die ik mocht open maken, ook als ze het nog prima deden. Lieve zusjes Alide, Renske en Rieke, wat heb ik jullie ontzettend lief! Lieve zwagers Pierre, Niek, Reinier, Bertus en Jelto en schoonzussen Dorien en Hanneke, ook door jullie voelt het leven geworteld, en dat is soms best een fijn gevoel. Lieve Gerrit, jouw terechte verontwaardiging over dat ik 3D plaatjes ga maken en nog steeds geen 4D, snap ik helemaal. Ik heb er nog eens over nagedacht en nu denk ik dat ik toch 4D ga doen. Tijd is ook een dimensie, maar dat leg ik je later nog wel eens uit. Lieve schoonouders, dank voor jullie warme gastvrijheid en jullie lieve dochter.

Lieve Grethe, prachtige vrouw, jij bent de liefde en het geluk van mijn leven. Dank voor de ruimte die jij mij gaf voor mijn onderzoek. Jouw levenslust, jouw intelligentie, jouw humor, jouw gezelligheid en jouw manier van in de wereld staan, maken dat elke nieuwe dag met jou voelt als een fantastische toegift op al die momenten waarin wij al samen waren.

Mijn Hemelse Vader, U dank ik voor alles. Uw genade en trouw zijn elke dag nieuw.

Pieter Kruizinga
Rotterdam 2015

Curriculum vitae



Pieter Kruizinga was born in Aduard on June 14, 1983. During his childhood he lived in several places, such as in South Africa, and attended several primary schools.

After graduating from secondary school (Gomarus College in Groningen and Deltion College in Zwolle) he worked in a bakery, in order to cover the expenses of a world trip. This trip took him across Africa, Southeast Asia, Australia, China and Russia.

After his return to The Netherlands he started in 2003 with the undergraduate program of Biomedical Engineering at the University of Twente. In the second year he also started studying philosophy at the VU University in Amsterdam. He received his BSc degree Biomedical Engineering in 2006 after which he moved to Amsterdam to continue the study in philosophy. In June 2007 Pieter married Grethe van't Foort. In the same year he started with the master program Biomedical Engineering at the Delft University of Technology. He received his MSc degree from this university in 2010. For his master research he visited the Ultrasound Imaging and Therapeutics Research Laboratory at the University of Texas at Austin, USA, where he worked for a year on contrast enhancement in photoacoustic imaging.

In 2010 he joined the Biomedical Engineering group of the Thorax Center at the Erasmus Medical Centre in Rotterdam, The Netherlands as a PhD student under the supervision of dr. Gijs van Soest and Prof.dr.ir. A.F.W. van der Steen. During his PhD he focused on developing high-frame-rate ultrasound and photoacoustic imaging applied to the human carotid artery. As of July 2014, he continued his research at the same research group on the topic of high-frame-rate 3D imaging of the carotid artery.

PhD Portfolio

International conference attendance	Date	ECTS
2010 IEEE International Ultrasonics Symposium, San Diego, CA, USA	10/2010	1.20
17 th European Symposium on Ultrasound Contrast Imaging, Rotterdam, The Netherlands	01/2011	0.60
2011 BiOS, SPIE Photonics West, San Francisco, USA	01/2011	1.80
European Conference on Biomedical Optics 2011, Munich	05/2011	1.50
2011 Optics in Cardiology, Rotterdam, The Netherlands	12/2011	0.60
18 th European Symposium on Ultrasound Contrast Imaging, Rotterdam, The Netherlands	01/2012	0.60
2012 BiOS, SPIE Photonics West, San Francisco, USA	01/2012	1.80
Lasers In Medicine & Biology, 2012, Gordon Research Conferences, Hol-derness, USA	07/2012	1.80
11 th International Conference on the Ultrasonic Measurements and Ima-ging of Tissue Elasticity	10/2012	1.20
2012 IEEE International Ultrasonics Symposium, Dresden, Germany	10/2012	1.20
19 th European Symposium on Ultrasound Contrast Imaging, Rotterdam, The Netherlands	01/2012	0.60
2013 BiOS, SPIE Photonics West, San Francisco, USA	02/2013	1.80
2013 Optics in Cardiology, Rotterdam, The Netherlands	03/2013	1.00
20th European Symposium on Ultrasound Contrast Imaging, Rotterdam, The Netherlands	01/2014	0.60
2014 BiOS, SPIE Photonics West, San Francisco, USA	02/2014	1.80
Vulnerable Patient Meeting 2014, Windsor, United Kingdom	06/2014	0.90
2014 IEEE International Ultrasonics Symposium, Chicago, Germany	09/2014	1.20
13 th International Conference on the Ultrasonic Measurements and Ima-ging of Tissue Elasticity	9/2014	1.20
9 th International Conference on Ultrasonic Biomedical Microscanning	10/2014	1.20

Conference presentations	Date	ECTS
Oral presentation - European Conference on Biomedical Optics 2011	05/2011	1.90
Poster presentation - 2011 Optics in Cardiology symposium	12/2011	0.60
Poster presentation - 2012 BiOS, SPIE Photonics West conference	01/2012	1.00
Poster presentation - Lasers In Medicine & Biology, Gordon Research Conferences	07/2012	1.00
Oral presentation - 11 th International Conference on the Ultrasonic Measurements and Imaging of Tissue Elasticity	10/2012	1.90
Oral presentation - 2012 IEEE International Ultrasonics Symposium	10/2012	1.90
Oral presentation - 2012 IEEE International Ultrasonics Symposium	10/2012	1.90
Poster presentation - 2012 IEEE International Ultrasonics Symposium	10/2012	1.00
Oral presentation - 2013 BiOS, SPIE Photonics West conference	02/2013	1.90
Poster presentation - 2013 Optics in Cardiology symposium	03/2013	0.60
Oral presentation - 2014 BiOS, SPIE Photonics West conference	02/2013	1.90
Oral presentation - Vulnerable Patient Meeting 2014, Windsor, United Kingdom	06/2014	1.90
Oral presentation - 2014 IEEE International Ultrasonics Symposium	09/2014	1.90
Oral presentation - 13 th International Conference on the Ultrasonic Measurements and Imaging of Tissue Elasticity	09/2014	1.90
Oral presentation - 9 th International Conference on Ultrasonic Biomedical Microscanning	10/2014	1.90
Courses	Date	ECTS
Medical Ultrasound Transducers, 2010 IEEE IUS	09/2010	0.15
Ultrasonic Signal Processing for Detection, Estimation and Compression, 2010 IEEE IUS	10/2010	0.15
Tissue Optics, 2011 BiOS, SPIE Photonics West	01/2011	0.15
Photoshop and Illustrator Workshop, MolMed postgraduate school	02/2012	0.30
Hartstichting PhD-training courses, Vascular Biology 1	02/2011	2.0
In-Design Workshop, MolMed postgraduate school	05/2011	0.30
Ultrafast Ultrasound Imaging: Principles and Applications, 2012 IEEE IUS	10/2012	0.15
Research Seminars	Date	ECTS
Dutch Society for Medical Ultrasound Autumn meeting, Maastricht	10/2010	0.15
Dutch Society for Medical Ultrasound Spring meeting, Delft	4/2011	0.15
Dutch Society for Medical Ultrasound Autumn meeting, Eindhoven	11/2011	0.15
Dutch Society for Medical Ultrasound Autumn meeting, Maastricht	10/2013	0.15
Dutch Society for Medical Ultrasound Spring meeting, Twente	4/2014	0.15
COEUR Research Seminar: Imaging of Atherosclerosis	12/2010	0.40
COEUR Research Seminar: Detection of early atherosclerosis	03/2011	0.40
COEUR PhD-day 2011	04/2011	0.40
SoundLight - Photons for Health, symposium University of Twente	11/2011	0.30

Total ECTS: 51.25



ISBN: 987-94-6259-571-2